UNIVERSIDAD DE COSTA RICA

SISTEMA DE ESTUDIOS DE POSGRADO

Explorando la patogenicidad de especies no descritas filogenéticamente emparentadas con *Clostridioides difficile* y *Clostridium perfringens* e implicadas en infecciones comunitarias en humanos

Tesis sometida a la consideración de la Comisión del Programa de Posgrado en Microbiología y Química Clínica con énfasis en Bacteriología para optar al grado y título de Maestría Académica en Microbiología con énfasis en Bacteriología

Lic. Daniela Aguilar Orozco

Ciudad Universitaria Rodrigo Facio, Costa Rica

2026

DEDICATORIA

A mis papás, a mi hermana y a Taty.

AGRADECIMIENTO

A mi tutor, el Dr. César Rodríguez, por su guía y apoyo para el desarrollo del proyecto.

Al Dr. Carlos Quesada, el Dr. Luis Acuña y la Dra. Laura Monturiol por su guía, consejo y acompañamiento durante el proceso.

Al Dr. Josué Orozco por su entrenamiento, paciencia y guía con los modelos animales.

A Daniela Núñez, Robin Cárdenas y Pablo Vargas por el apoyo indispensable en el laboratorio.

A mis amigos, quienes siempre han estado ahí para acompañarme a cumplir mis sueños y sostenerme en el proceso: Rick, Colas, Raque, Pablo, Palola, la tía Noelia, Guille, Jerson.

A Álvaro, por su paciencia, por escucharme, apoyarme, por cuidar de mi y nunca dejarme sola.

A mis papás y mi hermana por su apoyo incondicional.

Esta tesis fue aceptada por la Comisión del Programa de Posgrado en Microbiología, Parasitología, Química Clínica e Inmunología de la Universidad de Costa Rica, como requisito parcial para optar al grado y título de Maestría Académica en Microbiología con énfasis en Bacteriología.

Ph.D. Pamela Altamirano Silva
Representante del Decano
Sistema de Estudios de Posgrado

Ph.D. César Rodríguez Sánchez
Director de Tesis

Ph.D. Carlos Quesada Gómez
Asesor

Ph.D. Laura Mònturiol Gross
Asesora

PhD. Elías Barquero Calvo
Representante del Director
Programa de Posgrado en Microbiología

Daniela Aguilar Orozco
Candidato Candidata

TITLE

Exploring the pathogenicity of previously undescribed species phylogenetically related to *Clostridioides difficile* and *Clostridium perfringens* associated with community-acquired human infections.

TABLE OF CONTENTS

DEDICATORIA i
AGRADECIMIENTO ii
TITLE iv
TABLE OF CONTENTS v
RESUMEN EN ESPAÑOL vii
ABSTRACT viii
LIST OF FIGURES ix
LIST OF TABLES xi
SUPPLEMENTARY MATERIAL xii
LIST OF ABBREVIATIONS xiii
INTRODUCTION 1
SIGNIFICANCE 5
HYPOTHESIS 6
GENERAL OBJECTIVE 6
SPECIFIC OBJECTIVES 6
CHAPTER 1 7
1.1 State of the Art 7
1.2 Materials and Methods 14
1.3 Results 21
1.4 Discussion 37
Chapter 2. 46
2.1 State of the Art 46
2.2 Materials and Methods 52
2.3 Results 62
2.4 Discussion 73
LIMITATIONS 77
CONCLUSIONS 78

PERSPECTIVES 79
TECHNICAL DECLARATIONS 80
USE OF ARTIFICIAL INTELLIGENCE TOOLS 80
FUNDING 80
FACILITIES 80
ETHICS APPROVAL 80
SUPPLEMENTARY MATERIAL 81
APPENDIX 90
REFERENCES 94

RESUMEN EN ESPAÑOL

Las bacterias anaerobias esporuladas de los géneros *Clostridioides* y *Clostridium* incluyen especies de alta relevancia clínica, como *Clostridioides difficile* y *Clostridium perfringens*, responsables de infecciones intestinales y sistémicas severas. En años recientes, análisis genómicos han revelado la existencia de linajes divergentes estrechamente relacionados con estas especies, aislados tanto de fuentes clínicas como ambientales, cuyo potencial patogénico no ha sido completamente caracterizado. El objetivo de esta tesis fue evaluar las propiedades de virulencia de nuevas especies de *Clostridioides* y *Clostridium* mediante un enfoque integrado que combinó análisis genómicos, ensayos *in vitro* y modelos experimentales *in vivo.*

En el primer eje del estudio, se analizaron cepas de origen clínico y ambiental de *Clostridioides* relacionadas con *C. difficile*, previamente identificadas como clados crípticos y referidas en este trabajo como "Cd-like" strains. Los resultados demostraron que estas cepas producen toxinas activas capaces de inducir efectos citopáticos en cultivos celulares, así como alteraciones epiteliales y una respuesta inflamatoria comparable a la observada con *C. difficile* en el modelo murino de asa ileal ligada. El potencial patogénico de los aislamientos ambientales resalta la relevancia de los reservorios no clínicos para este género.

El segundo eje se centró en el estudio de dos aislamientos clínicos de *Clostridium* relacionados con *C. perfringens*, previamente caracterizados a nivel genómico como especies no clasificadas. Se evaluó la actividad de la fosfolipasa C (PLC) y su capacidad de inducir daño tisular en un modelo murino de gangrena gaseosa. Los resultados demostraron que, a pesar de la divergencia en la secuencia de la PLC, estas cepas conservan actividad fosfolipasa, hemolítica y citotóxica, y son capaces de reproducir características clave de la mionecrosis clostridial. El análisis proteómico reveló variabilidad entre cepas y sugirió diferencias metabólicas y regulatorias que podrían modular la expresión de la virulencia.

En conjunto, los resultados indican que linajes divergentes de *Clostridioides* y *Clostridium* circulantes en Costa Rica poseen características patogénicas funcionales, aunque heterogéneas, que no pueden explicarse únicamente por la presencia o cantidad de toxinas. Estos hallazgos resaltan la naturaleza multifactorial de la virulencia clostridial y subrayan la importancia de integrar enfoques genómicos y experimentales para mejorar la vigilancia, el diagnóstico y la comprensión del riesgo asociado a estos microorganismos desde una perspectiva de One Health.

ABSTRACT

Spore-forming anaerobic bacteria of the genera *Clostridioides* and *Clostridium* include clinically important species such as *Clostridioides difficile* and *Clostridium perfringens*, which are responsible for severe intestinal and systemic infections. In recent years, genomic analyses have revealed the existence of divergent lineages closely related to these species, isolated from both clinical and environmental sources, whose pathogenic potential has not been fully characterized. The aim of this thesis was to evaluate the virulence properties of novel *Clostridioides* and *Clostridium* species using an integrated approach combining genomic analyses, *in vitro* assays, and experimental *in vivo* models.

In the first chapter of the study, clinical and environmental *Clostridioides* isolates related to *C. difficile*, previously identified as cryptic clades and referred to in this work as Cd-like strains, were analyzed. The results demonstrated that these strains produce active toxins capable of inducing cytopathic effects in cell cultures, as well as epithelial damage and inflammatory responses comparable to those observed with *C. difficile* in a murine ligated ileal loop model. The pathogenic potential of environmental isolates highlights the relevance of non-clinical reservoirs for this genus.

The second chapter is focused on two clinical *Clostridium* isolates related to *C. perfringens*, previously characterized by genomic methods as unclassified species. Phospholipase C (PLC) activity and the ability to induce tissue damage were evaluated using a murine gas gangrene model. Despite divergence in PLC sequence, these strains retained phospholipase, hemolytic, and cytotoxic activities and were capable of reproducing key features of clostridial myonecrosis. Proteomic analyses revealed strain-level variability and suggested metabolic and regulatory differences that may modulate virulent expression.

Overall, the results indicate that divergent *Clostridioides* and *Clostridium* lineages circulating in Costa Rica possess functionally relevant, though heterogeneous, pathogenic traits that cannot be explained solely by the presence or abundance of toxins. These findings underscore the multifactorial nature of clostridial virulence and highlight the importance of integrating genomic and experimental approaches to improve surveillance, diagnostics, and risk assessment from a One Health perspective.

LIST OF FIGURES

Figure1. Phylogenetic relationships within the *Clostridioides* genus based on average nucleotide identity (ANI)…….….13

Figure2. Experimental design for the characterization of *Clostridioides* genomospecies related to C. difficile……..……....15

Figure3. Germination kinetics of *Clostridioides* strains in response to taurocholate……..22

Figure4. Toxin production of *Clostridioides* strains assessed through CPE induction……24

Figure5. Kinetics of the CPE induced by cell free supernatants of Cd-like strains *in vitro*……...25

Figure6. Characterization of cytopathic effects induced by cell-free supernatants of Cd-like strains……...…….26

Figure7. GTPase glycosylation induced by cell-free supernatants of Cd-like strains…….27

Figure8. Effect of cell-free supernatants of Cd-like strains in the ligated murine ileal loop model…….……29

Figure9. Histopathological scoring of intestinal damage induced by cell-free supernatants……..….30

Figure10. Histopathological evaluation of intestinal damage in the murine ligated ileal loop model…….34

Figure11. Comparison of toxin secretion and germination efficiency between clinical and environmental *Clostridioides* isolates……35

Figure12. Principal component analysis of quantitative and histological markers of intestinal injury in the murine ileal loop model…….36

Figure113. Phylogenetic diversity among *Clostridium perfringens*…..…….48

Figure14. Experimental design for the characterization of *Clostridium perfringens*-like strains (LIBA-8541 and LIBA-8841)……53

Figure15. *In vitro* functional characterization of PLCs from LIBA-8841 and LIBA-854….64

Figure16. Cytopathic effects (CPE) induced by LIBA-8841 and LIBA-8541 strain supernatants in DonQ cell cultures……...…….65

Figure17. Cytotoxic effects induced by cell-free supernatants of LIBA-8841 and LIBA-8541 strain supernatants on Don-Q cells…….……..66

Figure18. Non-metric multidimensional scaling (NMDS) plot representing the comparative exoproteome profiles of the *Clostridium perfringens*-like isolates and two reference *C. perfringens* type A strains (JIR325, 8937; and SM101, 8380)…….69

Figure19. Tissular damage induced by Cp-like strains in a mice model of gas gangrene……71

Figure20. Evaluation of tissular damage induced by Cp-like strains in a mouse model of gas gangrene…….……..…72

LIST OF TABLES

Table1. Percentage spore germination efficiencies of *Clostridioides* strains in response to 1 % taurocholate ……..……23

Table2. Comparison of inflammatory markers in the murine ileal loop model induced by Cd-like strains according to strain origin…….……37

Table3. Main toxins produced by *C. perfringens* and their locations…….….47

Table4. Amino acid substitutions in Cp-like phospholipase C compared to critical residues of *C. perfringens* PLC…….……..…….…..63

Table5. Proteins identified in cell free supernatants from LIBA-8841 and LIBA-8541 Cp-like strain…….68

Table6. Comparative summary of *in vitro* and *in vivo* functional analyses of Cp-like strains LIBA-8541 and LIBA-8841…….……..73

SUPPLEMENTARY MATERIAL

Supplementary Figure 1. Heterogenous germination kinetics of *Clostridioides* strains in the presence of 1% taurocholate……..……..81

Supplementary Figure 2. Cytopathic phenotypes induced by Cd-like species supernatants in 3T3 cell cultures……..……..82

Supplementary Figure 3. Cytopathic phenotypes induced by Cd-like species supernatants in HeLa cell cultures……..……83

Supplementary Figure 4. Histopathological analysis of ileal tissue response induced by cell-free bacterial supernatants in the murine ligated ileal loop model……..84

Supplementary Figure 5. Biplot representation of the principal component analysis (PCA) of quantitative and histological markers of intestinal injury induced by *Clostridioides* cell-free supernatants in the murine ileal loop model…….…….85

Supplementary Figure 6. SDS-PAGE analysis of recombinant expression and purification of Cp-like PLCs from LIBA-8541 and LIBA-8841 strains in *E. coli*……..85

Supplementary Figure 7. Lecithinase activity of recombinant phospholipase C (PLC) enzymes purified from Cp-like strains…….……86

Supplementary Figure 8. Dose- and time-dependent hemolytic activity of recombinant PLCs from Cp-like strains LIBA-8541 and LIBA-8841, and *C. perfringens*……..86

Supplementary Table 1 Proteins identified in the cell-free supernatant of Cp-like strain LIBA-8841……...……87

Supplementary Table 2. Proteins identified in the cell-free supernatant of Cp-like strain LIBA-8541……..…….88

Supplementary Figure 9 Intra-strain variability of exoproteome profiles among biological replicates of the *C. perfringens*-like strains…….89

Supplementary Table 3. Proteins contributing to NMDS separation between *C.perfringens* reference strains (Cp SM101, Cp JIR325) and Cp-like LIBA-8541 and LIBA-8841……89

LIST OF ABBREVIATIONS

3T3: Mouse embryonic fibroblast cell line (NIH/Swiss 3T3)

ANOVA: Analysis of variance.

CDI: Clostridioides difficile infection

Cd-like: Genomically distinct *Clostridioides* genomospecies related to *Clostridioides difficile*

Cp-like: Genomically distinct *Clostridium* genomospecies related to *Clostridium perfringens*

CDT: binary toxin.

CPE: Cythopathic effect

ELISA: Enzyme-linked immunosorbent assay.

HeLa: Human epithelial cervical carcinoma cell line

IL1-β: Interleukin 1-β

IL6: Interleukin 6

MPO: Myeloperoxidase

PaLoc: Locus of pathogenicity

PLC: phospholipase C

SD: Standard deviation

SE: Standard error

TcdA: Toxin A

TcdB: Toxin B

TcdBv: Variant TcdB

TNF-α: Tumoral necrosis factor α

INTRODUCTION

In recent decades, the emergence and reemergence of infectious diseases have underscored the dynamic relationship between microorganisms, their hosts, and the surrounding environment. Global changes in ecosystems, antimicrobial use, and human animal interactions, among other factors, continue to shape the evolutionary landscape of pathogenic bacteria, promoting the diversification of virulence mechanisms and the emergence of novel lineages (1, 2). Within this context, bacteria of the genera *Clostridium* and *Clostridioides* remain of particular concern due to their ability to persist as dormant spores, ensuring survival and transmission across environmental, agricultural, and clinical interfaces (3, 4).

The broad ecological distribution of *Clostridium* and *Clostridioides* species highlights the need for a One Health approach to understand their ecology, evolution, and public health impact. These organisms inhabit diverse niches, including soils, aquatic environments, food sources, compost, and the gastrointestinal tracts of animals and humans (3, 5, 6). They exhibit extensive genetic versatility, characterized by large open pangenomes and high rates of lateral gene transfer mediated by phages, plasmids, and conjugative elements. Their highly dynamic genomes enable adaptation to diverse environments, where antibiotic use and other selective pressures shape their evolutionary trajectories (7, 8).

In recent years, phylogenomic analyses and comparative genomics have uncovered remarkable diversity within both *Clostridioides* and *Clostridium* (7, 9, 10). Large-scale phylogenomic reconstructions have redefined the evolutionary boundaries of these genera, revealing deep divergence between *Clostridioides difficile* and members of the *Clostridium* sensu stricto group. Within *C. difficile*, distinct phylogenetic clades have been delineated—some showing genomic distances comparable to those separating recognized bacterial species—whereas the traditional genus *Clostridium* encompasses multiple distantly related lineages, underscoring its ongoing taxonomic revision (11). This evolutionary scenario underscores the complexity and long-term diversification of spore-forming anaerobes, providing a framework to interpret their ecological versatility and pathogenic differentiation.

Clostridioides difficile and *Clostridium perfringens* stand out as leading causes of infections with distinct clinical syndromes. *C. difficile* is a major etiological agent of diarrhea,

pseudomembranous colitis, septic shock, and recurrent infections (12), whereas *C. perfringens* is associated with gas gangrene, foodborne diarrheal disease, and necrotizing enteritis in humans and diverse animal species. Despite belonging to separate evolutionary lineages, both species share a central hallmark of pathogenesis: the production of potent exotoxins that disrupt host cellular processes (13, 14). In *C. difficile*, virulence is primarily mediated by two large clostridial toxins, TcdA and TcdB, encoded within the pathogenicity locus (PaLoc) along with the binary toxin CDT, encoded in a distinct genomic region known as the CdtLoc, whose combined action leads to epithelial injury, inflammation, and colonic dysfunction (15). *C. perfringens*, by contrast, produces a repertoire of more than twenty toxins, with chromosomal encoded α-toxin (phospholipase C, PLC) representing a major determinant of virulence in gas gangrene through its ability to degrade host membranes and induce extensive tissue necrosis (16, 17).

Toxin diversity has profound biological and epidemiological implications. Sequence variation within toxin genes can modify receptor affinity, enzymatic activity, and substrate specificity, resulting in altered cytopathic effects and hosts ranges. In *C. difficile*, comparative analyses have revealed an expanding repertoire of TcdB variants with distinct autoprocessing efficiencies and glycosylation profiles, which influence disease severity and tissue tropism (18, 19). Both the PaLoc and CdtLoc exhibit high polymorphism and evidence of recombination, reflecting their mobility and extensive toxin diversity across lineages (20). Similarly, natural polymorphisms in the phospholipase C (PLC) toxin of *C. perfringens* affect catalytic efficiency and hemolytic activity, contributing to differences in virulence across strains and host species (7, 21). These molecular adaptations illustrate how subtle genetic divergence can shape the biological behavior of bacterial toxins and ultimately determine the pathogenic outcome.

The growing recognition of cryptic and divergent *Clostridioides* and *Clostridium* lineages harboring atypical toxin gene architectures (22, 23) underscores significant challenges for current diagnostic frameworks and public health surveillance. Divergence within the PaLoc and CdtLoc regions may result in altered biological activity and hinder the performance of conventional assays designed to detect canonical toxin genes or their products (24). In *C. difficile*, this genetic variability has been shown to affect the sensitivity of routine molecular

and immunological diagnostics, as reported for clade C-I strains, and may likewise influence the efficacy of antibody-based therapeutics, whose neutralizing capacity varies across TcdB subtypes (20). Similar limitations apply to *Clostridium* species, where strains lacking the classical plasmid-encoded toxins but retaining PLC are often classified as toxinotype A (10), despite representing divergent evolutionary lineages. These issues highlight the need to improve diagnostic accuracy and expand genomic surveillance to capture the full spectrum of toxigenic variants and ensure timely recognition of emerging clostridial pathogens with clinical relevance.

Understanding the pathogenicity of emerging *Clostridioides* and *Clostridium* lineages requires an integrated approach that combines molecular, phenotypic, and experimental evidence (9, 22, 25). This thesis explores the virulence and pathogenic potential of species currently in the process of classification that are phylogenetically related to *C. difficile* and *C. perfringens*, with an emphasis on their toxin-mediated effects. To this end, complementary *in vitro* and *in vivo* assays were employed to elucidate how these isolates interact with host tissues and contribute to disease-associated phenotypes.

For *Clostridioides* isolates, toxin titers, cytopathic kinetics, and substrate specificity were assessed in cell culture and integrated with an ileal loop model to evaluate epithelial injury and inflammatory responses induced by bacterial supernatants. In the case of *Clostridium perfringens*-like strains, the cytopathic, cytotoxic, and hemolytic activities of phospholipase C were analyzed across different substrates, followed by a murine gas gangrene model to assess pathogenic potential and tissue damage profiles. Collectively, this experimental framework provides a functional basis to interpret the clinical relevance of these emerging lineages and informs their potential implications for disease prevention, diagnosis, and therapeutic strategies.

These complementary approaches provide functional insights into toxin-mediated damage and host responses, contributing to a broader understanding of the evolution and emergence of pathogenic *Clostridium* and *Clostridioides* species. The isolates investigated in this work possess homologs of classical virulence factors from *C. difficile* and *C. perfringens*; however, their divergent genomic architectures and phylogenetic distance suggest potential differences in regulation, activity, and pathogenic outcomes. Based on this premise, the central

hypothesis of this thesis is that previously undescribed species within the genera *Clostridioides* and *Clostridium* exhibit distinct virulence mechanisms and pathogenic potential compared to classical pathogens. This comparative framework provides the foundation to explore how genomic divergence translates into functional and pathogenic diversity within the *Clostridium–Clostridioides* group.

SIGNIFICANCE

Advances in bacterial genomics have greatly expanded our capacity to monitor microbial evolution and detect emerging toxigenic lineages. Yet, translating this genomic information into functional and ecological understanding remains a critical challenge. Integrating genomic surveillance with ecological and clinical evidence under the One Health framework is thus essential to trace reservoirs, transmission routes, and adaptive processes that sustain toxigenic bacteria across ecosystems (3, 4).

Within this context, recent genomic investigations have uncovered an unexpected diversity among *Clostridioides* and *Clostridium* species, including novel lineages carrying toxin-encoding loci arranged in atypical genomic contexts (7, 24). These findings suggest active evolutionary processes giving rise to previously unrecognized toxigenic taxa with potential clinical and ecological relevance (9, 24–26). However, the biological properties, pathogenic mechanisms, and host interactions of these emerging species remain largely uncharacterized.

This project directly addresses these gaps by integrating molecular, phenotypic, and experimental approaches to characterize the cytopathic, histopathological, and virulence traits of previously undescribed *Clostridioides* species from clinical and environmental sources, and *Clostridium* species isolated from human infections. By assessing the activity of their toxins and their effects on host tissues, this research provides essential insights into their pathogenic potential and establishes a comparison with classical pathogens.

Overall, the study advances our understanding of pathogenic diversity among anaerobic spore-forming bacteria. The integration of genomic and functional data offers a foundation for improved diagnostic, surveillance, and therapeutic strategies, reinforcing the relevance of One Health perspectives for recognizing and mitigating (re)emerging clostridial threats across human, animal, and environmental domains. Strengthening genomic-based diagnostics and continuous environmental monitoring will be essential to detect atypical or novel toxigenic strains that may escape standard laboratory assays. Moreover, translating these insights into preventive measures and evidence-based interventions can support public health systems in anticipating outbreaks and mitigating cross-sectoral transmission risks.

HYPOTHESIS

Previously undescribed species within the genera *Clostridioides* and *Clostridium* that harbor homologs of classical virulence factors exhibit distinct virulence mechanisms and pathogenic potential compared to *C. difficile* and *C. perfringens.*

GENERAL OBJECTIVE

To phenotypically compare the virulence and pathogenicity of environmental and clinical isolates from three novel species phylogenetically related to *C. difficile* producing TcdB and two novel species phylogenetically related to *C. perfringens* producing alpha toxin.

SPECIFIC OBJECTIVES

1. To evaluate the spore's germination, toxin activity, GTPase substrate specificity, of TcdB variants, cytopathic effect, and tissue damage of isolates from novel species related to *C. difficile* to elucidate their pathogenic mechanisms.

2. To compare the pathogenicity and virulence of clinical and environmental isolates from three novel *C. difficile*-related species to identify origin-specific differences and potential adaptations to the human host.

3. To phenotypically characterize the multifactorial pathogenicity of two novel *C. perfringens*-related species, with emphasis on the activity of their divergent phospholipase C.

CHAPTER 1

Previously undescribed species phylogenetically related to *Clostridioides difficile*

1.1 State of the Art

1.1.1Clostridioides difficile

Clostridioides difficile is a Gram-positive, spore-forming, obligate anaerobe that is widely distributed in nature. It can be isolated from soil, water, and the feces of humans and animals, reflecting its remarkable environmental persistence and ecological versatility (27). *Clostridioides difficile* infections (CDI) comprise a clinical spectrum ranging from mild diarrhea to pseudomembranous colitis, toxic megacolon, and frequent recurrence. Conventionally, CDI were considered nosocomial infections associated with prolonged use of broad-spectrum antimicrobials, hospitalization, and advanced age (28). In recent decades, however, an increasing number of community-acquired cases have been reported, affecting previously healthy individuals with no recent history of hospitalization or antibiotic exposure. This epidemiological shift underscores the complexity of *C. difficile* reservoirs and the need to understand its ecological dynamics beyond the clinical setting (23, 29, 30)

C. difficile spores display exceptional persistence in the environment, conferring resistance to disinfection and promoting fecal–oral transmission. Due to its clinical impact and growing antimicrobial resistance, *C. difficile* has been classified by the U.S. Centers for Disease Control and Prevention (CDC) as an urgent public health threat (3, 31). Infection begins with the ingestion of spores that transit through the gastrointestinal tract until reaching the ileum, where germination predominantly occurs. This step is critical for pathogenesis and subsequent colonization. Following the establishment in the intestine, the pathogenesis is driven by the coordinated action of toxins and other virulence determinants (12, 32).

1.1.2 CDI pathogenesis

Spore germination and colonization

Disruption of the gut microbiota plays a crucial role in the establishment of *Clostridioides difficile* infection (CDI). This dysbiosis alters the concentration and profile of bile acids within the colon, creating a favorable environment for spore germination (33). Germination is regulated by multiple factors. It has been described to be favored at 37 °C, within a pH

range of 6.5–8.5, and induced by primary bile acids, such as taurocholate, in conjunction with co-germinants including glycine, specific amino acids, and calcium ions (34, 35).

The germinant receptors CspA and CspC are pseudoproteases that, upon activation, are hypothesized to relieve the inhibition of the protease CspB. Sbubsequent to this, activated CspB cleaves and activates the cortex-lytic enzyme SleC, thereby initiating the degradation of the spore cortex, the release of calcium dipicolinate, and the rehydration of the core, ultimately leading to vegetative outgrowth. In contrast, secondary bile acids have been shown to inhibit this process, thereby conferring colonization resistance (36).

Once germinated, colonization of the intestinal epithelium is facilitated by secreted mucolytic enzymes and surface-associated adhesins that promote bacterial attachment. Vegetative forms of *C. difficile* can transition between motile and sessile states, enhancing their ability to form biofilms on epithelial surfaces. Additionally, cell–cell signaling mechanisms have been described as coordinating the expression of colonization and virulence factors, thereby further promoting persistence and disease development (37).

Toxins secretion

Although multiple virulence factors contribute to *C. difficile* pathogenesis, the clinical symptoms of infection are in most strains associated with the presence of a toxin-encoding pathogenicity locus (PaLoc) encoding two large homologous exotoxins: TcdA and TcdB, as well as three accessory genes (*tcdR, tcdE*, and *tcdC*) which presumably regulate toxin synthesis and export (38, 39).

TcdA and TcdB are single-chain polypeptides composed of four functional domains: an N-terminal glycosyltransferase domain (GTD) responsible for inactivating host Rho GTPases by glucosylation; an autoprotease domain (APD) that mediates self-cleavage and toxin maturation; a delivery and receptor-binding domain (DRBD) that facilitates translocation and receptor interaction; and a C-terminal combined repetitive oligopeptides (CROPs) region that also contributes to receptor binding and cellular specificity (15).

Toxin expression is modulated by various environmental and physiological cues, including temperature, subinhibitory concentrations of certain antibiotics, quorum-sensing signals, short-chain fatty acids, the presence of rapidly metabolizable carbon sources, and specific

amino acids. Notably, so-called “hypervirulent” or epidemic strains have been linked to increased disease severity and mortality, largely due to toxin overproduction, often associated with mutations in the *tcdC* negative regulator (40, 41). Historically, TcdA was characterized as the enterotoxin responsible for enterocolitis and was described as potentiating the effects of TcdB; however, accumulating evidence demonstrates that TcdB alone is sufficient to induce severe disease, emphasizing its pivotal role in CDI pathogenesis (42).

Mode of Action of TcdB

TcdB exerts its cytotoxic effects through a multistep process initiated by receptor-mediated endocytosis. The CROPs domain binds to host receptors, such as chondroitin sulfate proteoglycan 4 (CSPG4), abundant in the subepithelial layer and at epithelial junctions, and low-density lipoprotein receptor-related protein 1 (LRP1), in colonic epithelial cells. The DRBD interacts with Frizzled receptors (FZD1, FZD2, and FZD7) and the tissue factor pathway inhibitor (TFPI), whereas regions outside the CROPs domain recognize Poliovirus Receptor-Like 3 (PVRL3), highly expressed on colon epithelial surfaces (15, 19).

The receptor repertoire of TcdB has important biological implications (43). First, receptor abundance and tissue distribution determine toxin accessibility and organ tropism. Second, distinct binding sites for CSPG4 and FZDs may enable simultaneous engagement on the same cell surface. Third, several of these receptors, such as FZDs, participate in key signaling pathways governing epithelial renewal and homeostasis. Finally, receptor internalization and recycling dynamics may further influence toxin uptake (19).

Upon endocytosis, acidification within endosomes triggers conformational rearrangements, leading to pore formation and translocation of the glycosyltransferase (GTD) and autoprotease (APD) domains into the cytosol. Once released, the GTD inactivates small GTPases of the Rho and Ras families through glycosylation, thereby disrupting key regulatory pathways within the host cell. Rho GTPases primarily control actin cytoskeleton organization, while Ras GTPases regulate cell differentiation, proliferation, angiogenesis, and adhesion. Consequently, their inactivation results in cytoskeletal collapse and ultimately cell death (19, 42, 43).

Cytopathic and cytotoxic effects

TcdB induces rearrangements of the actin cytoskeleton, resulting in morphological alterations known as cytopathic effects (CPE). A classic CPE, or arborizing effect, occurs when stress fibers and focal adhesions are lost, resulting in the formation of neurite-like retraction fibers. Disruption of actin-anchored structures causes cell rounding and detachment from the extracellular matrix. Variant cytopathic responses have been described for certain TcdB subtypes, characterized by rapid cell rounding without protrusion formation, resembling the effect of *C. sordellii* lethal toxin (TcsL) (44, 45). These differences are attributed to variations in substrate targeting. The classical CPE is associated with RhoA glucosylation, whereas the variant phenotype involves transient RhoA activation and inactivation of R-Ras and Rac1 GTPases. The collapse of the actin cytoskeleton ultimately leads to the disassembly of epithelial tight junctions and the loss of barrier integrity (15, 39, 44).

In addition to its cytopathic effects, TcdB exhibits potent cytotoxicity in various cell types, including epithelial and endothelial cells, monocytes, lymphocytes, and enteric neurons. Cell death occurs through diverse mechanisms, including caspase-dependent and -independent apoptosis involving cytochrome c release and p53 activation, necrosis associated with reactive oxygen species (ROS) accumulation, and pyroptosis in myeloid-derived immune cells (19, 44). The predominant cytotoxic pathway appears to depend on toxin concentration and cellular context.

Overall, TcdB disrupts epithelial junctions and induces epithelial cell death, directly damaging the colonic mucosa. Moreover, it stimulates epithelial cells to secrete proinflammatory cytokines and neutrophil chemo attractants, triggering acute innate inflammation (46).

CDI immune response

The inflammatory response in *C. difficile* infection originates from the action of toxins on intestinal epithelial cells and is primarily mediated by activation of the innate immune system. TcdB induces the release of proinflammatory mediators, including interleukin-8 (IL-8), interleukin-1β (IL-1β), monocyte chemoattractant protein-1 (MCP-1), and interleukin-6 (IL-6), from colonic epithelial cells, monocytes, and macrophages, and this release correlates with disease severity (15, 47). These mediators promote the recruitment of neutrophils and monocytes to the colonic lamina propria, leading to epithelial injury and fluid secretion (48).

Excessive polymorphonuclear infiltration contributes to extensive tissue damage, and marked neutrophilia is associated with poor clinical outcomes (27). Additionally, TcdB amplifies inflammation by activating dendritic cells, group 3 innate lymphoid cells, and mast cells, which release TNF-α, IL-8, and histamine, further exacerbating mucosal damage. The inflammatory response itself is largely responsible for the pathological manifestations of CDI (42).

Binary toxin CDT

The binary toxin, also known as cytolethal distending toxin (CDT), is produced by approximately 20% of *C. difficile* strains and is encoded by the *cdtA* and *cdtB* genes, located in a chromosomal region distinct from the PaLoc. CDT is an actin-targeting ADP-ribosyltransferase that binds to the lipolysis-stimulated lipoprotein receptor (LSR) to enter host cells. Once inside the cytosol, it ribosylates G-actin, blocking polymerization and causing cytoskeletal collapse. This disruption leads to cell rounding, loss of tight junction integrity, and impaired cells migration (19, 42). Additionally, CDT induces microtubule redistribution and the formation of epithelial protrusions that facilitate bacterial adherence and colonization (49).

Beyond cytoskeletal alterations, CDT triggers proinflammatory responses, including IL-1β release, eosinophil apoptosis, and activation of mucosal-associated invariant T cells. Although its contribution to disease severity remains debated, CDT is frequently present in "hypervirulent" and community-acquired *C. difficile* strains associated with poor clinical outcomes. Detection of CDT^+ strains remains limited, as standard diagnostic assays solely target TcdA and TcdB (49, 50).

1.1.3 Diagnostic and Typing Methods

The diagnosis of CDI relies on detecting toxins or their genes in stool samples. The cytotoxicity assay on cell culture remains the gold standard; however, due to its technical complexity, current diagnostic algorithms combine enzyme immunoassays (EIAs) for toxin A (TcdA), toxin B (TcdB), and glutamate dehydrogenase (GDH) with nucleic acid amplification tests (NAATs) targeting toxin genes (*tcdA*, *tcdB*), the regulatory *tcdC* gene, and, in some cases, the binary toxin genes (*cdtA* and *cdtB*). Given their high sensitivity,

molecular results must be carefully interpreted to distinguish true CDI from asymptomatic colonization (5, 49, 51).

Molecular typing of *C. difficile* is essential for epidemiological surveillance and for understanding strain diversity. Classical genotyping methods—such as PCR ribotyping, pulsed-field gel electrophoresis (PFGE), multilocus variable-number tandem repeat analysis (MLVA), multilocus sequence typing (MLST), and toxinotyping—have provided critical insights into strain distribution, pathogenic potential, and outbreak tracking (9). Toxinotyping, in particular, enables the characterization of genetic variability within the *tcdA* and *tcdB* loci. To date, at least twelve TcdB subtypes have been described using average linkage hierarchical clustering, exhibiting differences in receptor binding, autoprocessing, and substrate specificity that modulate cytopathic effects and virulence (18). These variations have been experimentally associated with distinct pathogenic outcomes in animal infection and ileal loop models (52). Such molecular diversity also poses significant challenges for diagnostic assay design, therapeutic strategies, and vaccine development.

High-resolution molecular approaches, including MLST, whole-genome sequencing (WGS), single-nucleotide polymorphism (SNP) analysis, and pangenome comparisons, have deepened the phylogenetic understanding of *C. difficile*, highlighting extensive genomic variation within the *Clostridioides* genus (9). Based on MLST data, the population structure of *C. difficile* has been classified into five major clades and at least three cryptic clades (C-I, C-II, and C-III), displaying distinct genomic and toxin gene configurations (5).

1.1.4 Genomic Diversity and Emerging Species within the *Clostridioides* Genus

Genomic surveys from underexplored ecological sources—including soil, aquatic environments, compost, plants, and invertebrates—have uncovered an unexpected breadth of diversity among *Clostridioides* species (5, 6, 22). This wide distribution suggests ecological roles that extend beyond mammalian infection, although these organisms remain primarily adapted to animal hosts. Comparative genomic analyses based on average nucleotide identity, pangenome composition, and Bayesian inference have revealed significant taxonomic incongruities within *C. difficile*, supporting the reclassification of cryptic clades C-I–C-III as

distinct genomospecies (Figure 1). More recent phylogenomic studies of environmental and clinical isolates have further refined this framework, identifying up to eight novel *Clostridioides* genomospecies (23, 24).

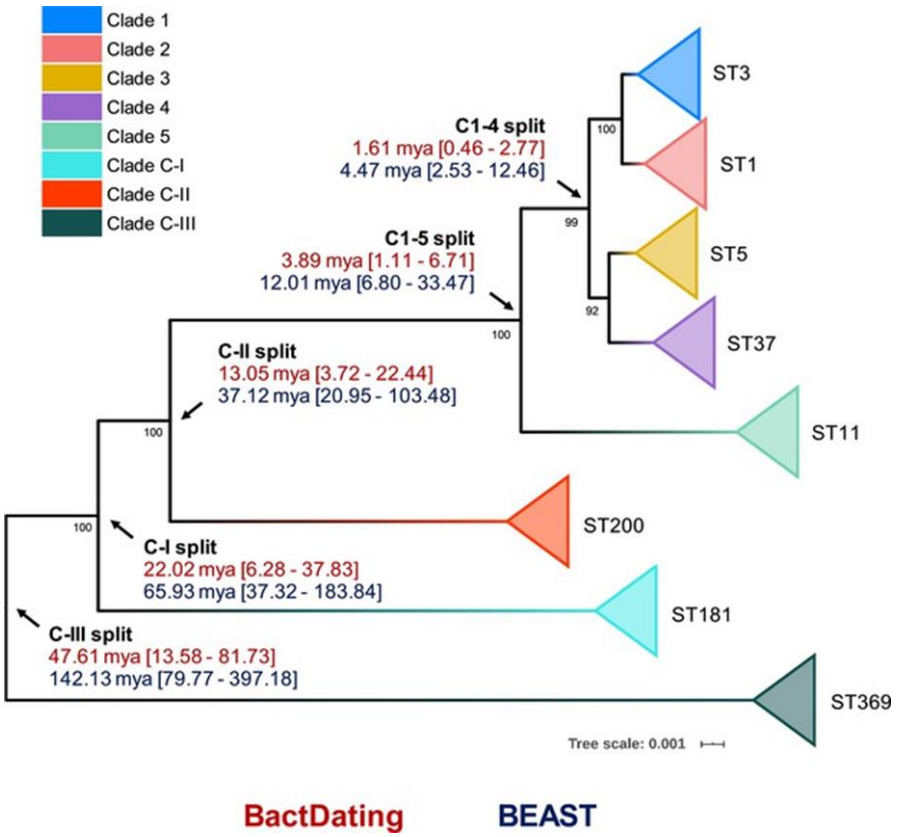

Figure 1. Phylogenetic relationships within the *Clostridioides* genus based on average nucleotide identity (ANI). BactDating and BEAST estimates of the age of major *C. difficile* clades. Taken from Knight et al., 2021 (eLife)(24).

These lineages exhibit extensive genomic divergence, particularly in toxin gene organization. Homologs of *tcdA* and *tcdB* have been identified within cryptic species genomes but occur in genomic contexts distinct from the canonical *C. difficile* PaLoc; frequently, isolates from these genomospecies are *tcdA*- and *tcdC*-negative. Moreover, atypical variants of *cdtA* and *cdtB* are frequently present on phages and plasmids, reflecting marked structural and functional divergence across these lineages (23, 24). Such divergent loci often escape detection by standard PCR assays, suggesting that their prevalence may have been underestimated (53). Furthermore, homologues of regulatory elements (*tcdR*, *cdtR*) also display unique sequences potentially affecting toxin expression (23, 24). These genomic

features highlight the evolutionary plasticity of virulence factors and pose challenges for diagnostic and vaccine development.

Beyond virulence genes, comparative genomics has identified alternative metabolic pathways absent in *C. difficile* from classical clades 1 to 5, likely reflecting adaptations to distinct ecological niches and long-term diversification shaped by environmental pressures (24). The recovery of toxigenic isolates from soil, water, animals, and human diarrheal samples underscores the public health relevance of environmental reservoirs (5, 22, 54). Multiple studies therefore provide a robust genomic framework to explore the diversity of emerging *Clostridioides* species; however, this genomic expansion has not been matched by functional characterization.

To date, phenotypic descriptions of cryptic clades have been largely restricted to a small number of human fecal isolates from clade C-I, which were shown to induce cytopathic effects, display variable cytotoxicity, and cause differential mortality in hamster models (20). Consequently, the functional diversity of these lineages and their implications for pathogenic mechanisms, clinical presentation, and disease severity remain poorly understood. This gap is particularly concerning because cryptic *Clostridioide*s lineages may evade routine diagnostic assays due to divergent toxin sequences and may differ in clinical presentation and responses to treatment (53). Collectively, these considerations underscore the need for sustained genomic surveillance complemented by targeted phenotypic analyses and *in vitro* and *in vivo* studies to accurately define their pathogenic potential. Lineages initially identified as cryptic clades and subsequently recognized as distinct genomospecies within the genus *Clostridioides* remain largely uncharacterized at the functional level. In the present study, isolates belonging to these genomically distinct lineages and phylogenetically related to *C. difficile* are hereafter referred to as **Cd-like strains**, reflecting their genetic relatedness to *C. difficile* and their divergence from classical clades.

1.2 Materials and Methods

To characterize the mechanisms underlying the pathogenicity of the previously undescribed *Clostridioides* genomospecies (Cd-like), a combined experimental strategy integrating *in vitro* and *in vivo* approaches was implemented. The study included clinical isolates recovered from human fecal samples and environmental isolates obtained from soil, which were

assigned to cryptic clades C-I, C-V, and C-VII based on WGS (unpublished data). The *in vitro* component is focused on spore germination kinetics, the production of toxins, the cytopathic effect, and substrate specificity in cell cultures. The *in vivo* component employed a murine ileal loop model to evaluate epithelial injury and acute inflammatory responses induced by bacterial supernatants. Figure 2 summarizes the overall methodology.

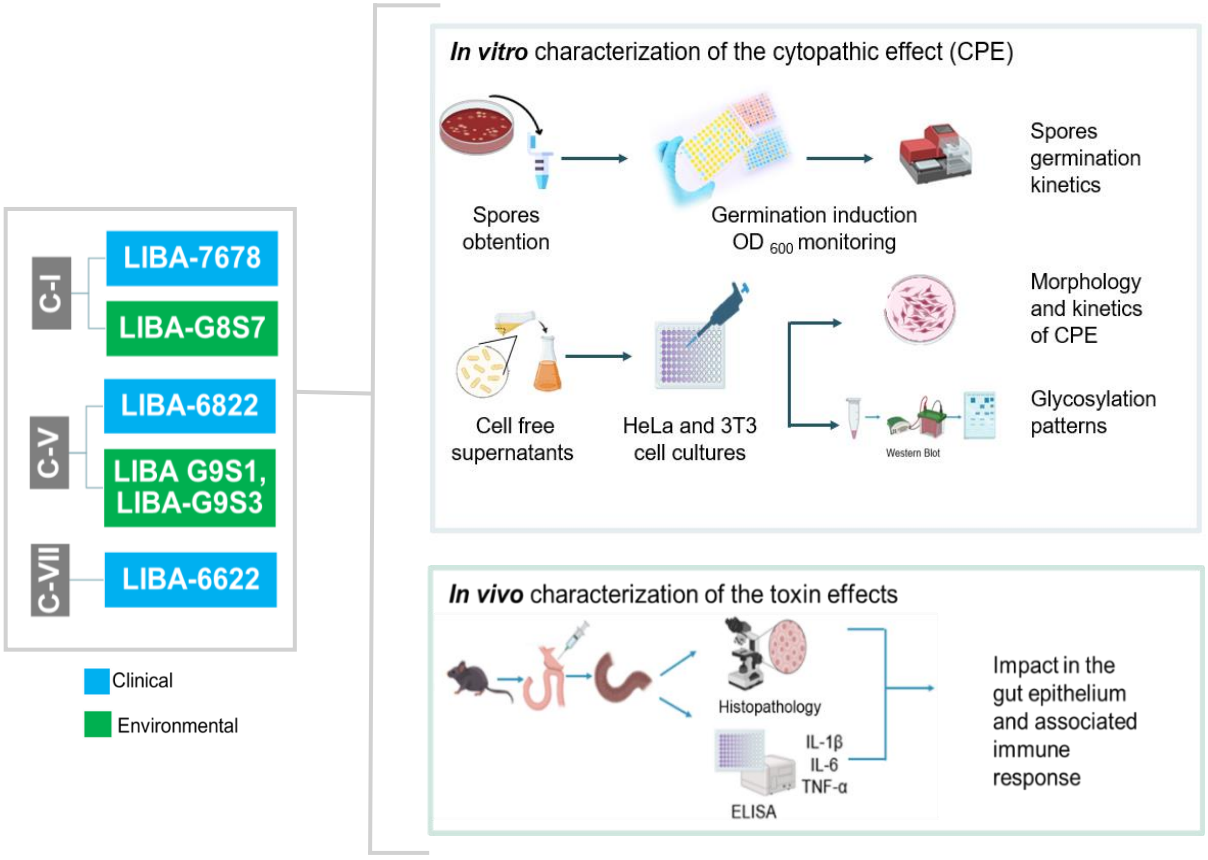

Figure 2. Experimental design for the characterization of *Clostridioides* genomospecies related to *C. difficile*. The study included both clinical (blue) and environmental (green) isolates representing genomospecies C-I, C-V, and C-VII. The experimental workflow comprised *in vitro* assays to evaluate spore germination kinetics, cytopathic effects, and toxin activity in cell cultures, as well as *in vivo* analyses using an ileal loop model to assess epithelial damage and inflammatory responses induced by bacterial supernatants.

1.2.1 Bacterial strains

This part of the study was conducted using isolates classified as representatives of genomospecies within the genus *Clostridioides*, previously identified as cryptic clades referred to as Cd-like strains. The isolates included LIBA-7678 (C-I), LIBA-6822 (C-V), LIBA-G9S1 (C-V), LIBA-G9S3 (C-V), LIBA-6622 (C-VII), and the non-toxigenic strain LIBA-G8S7 (C-I). Numerical codes correspond to clinical isolates, whereas codes containing the prefix "G" denote soil strains. All isolates were deposited in the Anaerobic Bacteriology Research Laboratory (LIBA) strain collection.

Clinical isolates were obtained from diarrheal stool samples of patients with suspected CDI, submitted to LIBA for confirmation. These isolates tested negative in a multiplex PCR for the presence of the *tcdC* gene, a PaLoc marker (unpublished data). Isolates recovered from soil were collected during 2022 at sites exhibiting minimal human activity within the Protected Areas Network of the University of Costa Rica. Soil samples were obtained using disinfected shovels at locations at least 5 m away from the nearest trail or road. To minimize external contamination and ensure that samples reflected native soil bacterial communities, the upper 5–10 cm of soil and surface vegetation were removed prior to collection. Soil suspensions were subsequently heat-treated and inoculated onto ChromeID plates (bioMérieux).

The identification of these isolates was achieved using a combination of phenotypic and molecular methods, including a latex agglutination test (Oxoid™ *Clostridium difficile* Test Kit), PCR detection of the *tpi* gene as a species-specific marker (20), MALDI-TOF mass spectrometry, and whole-genome sequencing. Genome sequencing was performed using paired-end sequencing on an Illumina platform. Whole-genome relatedness was initially assessed by computing alignment-free average nucleotide identity (ANI) values using FastANI.

The Type (Strain) Genome Server (TYGS) (55) was employed to calculate digital DNA–DNA hybridization (dDDH) values and complementary ANI metrics in order to determine whether the LIBA isolates corresponded to *C. difficile* or to other *Clostridioides* species. TcdB subtypes were identified using the BLAST algorithm implemented in Diffbase (18) (unpublished data).

Genomic analyses revealed the presence of the *tcdB* gene (except in strain LIBA-G8S7) and the binary toxin (*cdtAB*) locus in most strains, together with the absence of *tcdA* and *tcdC*. Sequence analysis classified the TcdB variants of the novel genomospecies as plasmid-encoded TcdB7, except for strain LIBA-6622, which harbors a chromosomally encoded TcdB11.

As reference strains, two *C. difficile* Clade 2 isolates were included: the hypervirulent strain R20291 (56), which induces a classical cytopathic effect, and LIBA-5757, carrying a variant TcdB toxin that causes a *C. sordellii* phenotype.Both have been extensively characterized in *in vitro* and *in vivo* models and served as benchmarks for comparative virulence analysis (40, 57). All isolates were maintained in cryopreservation at –80 °C as part of the LIBA strain collection.

1.2.2 Spores germination kinetics

Spore germination assays were conducted as previously described (58, 59). Spores were obtained from confluent cultures grown anaerobically for seven days on ten blood agar plates per strain. The colonies were harvested, resuspended in phosphate-buffered saline (PBS), and centrifuged for 20 min at 4,000 rpm. The resulting pellets were washed once with PBS, subsequently subjected to heat treatment at 60 °C for 10 min to eliminate vegetative cells, and centrifuged again under the same conditions. Pellets were resuspended in Dulbecco's Modified Eagle Medium (DMEM), and aliquots were stored at −80 °C until use. Prior to the assay, purified spore suspensions were adjusted in brain heart infusion (BHI) broth to an optical density (OD_{600}) of ~0.89.

Thereafter, 180 µL of each spore suspension was dispensed in triplicate into 96-well microplates. Taurocholate was added to achieve final concentrations of 0%, 0.25%, and 1%, in a final volume of 200 µL containing 1 mM glycine and 50 µM $CaCl_2$. The 0% condition was used as a negative control, with water replacing taurocholate. Germination was monitored by measuring the decrease in OD_{600}, with readings taken every 3 min over a 1.5 h period at 37°C in a Synergy HT Biotek microplate reader, with continuous shaking throughout the assay.

The change in OD_{600} from baseline (t=0) to the minimal value was used to calculate germination efficiency, expressed as the mean percentage (±SD) for each isolate.

1.2.3 Obtention of cell-free supernatants

Growth curves were performed using a standardized inoculum adjusted to 0.5 McFarland in 250 mL of Brain Heart Infusion (BHI, Oxoid™) broth to determine the time point at which cultures reached approximately 5×10^7 CFU/mL in the stationary phase. Cultures were incubated at 37 °C under anaerobic conditions in an atmosphere composed of 90% N_2, 5% H_2, and 5% CO_2 using an anaerobic chamber (Bactron II; Shell Lab). At the stationary phase, culture media were centrifuged at 4,000 rpm for 30 min, and supernatants were filtered through 0.2 µm membrane filters to obtain cell-free supernatants which were aliquoted and stored at −80 °C until further use.

1.2.4 Toxin quantification in cell-free supernatants

Tenfold serial dilutions of cell-free supernatants were added to 85% confluent monolayers of HeLa and 3T3 cell lines grown in Dulbecco's Modified Eagle Medium (DMEM, Gibco™). Toxin concentration was expressed as the reciprocal of the highest dilution causing 50% cytopathic effect (CPE_{50}) in the monolayer after 24 h of incubation at 37 °C, determined by direct microscopic observation of the cultures (57). To confirm that the effect was caused by Toxin B, a neutralization assay was performed under the same conditions with the addition of a polyclonal anti-TcdB/TcdA antibody (TechLab, Blacksburg, VA).

1.2.5 Evaluation of cytopathic effect

The cytopathic effect (CPE) induced by cell-free supernatants on confluent HeLa and 3T3 monolayers was monitored by light microscopy over a 20 h period. Morphological and kinetic evaluation of CPE was performed using bright-field microscopy images acquired with a BioTek Lionheart FX Automated Microscope (60) during continue incubation at 37 °C**.**

1.2.6 Determination of the glycosylation pattern of Toxin B

Cell-free supernatants were used to intoxicate four wells of a 24-well plate containing HeLa cells at 85% confluence in DMEM for 24 h. After treatment, the monolayers were resuspended and centrifuged for 10 min at 1,250 rpm (4 °C). The resulting pellets were lysed with 2% SDS by heating at 90 °C for 20 min (20). Protein concentration was determined with the Bradford method (Appendix 1). Approximately 10 µg of protein per condition were separated by molecular weight using 10% SDS-PAGE (Appendix 2), followed by Western blotting (Appendix 3) with specific primary antibodies such as anti-RhoA antibody mouse monoclonal (abcam ab54835), Purified Mouse anti-Rac1 (Biosciences610651) and α-Actinin (D6F6) XP Rabbit (Cell Signaling Technology mAb 6487). For signal detection, anti-mouse and anti-rabbit HRP-conjugated secondary antibodies (Life Technologies™) were used, and chemiluminescence was recorded with a ChemiDoc Imaging System (Bio-Rad®).

1.2.7 Characterization of epithelial damage and immune response induced by cell-free supernatants

The murine ligated ileal loop model (40, 61) (Appendix 4) was used to described the tissue damage and immune response induced by Cd-like strains. Briefly, bacteria-free supernatants were prepared as described above from standardized overnight cultures in BHI. Four-week-old Hsd:ICR mice (approximately 20 g) were injected with 0.1 mL of supernatant into ligated ileal loops. Four hours post-inoculation, the mice were euthanized. To assess damage severity, the weight-to-length ratio of the loops (mg/cm) was determined. Then, each loop was divided into three sections for subsequent analyses:

Myeloperoxidase activity: Tissue was homogenized in hexadecyltrimethylammonium bromide (HTAB, Sigma) buffer (PBS, 50% w/v HTAB, and 0.1% v/v H_2O_2) to measure myeloperoxidase (MPO) activity, expressed as MPO U/100 mg (Appendix 5)(40).

Cytokine quantification: Another tissue portion was homogenized in PBS containing protease inhibitors (cOmplete™ Protease Inhibitor Cocktail, Roche) for the determination of TNF-α, IL-1β, and IL-6 concentrations (pg/mg) by quantitative enzyme-linked immunosorbent assay (ELISA) assays, according to manufacturers´

protocols respectively: 88-7324, 88-7013A, 88–7064, (Invitrogen, USA). Samples were stored at –80 °C until processing.

Histopathological analysis: A third tissue section was formalin-fixed and embedded in paraffin. Hematoxilin/Eosin (H/E) staining was employed to analyze 4 µm-thick sections of intestinal tissue at the Pathology Laboratory of Clínica Bíblica Hospital. Histopathological evaluation was conducted in a single-blind manner. For each tissue sample, inflammation, edema, hemorrhage, and epithelial damage (including desquamation, ulceration, and alterations in epithelial architecture) were evaluated (Appendix 6). Subsequently, a score was then assigned according to severity and the percentage of affected area using the following scale: 0 = no alterations; 1 = <25% of the area affected; 2 = 25–50%; 3 = 50–75%; and 4 = >75% of the area with severe alterations. The individual scores assigned to each parameter were summed to calculate an overall severity index for each sample (62).

All animal proceedings were in compliance with local legislation (Ley de Bienestar de los Animales N° 7451) and approved by the Comité Institucional de Cuido y Uso de Animales (CICUA) from the Universidad de Costa Rica (CICUA 73-2023).

1.2.8 Comparative Analysis of Tissue Damage Parameters Across Strain Origins

Quantitative scores (weight/length ratio, MPO activity, and cytokine concentrations), together with overall histopathological severity scores, were used for multivariate exploratory analysis. When more than five measurements were available per group, a single extreme value showing marked deviation from the remaining observations was excluded to maintain a consistent sample size across groups. Values were then categorized into four ordinal classes based on interquartile ranges corresponding to the 0.25, 0.50, 0.75, and 1.0 percentiles. Each individual measurement was assigned a numerical value corresponding to its category, thereby standardizing all parameters on a comparable scale and enabling an integrated comparison of tissue damage and inflammation severity across strains.

A principal component analysis (PCA) was performed in GraphPad Prism 10.6.1 to evaluate similarities and differences in tissue alterations among strains and origins. Samples were grouped according to the strain origin—clinical vs. environmental, *C. difficile*, or Cd-like

LIBA-G8S7 (non-toxigenic)—and the first two principal components (PC1 and PC2) were plotted to visualize clustering patterns.

To compare the contribution of individual histopathological features to intestinal damage, mean scores for epithelial desquamation, ulceration/erosion, hyperplasia, crypt alterations, villus damage, inflammation, edema, and hemorrhage were plotted in a radar graph generated using Microsoft Excel. Groups were defined according to the origin of the corresponding strains.

1.2.9 Statistical analysis

Statistical analyses were performed using GraphPad Prism version 10.6.1 and SigmaPlot version 16. Data distribution was assessed using the Shapiro–Wilk test, and homogeneity of variances was evaluated using Levene's test. Parametric or non-parametric tests were selected accordingly, including one-way ANOVA with appropriate post hoc multiple-comparison tests or Kruskal–Wallis analysis, as appropriate. Results are expressed as mean ± SD unless otherwise specified, and differences were considered statistically significant at $p < 0.05$..

1.3 Results

Cd-like strains exhibited variable germination efficiencies in response to bile salts and co-germinants

The germination kinetics of *Clostridioides* genomospecies strains were assessed by monitoring optical density in response to taurocholate (TA), glycine, and $CaCl_2$, which have been previously described as the most effective germinant for *C. difficile* spores (36, 58). *C. difficile* R20291 showed a classical germination profile, marked by a with rapid decreased in optical OD600, during the first initial 20 minutes of incubation. This decline signifies the transition from spores to vegetative cells. Germination efficiency in this reference strain increased in a concentration-dependent manner with TA (Fig. 3A).

Under the tested conditions, TA was essential to trigger germination in all Cd-like genomospecies, and a dose–response effect was evident except for strain LIBA-6622 (Fig. 3C). the largest OD_{600} reduction occurred early in the assay, although the magnitude of germination varied among strains. Notably, LIBA-G8S7 did not exhibit a consistent pattern

under any of the conditions tested and could not be associated with typical germination kinetics (Fig. 3).

Among the isolates, LIBA-7678 showed the lowest germination efficiency (10.558 ± 0.594), whereas LIBA-6822 displayed the highest (27.566 ± 0.086). LIBA-G9S1, and LIBA-G9S3—classified as C-V—exhibited 23.458 ± 1.345 and 25.807 ± 1.807 efficiencies respectively whereas *C. difficile* shows 22.319 ± 0.480. However, these differences did not reach statistical significance, as determined by a Kruskal–Wallis analysis of variance on ranks ($p = 0.062$) (Table 1).

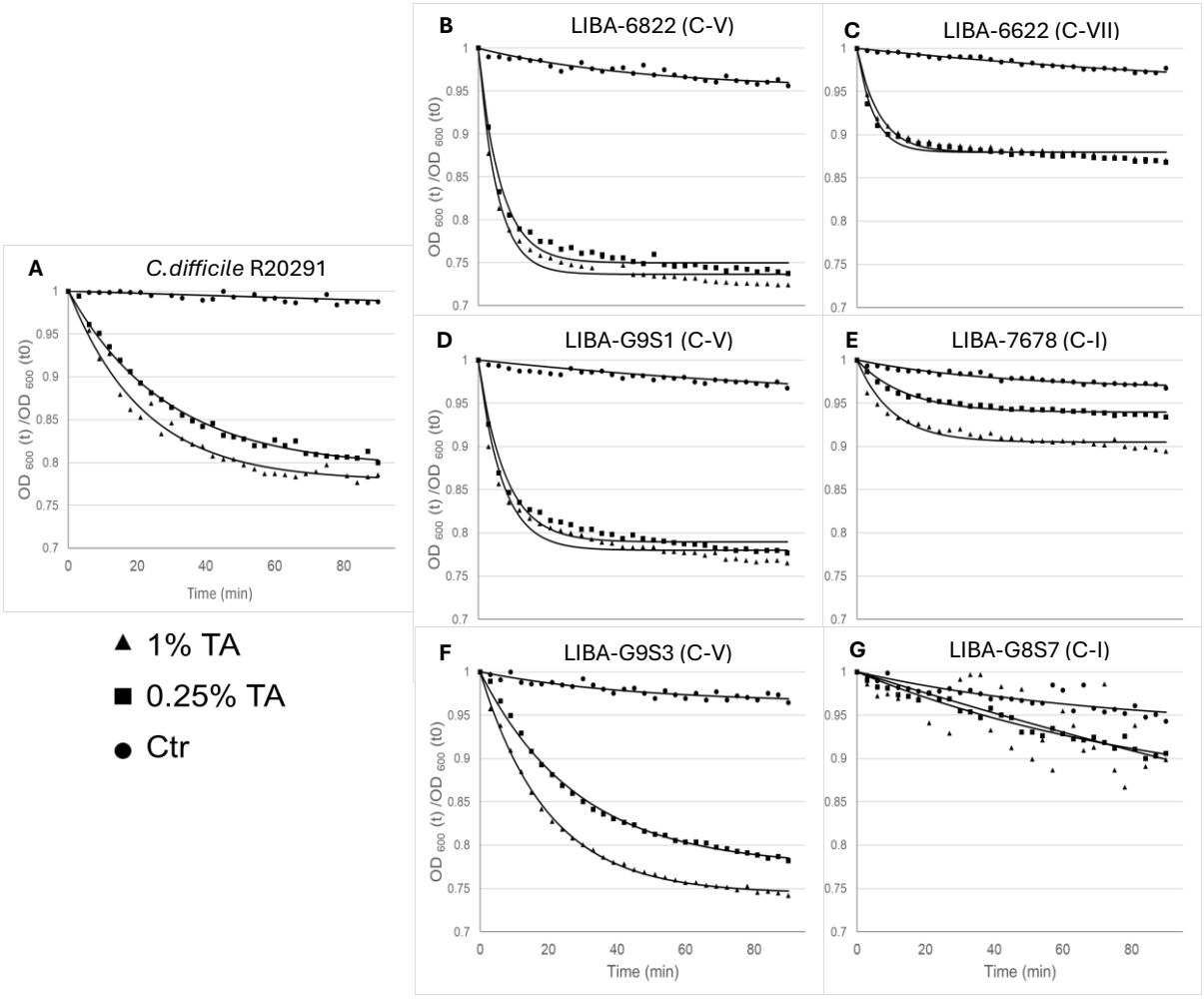

Figure 3. Germination kinetics of *Clostridioides* strains in response to taurocholate. Purified spores suspensions were incubated in BHI supplemented with glycine (1 mM) and $CaCl_2$ (50 µM), and germination was monitored as a decrease in OD_{600} over 90 min. Taurocholate (TA) was added at final concentrations of 0%, 0.25%, or 1%. *C.difficile* R20291 was used as positive control.

Table 1. Percentage spore germination efficiencies of *Clostridioides* strains in response to 1 % taurocholate. Germination efficiency was calculated based on the loss of OD_{600}, determined as the difference between the optical density at time zero and the minimum OD_{600} value reached during germination. Differences among strains were not statistically significant (Kruskal–Wallis, p = 0.062).

Strain		% germination efficiency by loss of OD_{600} nm
		Mean ± SEM
LIBA-7678	C-I	10.558 ± 0.594
LIBA-6622	C-VII	13.057 ± 0.580
LIBA-6822	C-V	27.566 ± 0.086
LIBA-G9S1	C-V	23.458 ± 1.345
LIBA-G9S3	C-V	25.807 ± 1.807
LIBA-G8S7	C-I	14.276 ± 0.929
C.difficile R20291	Clade 2	22.319 ± 0.480

Supernatants of Cd-like strains induced CPE in a strain- and cell type–dependent manner

Toxin titters in both cell lines revealed differences in TcdB secretion levels between the new genomospecies and *C. difficile* R20291 (Fig. 4). In HeLa cells, clinical isolates showed CPE_{50} values ranging from approximately 2.0–2.5, whereas environmental strains reached approximately 3.0–3.3, which remained below the reference strain R20291 (~4). A similar pattern was observed in 3T3 cells, where environmental isolates displayed marginally elevated titers (~3.0–3.2) in comparison to clinical ones (~2.2–2.5). These differences were not statistically significant among the Cd-like strains in 3T3 cells (Kruskal–Wallis, p = 0.094), although significance was reached in HeLa cells (Fig. 4). Cell rounding was consistently prevented by pre-incubation with a polyclonal anti-TcdB/TcdA antibody, confirming that the observed CPE was toxin mediated (data not shown).

CPE was monitored at hourly intervals for a period of 20 h in both 3T3 fibroblasts and HeLa cells. These assays also revealed varying potencies among the tested supernatants, which appeared to be cell line specific. Across all strains, including controls, the kinetics of CPE were higher in 3T3 cells compared to HeLa (Fig. 5). Strain-specific differences were even more pronounced in 3T3 fibroblasts. *C. difficile* R20291 induced the fastest CPE, reaching 100% within less than 3 h. Environmental strains displayed consistently faster CPE kinetics than clinical isolates. Moreover, LIBA-G9S1 and LIBA-G9S3 reached 75–100% CPE

between 4 and 10 h in both cell lines. In contrast, clinical isolates exhibited delayed CPE induction: LIBA-6822 showed the slowest progression and did not reach 100% CPE in 3T3 cells, whereas LIBA-6622 achieved full rounding in HeLa cells by ~6 h but reached only ~75% in 3T3 cells after 20 h (Fig. 5). These findings are consistent with previous observations of differential expression of surface receptors for TcdB in different cell types (57, 63).

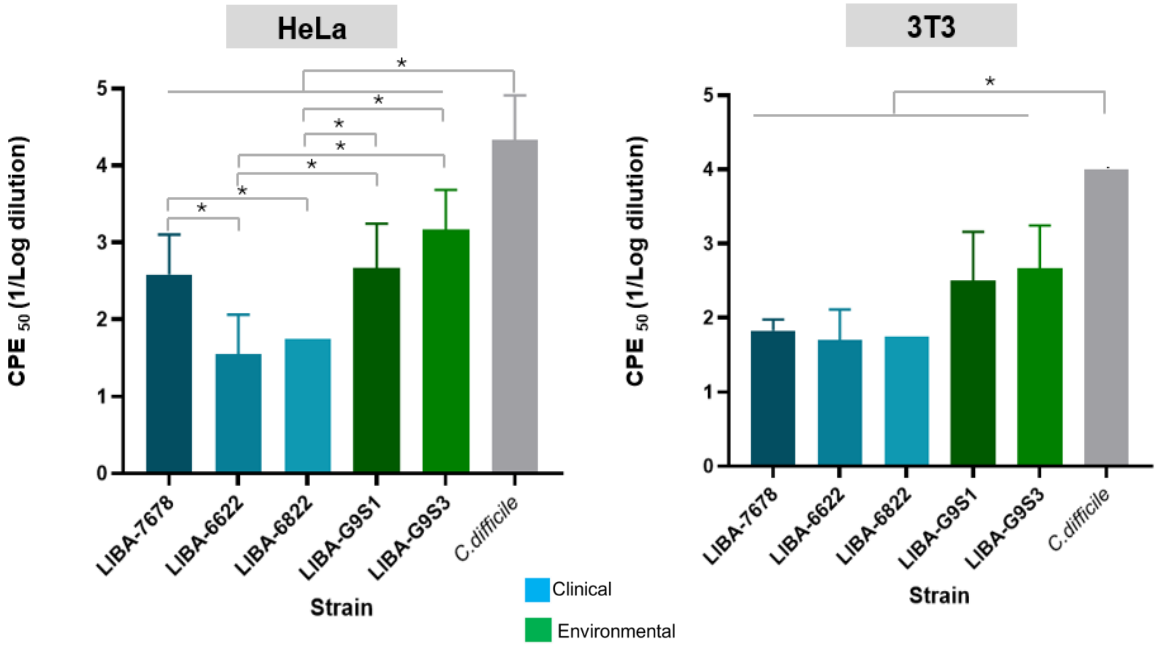

Figure 4. Toxin production of *Clostridioides* strains assessed through CPE induction. Cell-free supernatants of standardized cultures were titrated in 10-fold dilutions on 3T3 fibroblasts and HeLa cells. Twenty-four hours after incubation with the indicated supernatant, the dilution inducing a cytopathic effect for 50% of the cells (CPE_{50}) was determined by visual examination of bright-field images. Each bar represents the CPE_{50} value, and error bars indicate the coefficient of variation (CV) of the average dilution from three independent experiments. *C.difficile* R20291 was used as positive control. Statistical significance was evaluated using Kruskal–Wallis and Mann–Whitney post hoc comparisons, with significance indicated by asterisks ($p < 0.05$).

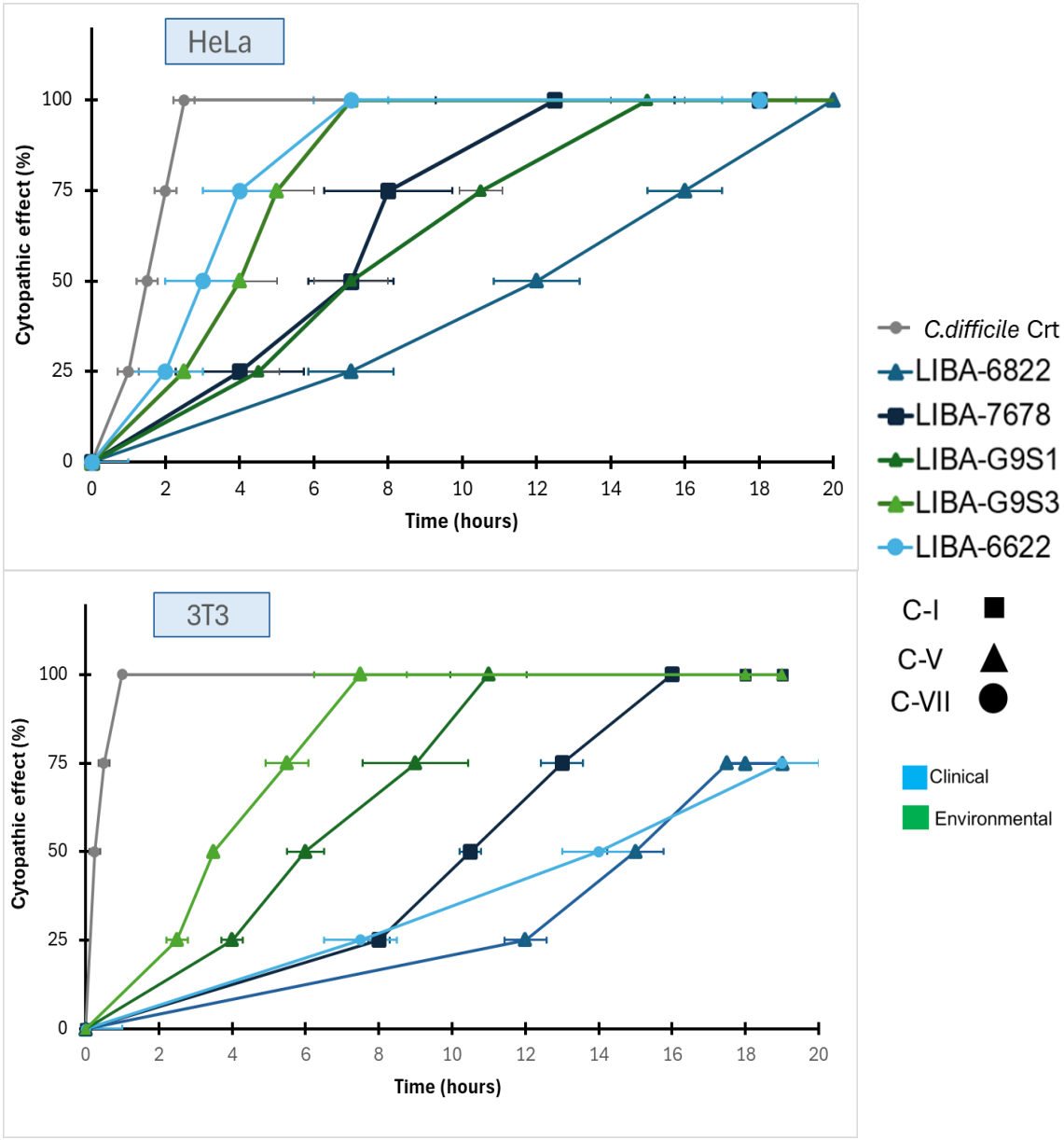

Figure 5. Kinetics of the CPE induced by cell free supernatants of Cd-like strains *in vitro*. Monolayers of HeLa (A) and 3T3 (B) cells were exposed to cell-free supernatants diluted 1:10, and the percentage (%) showing cytopathic effects (CPE) was recorded for 20 h. The percentage of rounded cells was quantified at multiple time points, and curves indicate the progression toward 25%, 50%, 75%, and 100% cell rounding. A *C. difficile* R20291 supernatant was included as a positive control. Data represent mean ± SD from three to five independent biological replicates.

Supernatants from strains LIBA-7678 (C-I), LIBA-6822, LIBA-G9S1, and LIBA-G9S3 (C-V) induced a *Paeniclostridium sordellii*–like CPE, characterized by the development of filopodia-like extensions before complete cell rounding. In contrast, intoxication with supernatants from LIBA-6622 (C-VII) resulted in a classical arborizing CPE, featuring long, branching cytoplasmic protrusions (Fig. 6(A) and Supplementary Figures 2 and 3).

Additionally, once 100% CPE was reached in cells exposed to any of the Cd-like strains, rounded cells tended to aggregate, producing a clustering phenotype. Conversely, following full cell rounding and detachment induced by *C.difficile* strain R20291, cells remained individually dispersed (Fig. 6(B) and Supplementary Figures 2 and 3).

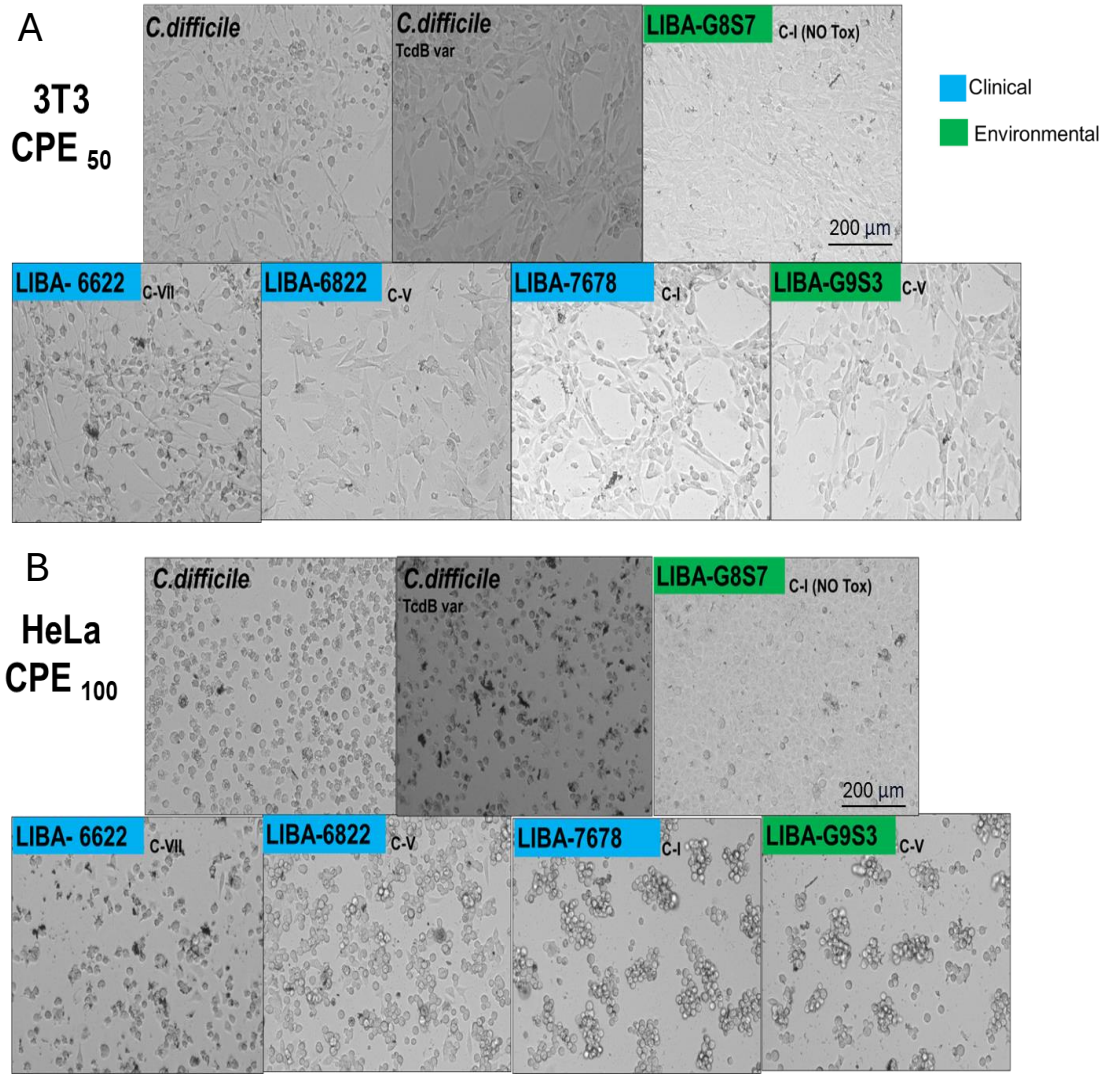

Figure 6. Characterization of cytopathic effects induced by cell-free supernatants of Cd-like strains. Representative phase-contrast images of cytopathic effects (CPE) in murine 3T3 fibroblasts at CPE $_{50}$ (A) and human HeLa epithelial cells at CPE $_{100}$ (B) after exposure to 1:10 diluted bacteria-free supernatants. *C. difficile* R20291 was included as a control for the classical arborizing CPE mediated by TcdB, whereas a TcdB-variant LIBA-5757 strain induced a filopodia-like phenotype. The non-toxigenic strain LIBA-G8S7 served as a negative control. CPE$_{50}$ and CPE$_{100}$ are shown in different cell lines to illustrate characteristic morphological changes within a single figure; complete image sets for each line are provided in Supplementary Figures 2 and 3. Scale bar = 200 µm. Representative images from three independent experiments.

Distinct TcdB substrate specificity explains the non-classical CPE induced by Cd-like strains.

Glucosylation of RhoA and Rac1 was evaluated in HeLa cells incubated with bacterial cell-free supernatants using antibodies that fail to recognize the glycosylated forms of these GTPases. In cells intoxicated with *C. difficile* R20291, RhoA was undetectable, confirming that its role as a substrate of TcdB causing classical-CPE. In contrast, supernatants from all Cd-like strains produced the same pattern as strain LIBA-5757, previously reported to carry a variant TcdB (57), indicating that RhoA was not glycosylated (Fig 7). Conversely, loss of Rac1 signal was observed in all new genomospecies, confirming that Rac1 is a target of their TcdB activity. Notably, supernatants from strain LIBA-6622 showed a weaker reduction in Rac1 signal, which could be attributed to a lower toxin concentration, consistent with its lower titers in the cytotoxicity assays. Overall, the WB results support the differential substrate specificity of TcdB variants and are consistent with the morphological changes observed during CPE induction.

Although Cdc42 glucosylation was explored, results were inconclusive (data not shown); likely due to variability among biological replicates and low signal intensity in the assay. Therefore, further optimization and targeted analyses will be required to determine whether Cdc42 represents a substrate for the TcdB subtypes produced by the Cd-like strains.

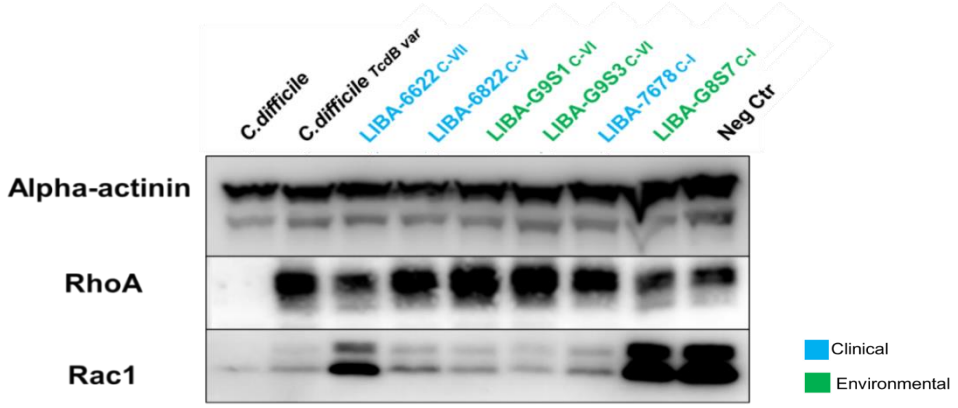

Figure 7. GTPase glycosylation induced by cell-free supernatants of Cd-like strains. HeLa cell monolayers were intoxicated with cell-free supernatants until full CPE was reached. Cells were lysed, and RhoA and Rac1 glycosylation was evaluated by Western blot using antibodies that do not recognize the glycosylated forms of these proteins. *C. difficile* R20291 and LIBA-5757 were included as controls for classical and variant TcdB cytopathic effects, respectively. Untreated cells (Neg Ctr) were used as a negative control for non-modified proteins. Membranes were probed with a monoclonal antibody against alpha-actinin as a loading control.

Acute inflammatory profiles vary across Cd-like strains, with some strains eliciting responses comparable to *C. difficile*.

The pathogenic potential of the strains was assessed by inoculating bacterial cell-free supernatants into murine ileal loops and measuring normalized ileal section weight as a proxy for edema, MPO activity as an indicator of neutrophilic degranulation, and levels of IL-1β, IL-6, and TNF-α as markers of acute inflammation. Normalization of toxin concentration was not required since all supernatants were collected at equivalent time points of the growth curve, and thus the effects also reflect differences in toxin secretion.

For most inflammatory parameters evaluated, LIBA-G9S3 induced the strongest responses, reaching levels that did not differ significantly from the virulence control *C. difficile* R20291, indicating a comparable inflammatory potential. Also, LIBA-G9S3 was the sole strain that exhibited a consistent and significant difference from the negative controls across all determinations. Edema, measured as the weight/length ratio, showed no statistically significant differences among strains (Fig 8). The cytokine profile exhibited a consistent trend: the human-associated isolates LIBA-7678 and LIBA-6622 induced lower levels of IL-1β and IL-6 (< 20 pg/mg) and TNF-α (< 5 pg/mg) than *C. difficile* R20291 (IL-1β and IL-6 > 50 pg/mg; TNF-α > 20 pg/mg). In contrast, tissues exposed to LIBA-6822 (C-V) showed cytokine concentrations similar to those induced by LIBA-G9S1 (C-V) (IL-1β and IL-6 < 40 pg/mg; TNF-α< 10 pg/mg) and markedly lower than those elicited by LIBA-G9S3 (C-V). Interestingly, although LIBA-7678 triggered minimal cytokines production (< 10 pg/mg), it induced MPO activity comparable to LIBA-6622, LIBA-6822, and LIBA-G9S1 (~2 U/100 mg). MPO levels were significantly higher in tissues exposed to *C. difficile* R20291 and LIBA-G9S3 (>2.5 U/100 mg) (ANOVA with Tukey's test, $p < 0.05$) (Fig 8).

The non-toxigenic strain LIBA-G8S7 induced mild inflammatory changes, which were comparable to those observed with the BHI control. Therefore, the effects are most likely due to the surgical procedure and tissue manipulation (Fig 8).

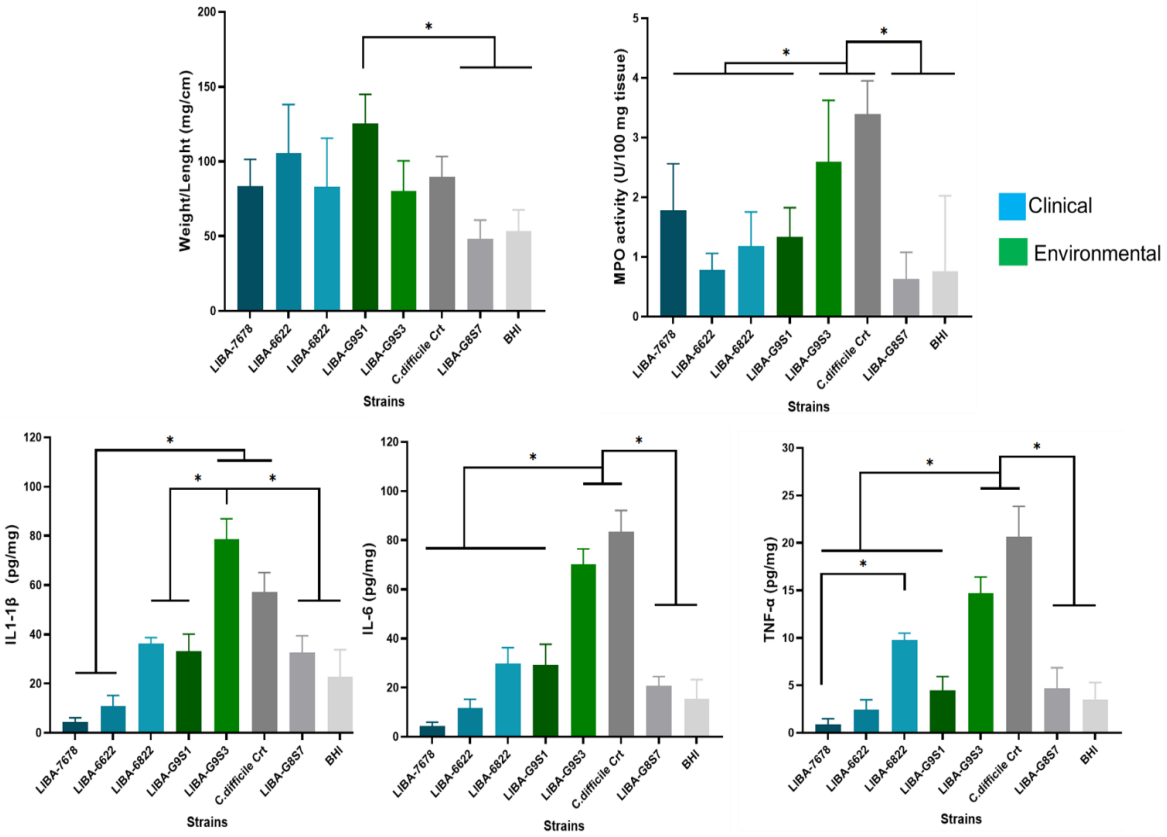

Figure 8. Effect of cell-free supernatants of Cd-like strains in the ligated murine ileal loop model. Weight-to-length ratio (mg/cm), myeloperoxidase (MPO) activity (U/100 mg tissue), and cytokine levels (IL-1β, IL-6, and TNF-α; pg/mg tissue) were quantified 4 h post-injection of cell-free supernatants from Cd-like strains, *C. difficile* control (R20291), and BHI medium control (n= 4-6). Bars represent mean ± standard error of the mean (SEM). Data are shown as mean ± SEM. (*) denotes statistically significant differences $p < 0.05$ (ANOVA with Tukey's test).

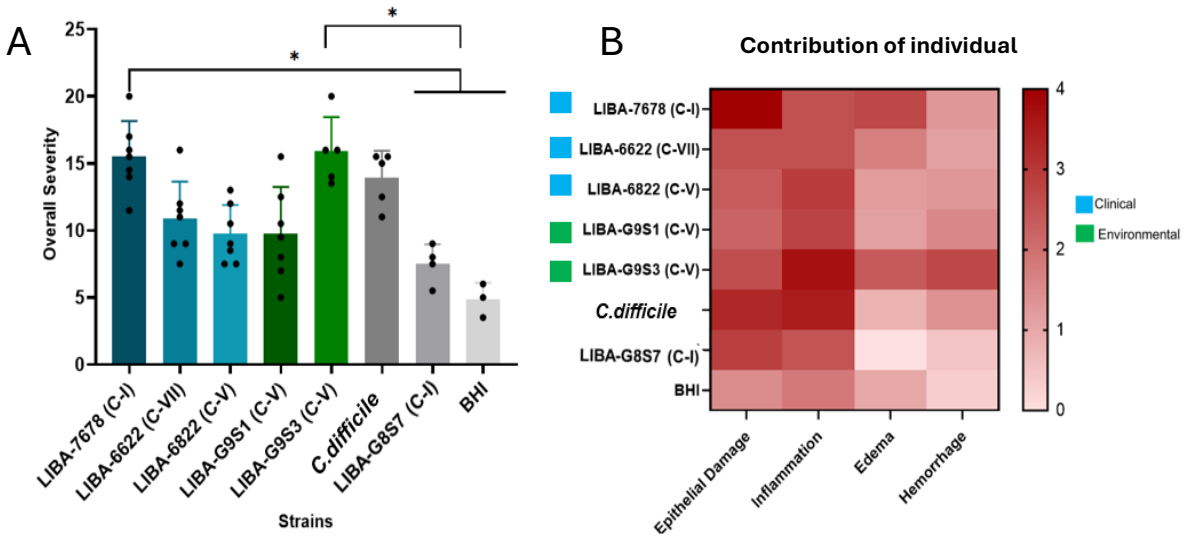

Figure 9. Histopathological scoring of intestinal damage induced by cell-free supernatants. (A) Overall severity index calculated as the sum of individual histopathological scores for epithelial damage, inflammation, edema, and hemorrhage in ligated ileal loops exposed to bacteria-free supernatants from each strain. Bars represent mean ± SEM, and individual data points correspond to biological replicates. (*p < 0.05; Kruskal-Wallis with Dunn's post-hoc test). Controls are shown in grey, *C.difficile* R20291 served as positive control, as negative controls the non-toxigenic strain LIBA-G8S7 and BHI (culture medium bacterial free) were included. **(B)** Heatmap representation of the contribution of individual histopathological parameters scores were assigned using a scale from 0 (no alteration) to 4 (severe alteration) based on the percentage and severity of the affected tissue area.

Histopathological alterations vary among Cd-like genomospecies but resemble those induced by *C. difficile*.

Histological examination of H/E-stained ileal sections revealed that a 4 h exposure to supernatants from the Cd-like strains induced measurable tissue alterations. Using a previously established pathological scoring system (40, 64, 65), severity scores were assigned for inflammation, edema, hemorrhage, and epithelial injury (Appendix 6).

Congestion and interstitial edema, typical features of acute inflammation, were evident in most tissues, with LIBA-7678 and LIBA-G9S3 showing the most pronounced submucosal expansion. However, only LIBA-7678 induced significantly greater edema compared with the non-toxigenic strain LIBA-G8S7 (Dunn's post hoc, p = 0.028) (Supplementary Fig 4). Notably, edema appeared with greater prominence in tissues exposed to the new genomospecies in comparison to those exposed to *C. difficile*, a pattern consistent with the weight/length ratios of the ileal loops (Fig 9 and 10).

Inflammation, defined as the presence of neutrophil infiltration into mucosa, submucosa, or transmural zones, was observed in all strains. LIBA-G9S3 produced significantly greater inflammation than the non-toxigenic control LIBA-G8S7 (Dunn's post hoc, p = 0.041) (Supplementary Fig 4).

While sporadic red blood cell extravasation was observed under most conditions, hemorrhage was more pronounced in the submucosa of tissues exposed to strain LIBA-G9S3 (Fig. 10). However, when hemorrhage was evaluated by comparing the mean severity scores assigned, no statistically significant differences were detected among strains (Kruskal–Wallis, p = 0.180) (Supplementary Fig 4).

Epithelial alterations were also observed across all Cd-like strains, with LIBA-7678 exhibiting a significantly higher mean severity score than the non-toxigenic control (Kruskal–Wallis, p = 0.002, Dunn's post hoc, p = 0.009) (Supplementary Fig 4). In contrast to control tissues, which display organized villi and well-defined crypt architecture, villi disorganization, rupture, and the appearance of Gruenhagen's space were observed in tissues exposed to supernatants from Cd-like strains. LIBA-7678 and LIBA-6622 were associated with evident alterations of the villous structure, including villus blunting, broadening, and, in severe cases complete villous atrophy (Fig. 9 & 10). Changes in crypt architecture, including distortion and loss of structural definition, were observed in tissues exposed to LIBA-7678, LIBA-6622, and LIBA-G9S3. Ulcerations and epithelial erosions were also observed in tissues treated with supernatants from LIBA-7678 and LIBA-G9S3. In contrast, exposure to *C. difficile* supernatants resulted in extensive epithelial desquamation, a feature not observed in tissues exposed to the Cd-like strains. Goblet cell loss and hyperplasia were not evident in the histopathological evaluation (Fig. 10).

To integrate the individual histopathological parameters into a single, comparative measure, an overall severity score was calculated for each animal. This score was obtained by summing the values obtained for inflammation, edema, hemorrhage, and epithelial injury. This composite metric revealed that all Cd-like strains induced histological alterations phenotypically comparable to those caused by *C. difficile* R20291 (Fig. 9). Among the strains evaluated, only LIBA-7678 (C-I) and LIBA-G9S3 (C-V) displayed overall severity scores that were significantly higher than those of the negative controls (LIBA-G8S7 and BHI)

(Kruskal-Wallis with Dunn's post-hoc test $p < 0.05$). This finding confirms their capacity to induce pronounced tissue injury. There were no significant differences between the remaining genomospecies and *C. difficile*, which further supports the hypothesis that these divergent lineages have the potential to cause substantial inflammatory and structural damage to the ileal mucosa.

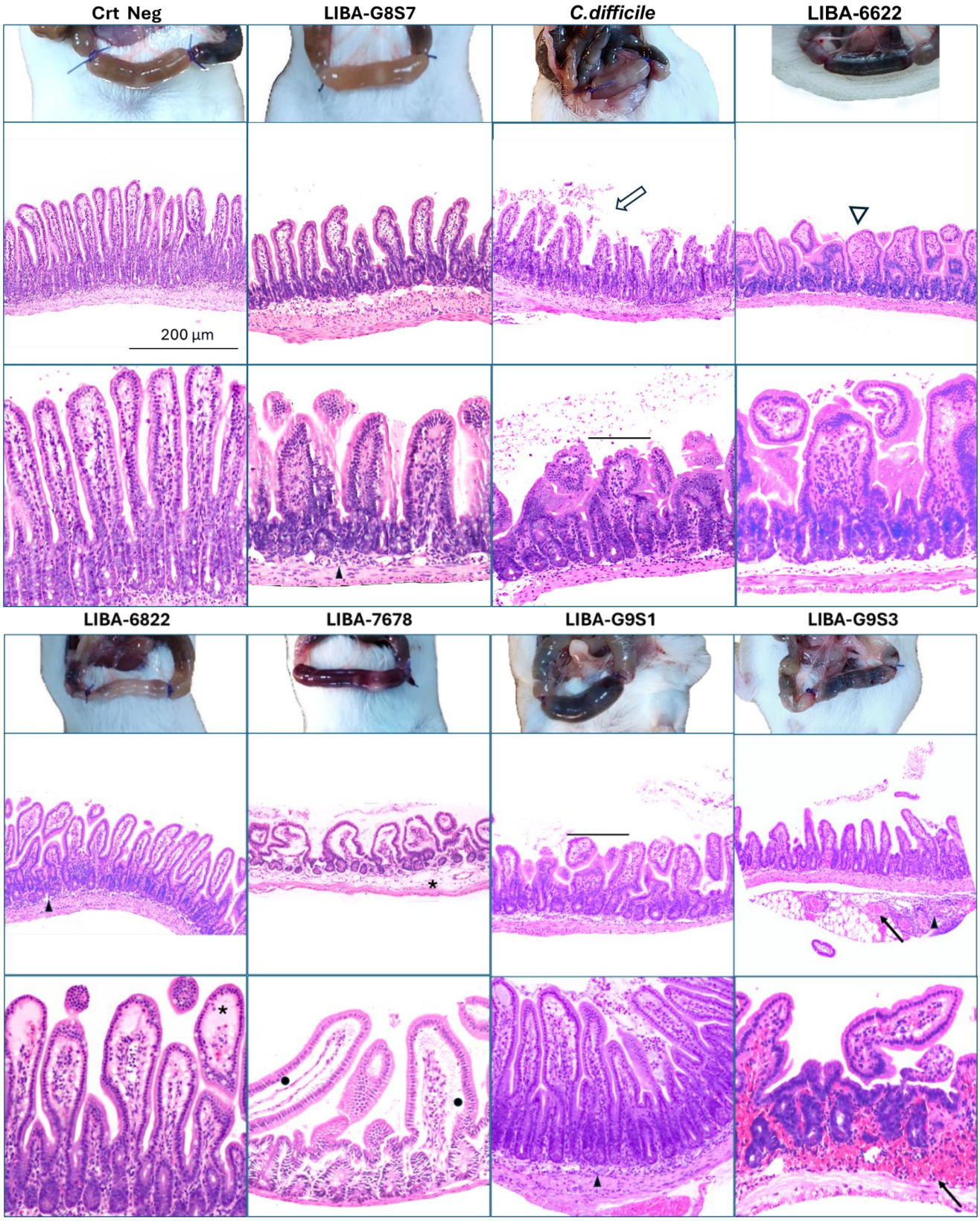
Crt Neg
LIBA-G8S7
C.difficile
LIBA-6622
200 µm
LIBA-6822
LIBA-7678
LIBA-G9S1
LIBA-G9S3

Figure 10. Histopathological evaluation of intestinal damage in the murine ligated ileal loop model. Representative macroscopic images and hematoxylin–eosin (H&E) stained sections of ileal loops collected 4 h after inoculation with bacteria-free supernatants from each strain (n = 4–6 mice per group). A sterile saline solution (negative control) showed normal villus architecture, whereas *C. difficile* R20291 was included as a reference for toxin-mediated epithelial damage and the non-toxigenic strain LIBA-G8S7 as a negative control. Key pathological alterations are indicated: inflammatory cell infiltration (arrowheads), edema (asterisks), Gruenhagen's space formation (dots), villus blunting (open arrowheads), villus atrophy (horizontal bars), hemorrhage (solid arrows), and epithelial desquamation or erosion (open arrows). Scale bar: 200 μm.

Germination patterns and toxin secretion show strain-dependent variability rather than origin-specific differences

To investigate whether spore germination rates differ according to the source of isolation, germination efficiency was compared between clinical and environmental strains. Although environmental isolates showed the highest germination rates, these differences were not statistically significant (Kruskal–Wallis, $p = 0.387$) (Fig 11). This observation is of particular interest since the germinant used in these assays (1% taurocholate) represents the main bile salt derivative involved in triggering germination during intestinal infection (12).

A similar analysis was performed to assess toxin production according to strain origin. Cytopathic titers (CPE_{50}), expressed as 1/log of the highest dilution inducing 50% cell rounding after 24 h, were compared between clinical and environmental strains. Under this representation, higher CPE_{50} values indicate greater cytopathic activity and, consequently, higher levels of toxin production. All Cd-like strains exhibited lower TcdB titers than the *C. difficile* reference strain R20291. Among the Cd-like strains, environmental isolates displayed slightly higher toxin titers than clinical isolates; however, this difference was not statistically significant (Kruskal-Wallis with Dunn's post hoc, $p = 0.150$) (Fig. 11.)

Taken together, the absence of significant differences in both germination and toxin production between clinical and environmental isolates indicates that the variability observed in these phenotypes is strain-dependent rather than origin-specific.

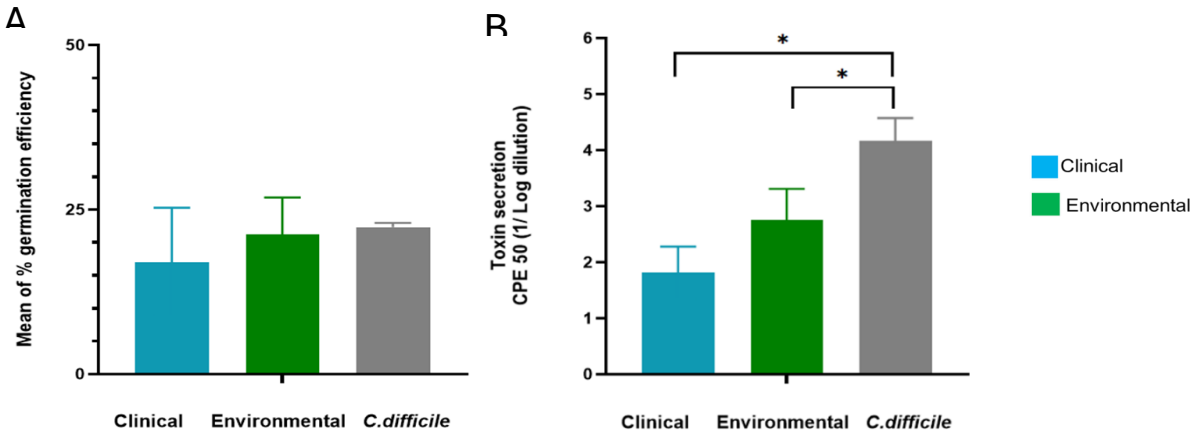

Figure 11. Comparison of toxin secretion and germination efficiency between clinical and environmental *Clostridioides* isolates. (A) Mean spore germination efficiency in the presence of 1% taurocholate. *C. difficile* R20291 was included for reference. **(B)** Toxin concentration reported as 1/log of the highest dilution required to induce CPE_{50} after 24 h, were compared among groups based on the origin of the isolates. Environmental isolates exhibited the highest germination rates and toxin titers though not reaching statistical significance differing from clinical strains. Data are shown as mean ± SEM. * ($p < 0.05$).

Environmental isolates of Cd-like strains induced *C. difficile*-like inflammatory patterns, whereas clinical isolates show attenuated responses.

The ileal loop model was used to evaluate multiple quantitative parameters, which were subsequently grouped according to strain origin to identify patterns of inflammatory responses. Data standardization allowed all variables to be compared on the same scale, and principal components were selected to account for 75% of the total variance. A PCA biplot (Supplementary Fig. 5) showed that all cytokine measurements were closely related and contributed with similar magnitude to the variance. Clinical strains, together with the non-toxigenic LIBA-G8S7, clustered separately and were associated with the lowest inflammatory responses, whereas environmental strains grouped with the *C. difficile* control, reflecting stronger and comparable pro-inflammatory profiles (Fig. 12). These quantitative results were consistent with the histological findings, which also revealed differences between clinical and environmental strains.

All strains induced inflammation in the ileal tissue; however, clinical strains were associated with milder alterations compared to both environmental strains and the *C. difficile* control (Fig. 12B). Edema was more pronounced in the new genomospecies strains than in *C. difficile*

R20291, whereas hemorrhage was particularly evident in tissues exposed to environmental strains.

The quantitative inflammatory markers were consistent with the histopathological observations. Environmental strains showed inflammatory profiles comparable to *C. difficile*, demonstrating superior inflammatory potential relative to clinical isolates. This was evidenced by significantly higher cytokine levels—particularly IL-1β (Kruskal–Wallis with Dunn's post hoc p=0.025) and IL-6 (Kruskal–Wallis with Dunn's post hoc p=0.025) which were markedly higher than those observed in clinical isolates. In contrast, clinical strains induced significantly lower cytokine concentrations and reduced MPO activity, indicating a milder inflammatory response (Table 2). Together, these quantitative trends confirm that environmental isolates elicit a pro-inflammatory phenotype closely resembling that of *C. difficile*, whereas clinical isolates induce weaker responses.

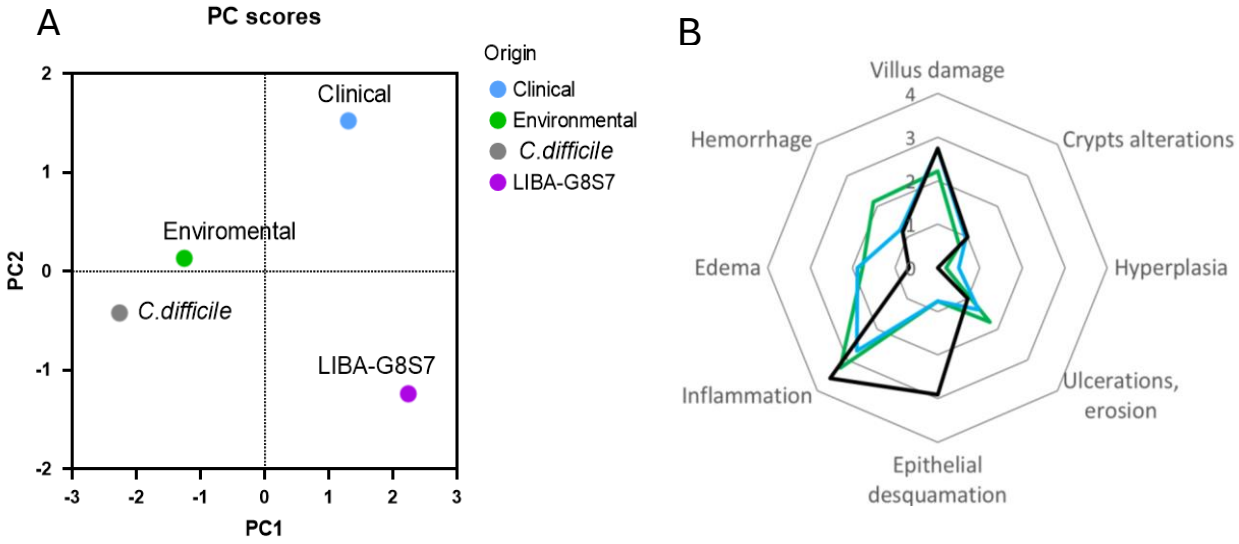

Figure 12. Principal component analysis of quantitative and histological markers of intestinal injury in the murine ileal loop model.. (A) Principal component analysis (PCA) of quantitative pathological markers (weight/length ratio, MPO activity, cytokine concentrations, and overall histopathological severity). Data points are grouped according to the origin of the isolates: clinical, environmental, *C. difficile*, and the non-toxigenic Cd-like strain LIBA-G8S7. PC1 and PC2 account for the highest proportion of variance (PC1 explains 75% and PC2 23% of total variance), revealing distinct clustering patterns among groups. (B) Radar plot depicting the mean contribution of individual histopathological parameters—to intestinal injury in each strain origin group.

Table 2. Comparison of inflammatory markers in the murine ileal loop model induced by Cd-like strains according to strain origin.

Inflammatory markers	Origin		
	Clinical	**Environmental**	*C.difficile*
Weight/Lenght ($^{mg}/_{cm}$)	89,23 ± 7,06	107,13 ± 9,48	89,55 ± 6,88
MPO ($^{U}/_{100\ mg}$)	1,2 ± 0,1 *	1,94 ± 0,30	3,39 ± 0,32
TNF-α ($^{pg}/_{mg}$)	4,38 ± 1,0 *	9,61 ± 2,27	20,66 ± 3,57
IL-1β ($^{pg}/_{mg}$)	**14,58 ± 3,69 ***	**49,68 ± 9,60**	83,34 ± 9,78
IL-6 ($^{pg}/_{mg}$)	**16,36 ± 3,92 ***	**53,4 ± 9,75**	57,06 ± 9,24

Values represent mean ± SEM of grouped clinical or environmental isolates and *C.difficile* R20291. Statistical comparisons were performed using the Kruskal–Wallis test followed by Dunn's post hoc method ($p < 0.05$). Values in **bold** indicate significant differences between clinical and environmental strain categories. Values marked with * indicate significant differences compared with *C. difficile* R20291.

1.4 Discussion

This study demonstrates that some of the Cd-like strains may possess a pathogenic potential comparable to *C. difficile*, supporting the central hypothesis that these lineages exhibit distinct yet functionally relevant virulence traits. Despite their marked genomic divergence—particularly within toxin-associated loci—their pathogenic mechanisms remain largely driven by TcdB, which was consistently observed across *in vitro* and *in vivo* assays. Notably, strains of environmental origin displayed stronger inflammatory and tissue-damaging capacities than clinical isolates, revealing an unexpected ecological trend in virulence expression. Together, these results highlight that genomic divergence among these *Clostridioides* species translates into meaningful phenotypic variability, which may influence their capacity to colonize hosts, cause disease, or persist in environmental reservoirs. These conclusions arise from an integrated evaluation of key pathogenic processes, including spore germination, toxin activity, and epithelial injury.

Spore germination represents a crucial step in *Clostridioides* pathogenesis, as it marks the transition from dormant spores to vegetative cells capable of colonization and toxin production (58). In the context of physiological conditions, this process is facilitated by bile salts and co-germinants such as glycine and calcium. In this study, strain-specific variations in germination kinetics were observed when TA was used as the primary germinant,

suggesting differences in receptor affinity or the activity of spore-associated enzymes among Cd-like strains. Importantly, heterogeneity in germination responses to bile salt germinants and inhibitors has also been reported across a wide range of *C. difficile* ribotypes, indicating that substantial intra-species variability in germination behavior is well documented (33)**.** Remarkably, two environmental strains exhibited higher germination efficiencies than both clinical isolates and the reference *C. difficile* strain R20291. This observation raises questions regarding their ability to recognize host-derived bile salts and other host-associated metabolites, as well as their potential to germinate and colonize the mammalian gastrointestinal tract. Such behavior is noteworthy, given that environmental strains would not be expected to be adapted to these host-associated signals, whereas clinical isolates were anticipated to show greater responsiveness. Moreover, the high germination efficiencies observed are especially relevant, as enhanced germinative capacity in *C. difficile* has been previously linked to an increased risk of recurrent CDI and greater clinical severity (66, 67). These strain-specific patterns suggest that the Cd-like strains may differ in key components of their germination and sporulation pathways. It would be of interest to examine additional physiological factors, such as phosphate, potassium, pH, amino acids, and secondary bile acids, as these may influence strain-specific germination efficiency and disease severity (58, 68). Cortex hydrolysis alone may be insufficient for ensuring complete germination (69). Therefore, assessing colony-forming efficiency under host-like conditions could provide a more comprehensive view of their pathogenic potential.

Following germination in the ileum, *C. difficile* vegetative cells produce the major toxins TcdA and TcdB, whose levels are generally correlated with disease severity (70). Toxin synthesis is modulated by environmental and nutritional factors, being repressed by readily metabolizable carbon sources and amino acids, however, they are stimulated through quorum-sensing signals (71). *In vitro,* toxin production occurs predominantly during the stationary growth phase (72), which supports the use of standardized stationary cultures, normalized by CFU/mL, to measure toxin titers in cell-free supernatant. The Cd-like strains displayed variable toxin titers; however, despite sequence divergence in the regulatory genes *tcdR* and *cdtR* among clades C-I and C-V strains LIBA-6822, LIBA-7678, LIBA-G9S1, and LIBA-G9S3 (24), none exhibited higher TcdB concentrations than *C. difficile* R20291. These differences likely reflect strain-specific variation in transcriptional regulation, secretion

efficiency, or toxin stability (46, 73), rather than enhanced toxin synthesis. Evaluating toxin expression *in vivo*, where nutrient availability, microbiota interactions, and host signals differ significantly from laboratory settings. This evaluation will be critical to determine whether these regulatory differences translate into distinct toxin outputs during infection**.** Future studies using targeted transcriptomic analyses of toxin and regulatory genes, construction of regulatory mutants, and functional assays with purified recombinant toxins will be essential to dissect the specific contributions of regulatory circuitry and toxin activity to the observed phenotypes (74).

When toxin levels were analyzed by isolation source, environmental isolates tended to produce higher TcdB titers than clinical strains, although the differences were not statistically significant. This trend may reflect metabolic or ecological adaptations linked to their native environments, whether soil- or host-associated. However, the precise determinants of toxin output remain to be elucidated. Nonetheless, toxin quantity alone does not determine virulence (75), as cellular damage also depends on toxin activity. Therefore, the kinetics and morphology of the cytopathic effect (CPE), along with associated glycosylation patterns, were further examined.

CPE kinetics are influenced both by the catalytic properties of distinct TcdB variants and by the receptor repertoire of the target cell. HeLa and murine fibroblasts (3T3) express FZD2/7, CSPG4, PVRL3, and LRP1, but differ in receptor abundance: 3T3 cells show elevated CSPG4 levels, whereas HeLa cells exhibit reduced PVRL3 and LRP1 expression (76, 77), which may account for cell line–specific responses. Receptor specificity may further shape CPE by directing internalization routes, enabling simultaneous receptor interactions, and modulating translocation dynamics to the cytosol (78, 79). Toxin concentration also influences binding efficiency, as CSPG4 and FZDs mediate entry at low levels, whereas PVRL3 contributes only at high concentrations (63). This could explain the faster CPE observed with the reference strain R20291, which exhibited higher titers than the Cd-like strains. Given the diversity of TcdB sequences across clades, as well as the differences observed among strains within the same clade, it is also plausible that additional, yet unidentified, receptors contribute to the responses observed for the new isolates.

Subtyping provides a molecular framework for interpreting how sequence variations affect toxin function and antigenicity (18). Different TcdB subtypes exhibit divergent receptor-binding preferences, thereby modulating host cell targeting. For example, TcdB4 displays a marked preference for TFPI, whereas TcdB2 also binds CSPG4. In addition, several subtypes associated with cryptic clades (TcdB7, TcdB10, TcdB11, TcdB12) primarily rely on CSPG4 or TFPI rather than FZD receptors (80, 81). Notably, receptor usage exhibit variability even within a specific subtype. A noteworthy example of this the TcdB2 variants, which demonstrate an alternating pattern between TFPI and FZD binding, or closely related TcdB7 toxins that differ in receptor preference despite >98% sequence identity (43, 81). This plasticity suggests the existence of selective pressures that favor receptor-binding shifts across different lineages. In this context, the reference strain R20291 expresses TcdB2, whereas the new genomospecies carry TcdB7 toxins—except LIBA-6622, which encodes TcdB11—highlighting that subtype-specific receptor affinities may underlie part of the strain-dependent differences observed in CPE kinetics.

Based on GTD sequence comparisons, two major groups have been proposed among subtypes: one including B3, B4, B7, and B8, which typically induce CPE resembling the phenotype of TcsL (45), and another comprising the remaining subtypes, which generate cell rounding with multiple protrusions (arborizing effect) (18). Our results support this model, as glycosylation patterns were consistent with the observed CPE. Previous studies have demonstrated that differential glycosylation of the small GTPase Rac1 is directly associated with the variant cytopathic effect (45, 57). In agreement with this observations, the strain LIBA-5757, as previously described, exhibited Rac1 glycosylation patterns consistent with this variant phenotype, further supporting the mechanistic link between GTD substrate specificity, Rac1 modification, and the resulting cytopathic outcome (57).

Notably, when 100% CPE was reached by the Cd-like strains, an additional clustering of affected cells was observed (Fig.6 & Supplementary Figure 2 and 3). This phenotype differs from the classical TcdB-induced cytopathic effect, in which rounded cells typically remain individually dispersed following detachment (57). The mechanisms underlying this clustering remain to be determined. One possible explanation is the contribution of the binary toxin CDT, which is present in most Cd-like strains. CDT has been shown to induce actin-

dependent membrane protrusions and cytoskeletal rearrangements (49), which could promote increased cell–cell contacts or adhesion, thereby favoring cellular aggregation under conditions of extensive cytopathic damage. However, further studies will be required to directly assess the role of CDT in this phenotype and to disentangle its contribution from that of TcdB variants.

The observed CPE is largely reflective of TcdB-mediated disruption of the actin cytoskeleton and focal adhesions, which promotes cell rounding, loss of tight junction integrity, and impaired cellular functions (15, 57), yet the toxin also induces a wide range of cellular alterations that may exacerbate disease severity (19, 82). The toxins, compromise epithelial regeneration by impairing colonic stem cell function and renewal, and can trigger cellular senescence (42, 83, 84). Together, these effects underscore the importance of re-evaluating the biological activity of the new genomospecies under physiologically relevant conditions.

A comparative assessment of supernatants from the Cd-like strains in the mouse ileal loop model provided insights into the contribution of toxins and other secreted factors to epithelial damage and inflammation. Although *in vitro* toxin titers of these strains did not reach the levels observed for *C. difficile* R20291, they nonetheless induced alterations consistent with CDI pathology (40). The soil isolates LIBA-G9S1 and LIBA-G9S3 elicited elevated cytokine secretion in accordance with their toxin titers, whereas the clinical strains LIBA-7678 and LIBA-6822 caused marked epithelial injury and inflammation despite lower toxin concentrations. Similar findings have been reported for strains with low toxin production *in vitro* but comparable lethality *in vivo* (85).

The absence of a strict correlation between toxin titers and tissue damage highlights that pathogenesis results from complex interactions involving toxin potency, additional bacterial factors, and host immune responses (75). In the present study, *in vitro* assays did not reveal significant differences according to strain origin, whereas multivariate analysis of *in vivo* data clearly separated environmental strains from clinical isolates, with the former exhibiting tissue damage and inflammatory profiles comparable to those induced by *C. difficile.* This discrepancy may be partly explained by methodological limitations inherent to *in vitro* assays, which rely exclusively on toxin concentrations measured in cell-free supernatants and do not capture host-related factors. In contrast, *in vivo* models integrate additional factors,

including receptor availability and distribution, tissue architecture, the presence of accessory virulence factors, and immune-mediated amplification of damage. Therefore, toxin concentration alone may be insufficient to predict virulence, and *in vivo* models provide a more integrative assessment of pathogenic potential, revealing differences that may not be apparent in simplified *in vitro* systems.

In most tissue samples in which toxin-like-mediated alterations were evident, the lesions appeared in sporadic patches, with areas of intact mucosa still preserved. It is noteworthly that previous studies using *C. difficile* in murine ileal loop models frequently employed elevated inoculation volumes of cell-free supernatants (40), which could explain differences in the extent of tissue injury and underscore the necesity for standardizing conditions when assessing pathogenic severity. Overall, the histopathological alterations induced by the Cd-like strains were consistent with those previously described for *C. difficile* infection in both animal models and human cases (52, 64, 86). These findings reinforce the pathogenic potential of the newly described *Clostridioides* genomospecies.

Cytokines increases were also consistent with the immune response described in CDI, where TNF-α serves as an early marker of pathogenesis, IL-6 promotes neutrophil influx and amplifies epithelial injury through NOD- and NFκB-dependent pathways, and IL-1β is strongly linked to toxin-induced responses (15, 87). MPO activity paralleled cytokine secretion, being highest for LIBA-G9S3 and LIBA-7678, although PMN infiltration was consistently abundant in all strains. This suggests that MPO more accurately reflects the activation status of recruited neutrophils rather than their absolute presence, emphasizing that excessive neutrophil activation drives epithelial damage and worsens disease severity (48, 61, 88).

Histological analyses showed abundant inflammatory infiltration in all isolates, whereas cytokine levels were higher in some strains such as LIBA-G9S3. This apparent dissociation may indicate the involvement of additional immune recruitment pathways beyond IL-6- and IL-1β-driven responses. Other inflammatory mediators previously implicated in TcdA- and TcdB-induced inflammation, including monocyte chemoattractant protein-1 (MCP-1), IL-23, or inflammasome activation and release of cytokines such as IFN-γ could contribute to leukocyte recruitment and activation (42).

Beyond inflammatory infiltration, additional histopathological alterations were evident, with some strains inducing more pronounced villus architectural changes, whereas others were characterized predominantly by submucosal edema or epithelial disruption. The presence of edema and fluid accumulation, reflected in the increased weight-to-length ratio of the loops, is consistent with the intestinal permeability changes and fluid secretion previously described for *C. difficile* toxins (64, 89). Notably, marked submucosal edema typical of early CDI was observed (64), although more advanced lesions such as pseudomembrane formation and extensive epithelial necrosis were not evident. Structural alterations of the epithelium are particularly relevant, as they may facilitate spore adherence and contribute to recurrence (90).

While *C. difficile* infection predominantly affects the colon and cecum, ileal loop models are restricted to the small intestine, and thus results must be interpreted with caution (91). The effects of purified TcdB in rodent ileal loops are comparatively mild, in contrast to the pronounced enterotoxicity of TcdA. This discrepancy can be attributed to the abundance of TcdA receptors present in the ileum as well as the preferential distribution of TcdB receptors in the colon and cecum (48, 91). This receptor distribution may also explain the stronger epithelial damage observed with *C.difficile* strain R20291, whose supernatant is expected to contain active TcdA, and more severe alterations would likely be anticipated in models assessing colonic tissue for new genomospecies. Moreover, TcdB preferentially binds to the basal surface of epithelial cells, implying that barrier disruption by additional factors facilitates receptor access and subsequent inflammatory effects (44). These considerations support the use of complete bacterial supernatants in the present model, as they enable the assessment of how additional virulence factors, including CDT, may promote epithelial permeability and thereby enhance TcdB-mediated pathology.

The comparatively lower cytokine levels observed in this study may be indicative of variability in inflammatory responses influenced by experimental design—such as the use of bacterial supernatants instead of purified toxins—as well as intrinsic differences in animal model characteristics (e.g., age, sex, diet, or genetic background), toxin variants, and exposure conditions including dosage and timing (48, 68, 92). Variability could also arise from the ileal loop's lack of direct host–pathogen interaction, which distinguishes it from infection-based CDI models (93).

As anticipated, environmental and clinical isolates induced distinct tissue alterations. The environmental strains LIBA-G9S1 and LIBA-G9S3 elicited stronger inflammation and hemorrhage, suggesting different virulence strategies. Clinical isolates may reflect adaptation to mammalian hosts, shaped by immune selection and antibiotic pressure (73), whereas environmental strains evolve under distinct constraints that favor metabolic versatility and the production of uncharacterized secreted factors with potential virulence roles. These differences highlight how ecological context may drive the diversification of virulence mechanisms across *Clostridioides* species.

Although no formal phylogenetic comparison was performed and the number of isolates analyzed per genomospecies was limited, the data nonetheless indicate notable variability within each genomospecies. For instance, the C-V strains LIBA-6822, LIBA-G9S1, and LIBA-G9S3 showed markedly different inflammatory and tissue-damage profiles, despite belonging to the same clade. Similarly, the C-I representative LIBA-G8S7 was non-toxigenic and displayed an atypical germination pattern, further illustrating intra-clade diversity. In addition, the C-VII genomospecies demonstrated reduced toxin production and decreased pathogenicity relative to the other groups. These observation suggest that phylogenetic grouping alone does not fully predict pathogenic behavior, and that ecological origin and strain-specific factors may also contribute to phenotypic outcomes. A more comprehensive phylogenetic assessment will require incorporating larger numbers of clinical and environmental isolates from each genomospecies, enabling clearer resolution of clade-associated pathogenic signatures.

Collectively, these findings provide experimental evidence in support of the central hypothesis that divergent *Clostridioides* lineages circulating in human and environmental sources in Costa Rica possess pathogenic traits comparable, at least in part, to those of *C. difficile*. Their functional characterization of toxin activity broadens our understanding of the mechanisms underlying virulence in emerging *Clostridioides.* Beyond confirming their pathogenic potential, this work highlights the dynamic interplay between host, pathogen, and environment, emphasizing that virulence is not an exclusive feature of clinical isolates. These results underscore the importance of a One Health perspective, as environmental reservoirs

may harbor strains capable of causing disease, influencing transmission dynamics, and contributing to the emergence of un characterized pathogenic lineages.

CHAPTER 2.

Previously undescribed species related to *Clostridium perfringens*

2.1 State of the Art

2.1.1 *Clostridium perfringens*

Clostridium perfringens is a Gram-positive, spore-forming, anaerobic bacterium widely distributed in nature and commonly isolated from soil, water, food, and the intestinal microbiota of humans and animals. The persistence and dissemination of *C. perfringens* across diverse ecological niches are facilitated by its highly resistant spores, which can support external conditions such as heat, desiccation, nutrient limitation, and oxygen exposure. The species exhibits remarkable metabolic versatility and rapid growth, enabling it to proliferate efficiently in nutrient-rich environments (13, 94). Genomic features underscore the exceptional adaptability, heterogeneity, and pathogenic versatility of *C. perfringens*, reinforcing its relevance from a One Health perspective (3).

2.1.2 Genomic diversity in *C. perfringens*.

C. perfringens exhibits one of the most diverse and open pangenomes among Gram-positive bacteria (14). The broad ecological distribution of this species has driven diversification into five stable phylogroups (I–V) with variable virulence profiles and environmental adaptations (26). Its low GC content and rapid replication promote remarkable genomic plasticity and lateral gene transfer, enabling the rapid acquisition of exogenous genes. Plasmids and other mobile genetic elements play a key role in disseminating toxin genes and antimicrobial resistance determinants, while prophages and the frequent absence of CRISPR systems further enhance genetic exchange (14, 95). The genetic context of toxin genes critically influences virulence evolution: plasmid-encoded toxins can spread horizontally to non-virulent strains, generating novel pathogenic variants, whereas chromosomal toxin genes may undergo loss, attenuation, or diversification through mutation (16).

C. perfringens is linked to a wide range of systemic and enteric diseases in livestock and humans, including gas gangrene, food poisoning, non-foodborne diarrhea, and enterocolitis (14, 16). The virulence of *C. perfringens* is primarily associated with its ability to produce a wide array of extracellular toxins and enzymes. More than twenty degradative toxins have been described, including phospholipases, proteases, collagenases, hyaluronidases,

hemolysins, and neuraminidases, which collectively contribute to extensive tissue damage during infection. Based on the presence of six major toxins—alpha (CPA), beta (CPB), epsilon (ETX), iota (ITX), enterotoxin (CPE), and necrotic enteritis B-like toxin (NetB)—*C. perfringens* strains are currently classified into seven toxinotypes (A–G), each associated with specific diseases (96)(Table 3).

Table 3. Main toxins produced by *C. perfringens* and their locations (Taken from (13))

Toxins	Toxin Types	Encoded Genes	Gene Location	Protein Size, kDa
Alpha (CPA or PLC)	A, B, C, D, E, F, G	*cpa* or *plc*	Chromosome	42.5
Beta (CPB)	B, C	*cpb*	Plasmid	35
Epsilon (ETX)	B, D	*etx*	Plasmid	34
Iota (ITX)	E	*iab* and *iap*	Plasmid	Ia: 47.5, Ib: 71.5
Enterotoxin (CPE)	C, D, E, F	*cpe*	Chromosome or Plasmid	35.5
Enteritis B-like toxin (NetB)	G	*net*B	Plasmid	28

Comparative genomic analyses have shown that toxinotype A does not represent a phylogenetically distinct lineage within *C. perfringens* (Fig.13)(10, 97). Instead, toxinotype A is defined by the absence of the plasmid-encoded major typing toxins found in other toxinotypes, leaving the chromosomal *cpa* gene—located near the origin of replication and encoding α-toxin (PLC)—as its principal virulence determinant (10).

2.1.3 Gas gangrene

Clinical features, pathogenesis, and treatment

Gas gangrene, or clostridial myonecrosis, is a rapidly progressing and highly lethal necrotizing infection of skeletal muscle and subcutaneous tissue. *C. perfringens* toxin type A accounts for approximately 80–90% of traumatic cases in both humans and animals. The disease is characterized by extensive myonecrosis, gas accumulation, toxemia, and systemic complications such as sepsis, renal failure, and multiorgan dysfunction (13, 14).

Diagnosis primarily relies on clinical evaluation supported by microbiological and imaging evidence; however, conventional culture-based methods have limited sensitivity for detecting *C. perfringens* due to its fastidious growth and rapid tissue degradation. Prompt treatment is critical and typically involves urgent surgical debridement, high-dose intravenous antibiotics, fluid resuscitation, and adjuvant hyperbaric oxygen therapy to enhance tissue oxygenation and restrict anaerobic proliferation (98).

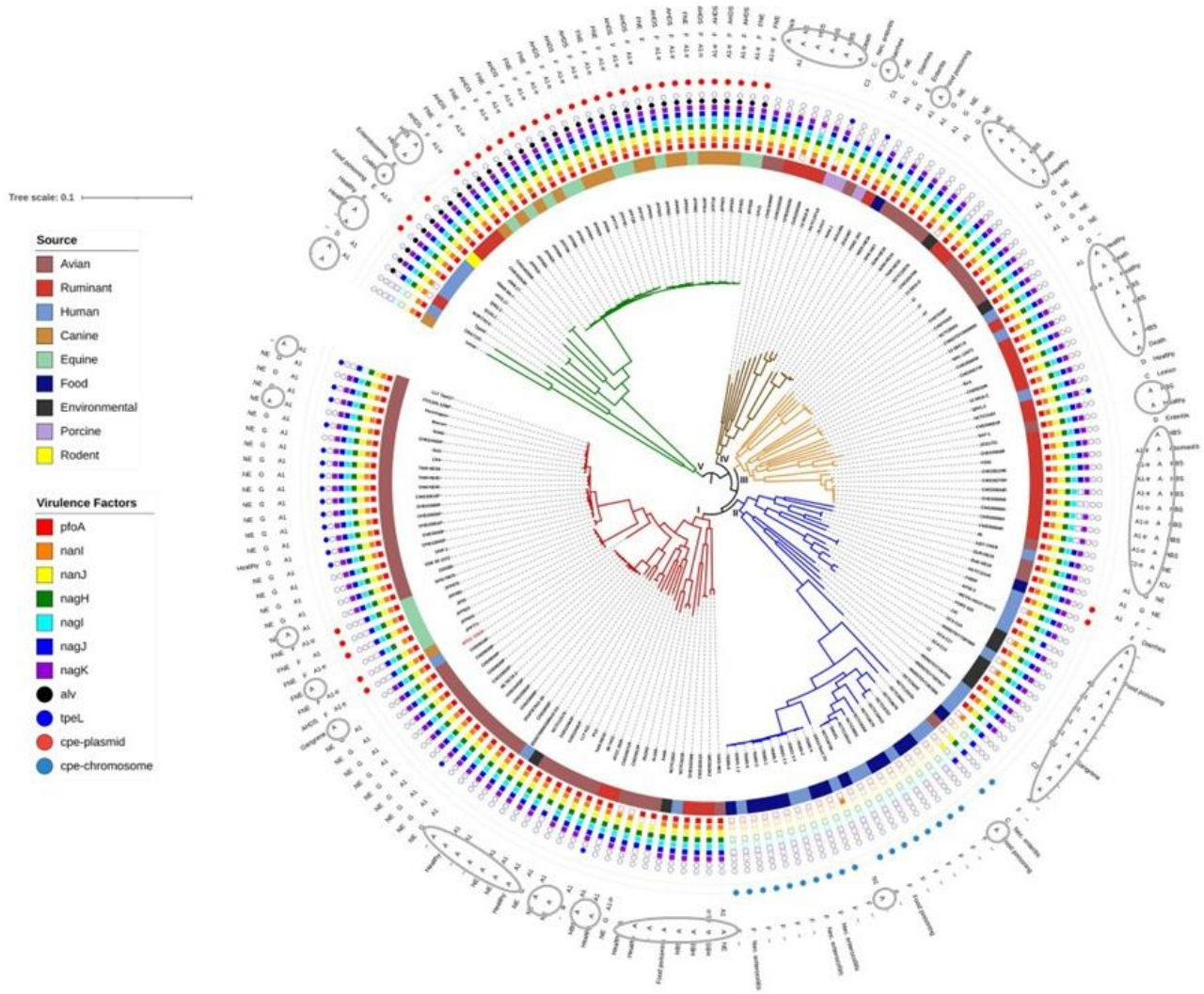

Figure 13. Phylogenetic diversity among *Clostridium perfringens*. Maximum-likelihood phylogenetic tree of C. perfringens genome assemblies based on single-nucleotide polymorphisms (SNPs) relative to the reference strain ATCC 13124. Phylogroups (I–V) are indicated by branch colors. The three outer rings annotate, respectively, the presence of the beta2 variant, toxinotype, and reported host or disease association for each strain. Toxinotype A strains are highlighted with a grey circle. Figure adapted and modified from: Geier, R. R., et al.,2021 (Front Microbiol)(97).

Infection usually follows traumatic or surgical wounds that create anaerobic conditions favoring bacterial proliferation. The short incubation period and rapid spread of tissue destruction reflect the organism's fast growth and secretion of potent extracellular toxins that degrade host tissues and release nutrients, further promoting bacterial expansion. The pathogenesis of gas gangrene involves the synergistic activity of α-toxin (phospholipase C, PLC) and perfringolysin O, which disrupt host cell membranes, impair immune defenses, and promote extensive necrosis and hypoxia (16). Additional virulence factors, such as degradative enzymes (sialidases NanJ, NanI, and NanH; N-acetylgalactosaminidase EngCP; hyaluronidases; and collagenases), also contribute to tissue invasion. Adhesive proteins,

including the collagen adhesion protein (CNA) and fibrinogen-binding proteins (FbpA and FbpB), may facilitate bacterial attachment and persistence during infection (99).

The regulation of *C. perfringens* virulence is tightly controlled by environmental signals through systems such as the two-component regulator RevR and the Agr-like quorum-sensing network, which coordinate toxin and enzyme production during infection (99, 100). Insights into the roles of these regulatory pathways and associated virulence factors have been largely derived from animal models, which remain essential for elucidating disease mechanisms and evaluating new therapeutic and preventive strategies (101).

α-toxin (phospholipase C, CpPLC)

CpPLC is a zinc-dependent metalloenzyme of 370 amino acids comprising two main domains: an N-terminal catalytic domain containing three Zn^{2+} ions, and a C-terminal β-sandwich domain that mediates Ca^{2+}-dependent binding to phospholipid membranes (13, 16, 102). Within the N-terminal catalytic domain (residues 1–246), several residues are essential for metal coordination and enzymatic activity. Catalysis depends on a triad of Zn^{2+} ions coordinated by His-11, Asp-130, His-148, Glu-152, and additional supporting residues (His-68, His-126, His-136, Asp-130). Asp-56, Asp-130, and Glu-152 are particularly critical, as their substitution abolishes phospholipase and hemolytic activity, underscoring their central role in metal coordination and enzymatic activity (103–105). The C-terminal (residues 256–370), responsible for Ca^{2+}-dependent membrane interaction, contains residues that contribute to ion binding and membrane recognition, including Asp-269, Asp-336, Gly-271, and Ala-337. Key aromatic residues such as Tyr-275, Tyr-307, Tyr-331, and Phe-334 mediate membrane anchoring through hydrogen bonding and hydrophobic interactions. A hydrophobic surface loop (residues 84–88) adjacent to the catalytic and calcium-binding sites further contributes to membrane engagement, together defining the structural determinants necessary for CpPLC-mediated cytotoxicity (106–108).

The toxin binds to ganglioside receptors and Tyrosine kinase A (TrkA) in a GM1a-TrkA complex on the host cell surface. Sialic acids are critical structural components of gangliosides, and their removal by *C. perfringens* sialidases increases cellular susceptibility to PLC (109–111). Membrane interaction occurs through two complementary mechanisms:

insertion of large hydrophobic residues into the bilayer and the formation of a complex with Ca^{2+} ions and phospholipid headgroups, which stabilizes toxin binding. Then CpPLC catalyzes phospholipid hydrolysis, leading to progressive membrane destabilization (112).

CpPLC exhibits phospholipase and sphingomyelinase activities, generating the lipid mediators diacylglycerol (DAG) and ceramide, respectively, which activate intracellular signaling cascades. Additionally, PLC can hydrolyze phosphatidylethanolamine (PE), phosphatidylinositol (PI), phosphatidylserine (PS), and phosphatidylglycerol (PG)(102, 113). This broad substrate specificity may facilitate the colonization of diverse tissues and contribute to phagosome escape within macrophages. Differences in substrate affinity are determined by variations in the toxin sequence (102, 112). For example, phosphatidylcholinesterase activity was reported approximately five times higher than its sphingomyelinase activity for PLC in *C.perfringens* strain 8–6 (104). Alterations in the membrane-binding domains have been associated with variations in cytotoxic potency when comparing CpPLC with phospholipases from related species, highlighting the biological implications of these structural differences. Moreover, CpPLC activity and cytotoxicity vary among cell types, depending on the PC-to-SM ratio in the plasma membrane and local toxin concentration (102, 111).

At the cellular level, CpPLC exerts a broad range of cytotoxic effects. In erythrocytes, it causes hemolysis via direct phospholipid hydrolysis or activation of endogenous phospholipases (102). In neutrophils and endothelial cells, it induces oxidative stress, Ca^{2+} influx, and activation of signaling pathways involving TrkA, MEK/ERK, PI3K, and PKC, leading to inflammation, apoptosis, or necrosis. α-toxin also promotes platelet aggregation through intracellular Ca^{2+} mobilization and the translocation of fibrinogen receptors (gpIIbIIIa) to the cell surface, contributing to vascular occlusion and ischemia (111, 114). Additionally, CpPLC penetration of host cell membranes activates the arachidonic acid cascade and protein kinase C, resulting in the release of prostaglandins, thromboxane, and leukotrienes that intensify inflammation, vasoconstriction, and platelet aggregation (13, 115). These combined effects reduce tissue perfusion, amplify necrosis, and promote the rapid progression of gas gangrene.

Immune response and evasion mechanisms in gas gangrene

Gas gangrene is defined by a profoundly dysregulated and spatially restricted inflammatory response, with extensive tissue necrosis and minimal leukocyte infiltration. This immune impairment is primarily driven by synergic activity of CpPLC and θ-toxin (PFO), which disrupt vascular integrity and immune cell dynamics (13, 14, 116). These toxins induce endothelial activation, upregulation of adhesion molecules, and intravascular aggregation of platelets and leukocytes, leading to thrombosis and microvascular occlusion that restrict immune cell migration to infected tissues (99, 101, 111).

CpPLC also triggers suicidal NETosis in human neutrophils, forming web-like extracellular DNA structures coated with histones and enzymes, including neutrophil elastase and myeloperoxidase. However, *C. perfringens* can evade these antimicrobial defenses by secreting nucleases that degrade NETs and by suppressing leukocyte recruitment and activation (117). Moreover, CpPLC interferes with neutrophil maturation, inhibits diapedesis by promoting platelet aggregation, and disrupts cytokine-mediated chemotaxis (111, 118). In parallel, α-toxin impairs myoblast differentiation, potentially compromising muscle tissue repair and regeneration (119).

Together, these mechanisms suppress immune clearance and exacerbate vascular dysfunction, creating an ischemic and anaerobic environment that favors bacterial persistence and drives the rapid progression of clostridial myonecrosis (16).

2.1.4. Emerging *C. perfringens*-related species

WGS-based comparative genomics has become fundamental for elucidating evolutionary relationships, resolving phylogeny, and tracking the diversification of virulence determinants within the genus (97). Genomic approaches such as average nucleotide identity (ANI) analysis and phylogenomic reconstruction now provide the resolution necessary to distinguish closely related lineages that remain indistinguishable by conventional biochemical or toxinotyping assays. New human-associated species (e.g., *C. massiliamazoniense, C. pacaense*) and environmentally derived clostridia were identified through WGS-guided taxonogenomics, highlighting the ongoing discovery of previously unrecognized diversity (120, 121).

In this context, a recent genomic analysis of over 100 *C. perfringens* isolates from humans, animals, and food sources in Costa Rica revealed high diversity encompassing all previously described phylogroups (unpublished data). Two isolates initially identified as *C. perfringens* in clinical laboratories (LIBA-8841 and LIBA-8541) exhibited pronounced genetic divergence, prompting further genomic characterization that confirmed their classification as two distinct *Clostridium* species (25). Despite their phylogenetic distance, these novel taxa encode homologs of major *C. perfringens* virulence factors, including α-toxin (Plc), perfringolysin O (Pfo), and hyaluronidase (NagH), suggesting a conserved pathogenic potential.

Comparative sequence analysis of the *plc* genes of these two strains revealed low nucleotide identity to the canonical *C. perfringens* α-toxin, implying potential structural and functional variations that may influence virulence and host interactions. Such divergence also raises diagnostic challenges, as these strains could be misidentified by routine detection methods that rely on traditional toxin or gene-based assays.

By integrating genomic, phenotypic, and *in vivo* experimental approaches, this study aims to elucidate the pathogenic potential of undescribed *Clostridium* species and to provide a functional framework for interpreting their marked genomic divergence. In doing so, it underscores the relevance of these emerging *Clostridium* lineages for human health and highlights the need for continued surveillance and functional characterization beyond genomic analyses alone.

2.2 Materials and Methods

An integrated methodological approach comprising *in vitro* and *in vivo* analyses was implemented to investigate the pathogenic mechanisms of newly described species related to *Clostridium perfringens*, hereafter referred to as Cp-like strains. The *in vitro* workflow encompassed the evaluation of bacterial supernatants and recombinant phospholipase C homolog (PLC) to characterize proteomic profiles, phospholipase and hemolytic activities, and cytotoxic and cytopathic effects in cell cultures. The *in vivo* component employed a murine gas gangrene model to assess pathogenic potential and to characterize the histopathological features of tissue damage induced by these strains. The overall experimental design is summarized in Figure 14.

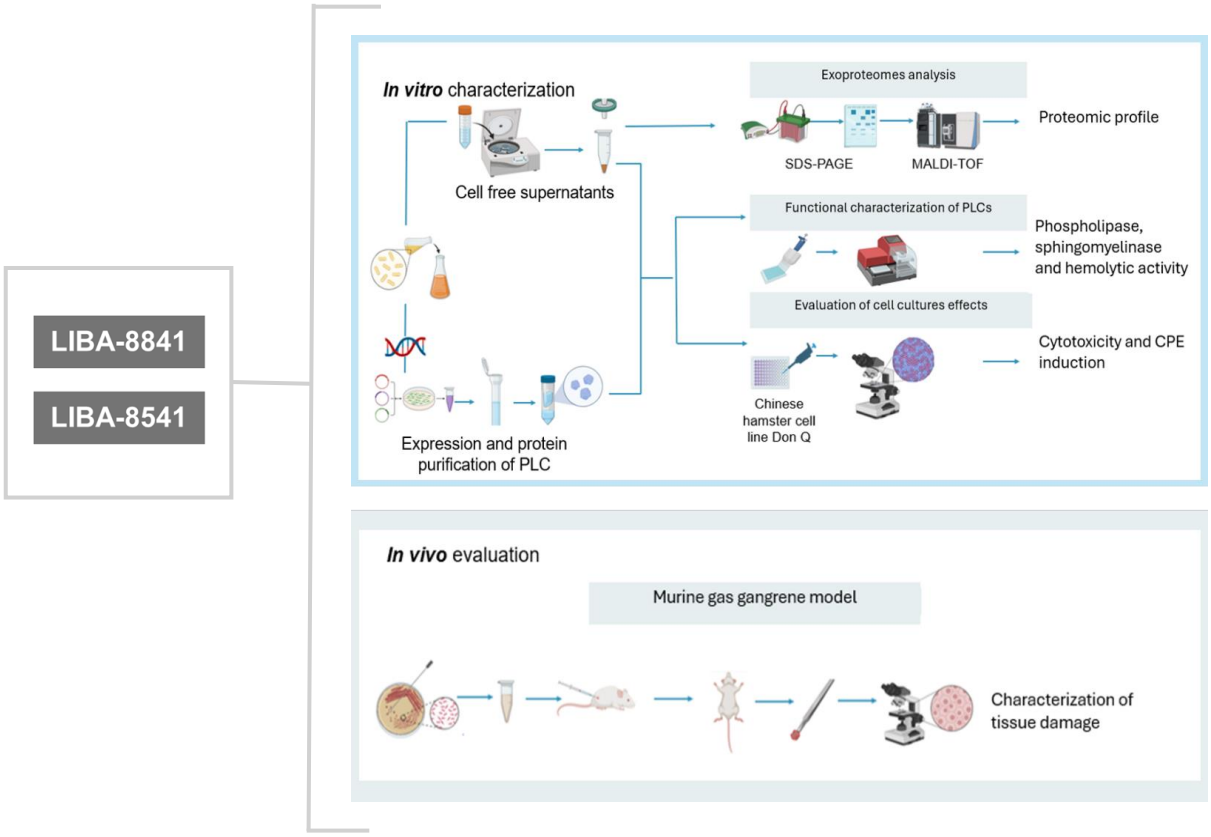

Figure 1421. Experimental design for the characterization of *Clostridium perfringens*-like strains (LIBA-8541 and LIBA-8841). The methodological workflow included *in vitro* analyses of bacterial supernatants and recombinant phospholipase C (PLC) to assess proteomic profiles, phospholipase and hemolytic activity, and cytotoxicity in the Don-Q fibroblast cell line. *In vivo* evaluation was performed using a murine gas gangrene model to examine pathogenic potential and characterize the histopathological features of tissue damage.

2.2.1 Bacterial strains

This study was conducted using two clinical isolates (LIBA-8541 and LIBA-8841), previously subjected to comprehensive genomic characterization and reported by Rodríguez et al.(2020) (25) as isolates 27733 and 27737 and referred to as Cp-like strains. These strains were originally submitted to the Anaerobic Bacteriology Research Laboratory (LIBA) for confirmation of their low-confidence identification as *Clostridium perfringens* by MALDI-ToF and were recovered from human cases of soft-tissue infections at the Trauma Hospital in Costa Rica.

As previously described (25), whole-genome sequencing revealed that both isolates display average nucleotide identity (ANI; ~87%) and digital DNA–DNA hybridization (dDDH; ~35%) values below the accepted species thresholds for *C. perfringens*, supporting their classification as unassigned *Clostrium*-like species. Raw sequence reads were deposited in the European Nucleotide Archive (ENA) under the project accession number PRJEB41321.

Phenotypically, the isolates exhibited rapid growth in BHI broth, double hemolysis on blood agar, and lecithinase activity on egg-yolk agar, consistent with *C. perfringens*-like traits. Genomic analyses further revealed the presence of genes encoding toxins and virulence-associated factors typically found in *C. perfringens*, including *plc* (alpha toxin), *pfoA* (perfringolysin O, theta toxin), *nagHIJKL* (hyaluronidase, μ-toxin), *nanHIJ* (exo-α-sialidase), and *cloSI* (α-clostripain) (25).

2.2.2 Identification of differences in *plc* at the sequence level

The complete genome sequences of the *C. perfringens*-like strains were generated with long-read assemblies were constructed using a Sequel II PacBio sequencer at the Leibniz Institute DSMZ (Braunschweig, Germany)(un published data) and annotated with Prokka v1.13 and Bakta. PLC protein sequences from the Cp-like strains were manually extracted from the annotated genomes and confirmed by manual curation. These sequences were aligned against a dataset of 98 reference *C. perfringens* PLC sequences retrieved from GenBank. Multiple sequence alignments were prepared with Clustal in Seaview to identify amino acid substitutions and then analyze if the sequence location is in regions of known functional importance. A subsequent literature review was then conducted to map these differences onto

the functional domains of the toxin and to assess their potential implications for its biological activity.

2.2.3 Expression and protein purification of recombinant PLC

Synthetic gene fragments (gBlocks) encoding the PLC sequences from strains LIBA-8841 and LIBA-8541 were cloned into the expression vector pET30a. The inserts were codon-optimized for *E. coli* and ligated using the XbaI/BlpI restriction sites following a uniform cloning strategy for both genes. The resulting constructs were initially transformed into *E. coli* TOP10 cells, and plasmids carrying the expected inserts were purified using standard miniprep procedures. Transformation of *E.coli* BL21 competent cells was performed using a protocol described in pET System Manual (Novagen). Competent cells were thaw on ice until completely resuspended. 100 µl of competent cells were transferred into pre-chilled tubes, followed by the addition of 2µl of 2-mercaptoethanol (1:10). Tubes were kept on ice for 10 min and gently mixed every 2 min. 2 µl of plasmid (25 ng/µl) was added, mixed and incubated on ice 30 min. Tubes were placed on 42°C water bath for exactly 20 sec, then placed on iced for 2 min. Then, 900 µl of SOC medium was added to each tube and incubated with shaking for 1h at 37°C. *E.coli* transformants were selected on LB agar containing 50 µg/mL kanamycin. Moreover, acquisition of plasmid DNA was confirmed through agarose gel electrophoresis of minipreps.

2.2.4 PLC expression and purification

Transformed *E. coli* colonies carrying the PLC-encoding plasmids were used to inoculate 10 mL of LB medium supplemented with kanamycin (50 µg/mL). After overnight incubation at 37 °C with shaking, the entire culture was transferred to 250 mL of fresh LB medium containing kanamycin (50 µg/mL) and incubated at 37 °C with agitation until the optical density at 600 nm (OD600) reached approximately 0.5. Protein expression was induced by adding IPTG to a final concentration of 100 µM. Cultures were then incubated for an additional 16 h at 37 °C with agitation (122). Cells were harvested by centrifugation at 3000 × g for 10 min at 4 °C.

Cell pellets were thawed on ice for 15 min and resuspended in 10 mL of native lysis buffer (Qiagen), supplemented with lysozyme and Benzonase® nuclease. The suspension was then incubated on ice for 30 min with occasional gentle mixing to ensure homogeneity. Cell debris

was removed by centrifugation at 14,000 × g for 30 min at 4 °C, and the clarified supernatant containing the soluble protein fraction was subsequently collected.

Purification of 6xHis-tagged proteins was performed using Fast Start columns (Qiagen) (122) prepacked with Ni-NTA resin, following the manufacturer's recommendations. The resin was equilibrated by inverting the column several times and draining the storage buffer. Clarified lysates were applied onto the column, and the flow-through was collected. The column was washed twice with 4 mL of native wash buffer, and both wash fractions were retained. Bound proteins were eluted using two 1 mL aliquots of native elution buffer. Aliquots from the flow-through, wash, and elution fractions were mixed with 2x SDS-PAGE sample buffer and resolved by SDS-PAGE.

Purified elution fractions were concentrated to a final volume of 500 µL using a centrifugal evaporator (Genevac miVac system) (123). Total protein concentration was determined using the Bradford dye-binding method (Bio-Rad), following the manufacturer's instructions. Final protein preparations were stored in 25 µL aliquots at −80 °C.

2.2.5 Functional characterization of PLCs

Phospholipase C enzymatic assays

The enzymatic activity of purified PLC proteins was assessed using a colorimetric phospholipase C activity assay kit (CS 0011 Sigma-Aldrich), based on the hydrolysis of the chromogenic substrate, *p*-nitrophenylphosphorylcholine. PLC-mediated cleavage releases *p*-nitrophenol, which produces a yellow color measurable at 405 nm under near-neutral pH conditions (pH 7.2–7.5). The change in absorbance is directly proportional to PLC activity. One unit of PLC activity was defined as the amount of enzyme required to produce 1 µmol of product per minute at 37 °C, with activity values normalized to protein content and expressed as mU/mg.

Sphingomyelinase (SMase) activity was determined using a coupled enzyme assay (MAK152 Sigma-Aldrich) that generates a chromogenic product measurable at 655 nm. The absorbance is proportional to the SMase activity in the sample.

As a positive control for PLC activity, lyophilized phospholipase C from *C. perfringens* Type XIV (Sigma-Aldrich, Lot #0000138274), resuspended in phosphate-buffered saline (PBS),

was used under the same conditions. Enzymatic activity determinations were performed in triplicate.

Lecithinase activity was evaluated using a spot assay on egg yolk agar (124). Wells were made in the agar, and 10 µL of each purified enzyme preparation were pipetted into the wells. Lecithinase activity hydrolyzes lecithin into insoluble diglycerides and phosphorylcholine, forming a white, opaque precipitate that extends beyond the edge of the wells. The diameter of the opalescent halo was measured as an indicator of lecithinase activity. Recombinant PLC from *C. perfringens* expressed in *E. coli* (provided by Dr. Laura Monturiol, Instituto Clodomiro Picado) was included as a positive control (Cp-PLC).

PLC hemolytic activity

Hemolytic activity was assessed as previously described (15), with minor modifications. Briefly, human erythrocytes were suspended in 0.02 M Tris–HCl buffer (pH 7.5) containing 0.9% NaCl (Buffer 1), centrifuged at 1100 × g for 3 min, and washed five times in the same buffer. Erythrocytes were enumerated using a hemocytometer, and cells were resuspended in TBS supplemented with 1 mM $CaCl_2$ and 0.5 mM $ZnCl_2$ (Buffer 2), required for PLC membrane binding and catalytic function, respectively (108).

A total of 0.1 mL of erythrocyte suspension containing aprox. 1.5×10^6 cells/mL was incubated with various concentrations (2-10 µg) of purified PLCs in 0.5 mL of Buffer 2 at 37 °C for 20 min. Following incubation, samples were chilled at 4 °C for 10 min and subsequently maintained at room temperature for hemolysis measurements at various time points. Hemolysis was quantified by measuring hemoglobin release in the supernatant at 550 nm, after removing intact cells by centrifugation at 1100 × g for 3 min. Hemolytic activity was expressed as the percentage of total hemoglobin released, using erythrocytes lysed in 0.4% NaCl as a positive lysis control (125).

Phospholipase C from *C. perfringens* Type XIV (Sigma-Aldrich, Lot #0000138274) was used as a positive control under the same conditions.

2.2.6 Exoproteome composition analysis

In order to analyze the exoproteome of the strains LIBA-8841 and LIBA-8541, and the reference strains *C. perfringens* JIR325 and SM101, were grown overnight (ON) in Reinforced Clostridial Medium (RCM, Appendix 7) under anaerobiosis at 37°C to prepare a preinoculum. This was used as seed culture in a 250 ml Erlenmeyer, which was incubated ON at 37°C. The stationary phase culture was centrifuged at 3000rpm for 30min, then filtered through a 0.22 µm pore size membrane. Three independent biological replicates were prepared for each strain and Aliquots of the resulting cell-free supernatants were stored at −20 °C.

Aliquots of 1.5 mL of cell-free supernatants were then concentrated using a vacuum centrifuge to a final volume of 0.1 mL. A 15 µL portion of each sample was applied to SDS-PAGE under reducing conditions (Appendix 2) and concentrated into a single band by stopping the electrophoresis as soon as the migration front entered 3–4 mm of the resolving gel. Gels were stained with Coomassie Brilliant Blue using standard protocols, and bands were excised and subjected to reduction with 10 mM dithiothreitol for 30 min at 56 °C, alkylation with 50 mM iodoacetamide for 20 min in the dark, and digestion with sequencing grade trypsin at 37°C overnight in an automated workstation (Intavis). The resulting tryptic peptide mixture was dried by vacuum centrifugation, redissolved in 0.1% formic acid, and subjected to RP-HPLC on a nano-Easy 1200® chromatograph (Thermo) in-line with a Q-Exactive Plus® mass spectrometer (Thermo). Ten µL of the peptide mixture were loaded on a C18 trap column (75 µm × 2 cm, 3 µm particle; PepMap, Thermo), washed with 0.1 % formic acid (solution A), and separated at 200 nL/min on a C18 Easyspray® column (75 µm × 15 cm, 3 µm particle; Thermo). A gradient toward solution B (80 % acetonitrile, 0.1 % formic acid) was developed in a total of 110 min (1 % B for 3 min, 1–26 % B in 62 min, 26–99 % B in 30 min, and 99 % B for 15 min). MS spectra were acquired in positive mode at 1.9 kV, with a capillary temperature of 200°C, using 1 µscan in the range 400–1600 m/z, maximum injection time of 50 ms, AGC target of 1 × 106, and resolution of 70,000. The top 10 ions with 2–4 positive charges were fragmented with an AGC target of 1 × 105, minimum AGC 2 × 103, maximum injection time 110 ms, dynamic exclusion time 5 s, and resolution 17,500. MS/MS spectra were processed against protein sequences contained in custom

databases that were derived from the annotated genomes using Peaks X® (Bioinformatics Solutions), and matches were assigned to known protein families by similarity. Cysteine carbamidomethylation was set as a fixed modification, while deamidation of asparagine or glutamine, and methionine oxidation, were set as variable modifications, allowing up to 3 missed cleavages by trypsin.

Parameters for match acceptance were set to FDR < 0.1 % and -10lgP protein score ≥ 50. Functional categorization was determined using orthologous group clusters in the COGnitor tool (126). The relative abundance of each identified protein was calculated from the area under the curve (AUC), and the corresponding standard deviation was determined from three replicates per strain.

Cell-free supernatants from two *C. perfringens* type A strains, JIR325 and SM101, were obtained following the above protocol to compare their exoproteomes with those of the *C. perfringens*-like isolates. These reference strains were selected due to their relevance in the study of *C. perfringens* pathogenesis: JIR325 is a widely used model strain for virulence (117, 127) characterization, and SM101 has been extensively analyzed in transcriptomic studies under various conditions (128, 129). Protein profiles were obtained as described above.

Comparisons were performed based on protein identity and the mean relative abundance across three biological replicates per strain. To visualize the global differences among the exoproteomes, a non-metric multidimensional scaling (NMDS) analysis was conducted using Euclidean distances calculated on Hellinger-transformed abundance data. The analysis was implemented in Python, using the scikit-learn library for NMDS and the scipy library for distance-matrix computations. A bootstrap approach (n = 1000 iterations) was used to estimate confidence intervals and assess the robustness of the strain clustering. Ellipses representing 95% confidence regions were computed using chi-squared distributions and overlaid on the ordination plot. Additionally, Pearson correlation coefficients were calculated between each protein and the two NMDS axes to identify the top 10 proteins most associated with each dimension.

To evaluate the variability among biological replicates and determine whether differences across strains were statistically significant, Bray–Curtis dissimilarity indices were calculated

between all replicate pairs for each strain using protein relative abundance data. Protein profiles were first Hellinger-transformed and normalized to proportions. Pairwise Bray–Curtis distances were computed within each strain, and the mean and standard deviation of the dissimilarities were used as a measure of inter-replicate variability. To statistically compare the variability across strains, a Kruskal–Wallis test was performed on the Bray–Curtis distributions obtained for each group.

2.2.7 *In vitro* evaluation of Cp-like supernatants

Cytopathic and cytotoxic assays.

Chinese hamster fibroblasts (Don Q), a cell line characterized by increased susceptibility to CpPLC due to reduced ganglioside content in the plasma membrane (130), were cultured in Eagle's Minimal Essential Medium (MEM) supplemented with 10% fetal bovine serum (FBS), L-glutamine (5 mmol/L), penicillin (100 U/mL), and streptomycin (100 µg/mL), in a 5% CO_2 atmosphere. Two-fold serial dilutions of cell-free supernatants were applied to fibroblast monolayers seeded in 96-well plates. After 24 hours of incubation, CPEs were assessed by observing morphological alterations in the monolayer under light microscopy.

In parallel, cell viability was evaluated using the MTT assay (131). Briefly, 10 µL of MTT substrate (3-(4,5-dimethylthiazol-2-yl)-2,5-diphenyltetrazolium bromide) (5mg/ml) were added to 100µL medium on each well (for a 0,5mg/ml final concentration), and after 1 hour of incubation, absorbance was measured at 570 nm using a Cytation™ 3 microplate reader (BioTek). Cell survival was expressed as a percentage, considering wells incubated only with MEM as 100% viability, and wells incubated with a 1:100 dilution of recombinant PLC from *C. perfringens* expressed in *E. coli* (provided by Dr. Laura Monturiol, Instituto Clodomiro Picado) as 100% cytotoxicity control.

All experiments were replicated 3 to 6 times. Each replicate included a neutralization step in which the supernatants were incubated with a polyclonal anti-CpPLC antibody (0.024 mg/mL), produced in rabbits and purified by affinity chromatography. This antibody preparation was provided by Dr. Marietta Flores Díaz and Dr. Laura Monturiol at the Clodomiro Picado Institute and used to confirm the specific involvement of PLC, if present in supernatants, in cytotoxicity.

Differences among strains were analyzed using the Kruskal-Wallis with Tuckey post-hoc test. A p-value < 0.05 was considered statistically significant.

2.2.8 *In vivo* evaluation of the pathogenesis of the Cp-like strains

Murine gas gangrene model

The murine gas gangrene model was conducted using three treatment groups: one group inoculated with strain LIBA-8541, one group inoculated with strain LIBA-8841, and a positive control group inoculated with the reference strain *Clostridium perfringens* ATCC 3624. Each group consisted of three BALB/c mice (20–25 g). For each animal, the left hind thigh was injected with the bacterial inoculum, whereas the contralateral right hind thigh received sterile Dulbecco's phosphate-buffered saline (DPBS) and served as an internal negative procedural control.

Aliquots of 2 mL from a 1:250 dilution of overnight cultures grown in fluid thioglycolate medium (FTG; Difco Laboratories) were inoculated into 250 mL of tryptone yeast (TY) broth and incubated anaerobically at 37 °C for 5 h. After incubation, cultures were washed with sterile DPBS. An aliquot of 50 µL, corresponding to 10^8 CFU/mL, was injected intramuscularly into the left hind thigh of each mouse. Mice were euthanized by cervical dislocation 8 h post-infection, and skeletal muscle samples were collected for analysis (101). (Detailed protocol available in Appendix 8.)

Histological analyses

Histopathological analyses were performed as previously described (106). Infected muscle tissue was fixed by immersion in 10% buffered formalin (pH 7.2) for 24 to 72 hours. Tissue sections (4 µm thick) were prepared using routine procedures and stained with H/E and Gram stain. Slides were examined microscopically, and lesion severity was assessed using a semiquantitative ordinal scale that ranges from 0 (no lesions) to 5 (severe lesions). The scoring criteria for H/E staining included edema, hemorrhage, inflammatory cell infiltration, and alterations in muscle fibers (loss of striations, cytoplasmic loss, vacuolation, swelling, and hypercontraction bands). Bacterial load was evaluated by Gram staining. All parameters were considered to determine the overall score for each section**.** Statistical comparisons were

performed using the Kruskal–Wallis test followed by Dunn's multiple-comparison post hoc test, with $p < 0.05$ considered statistically significant.

Bacterial recovery and genomic confirmation to establish lesion causality

To establish the causality of the observed lesions, gastrocnemius muscles were dissected under aseptic conditions. One section from each hind limb was macerated, suspended in sterile PBS, and vortexed. A 1:10 dilution was prepared, and 100 µL of both undiluted and diluted suspensions were plated on brain heart infusion (BHI) agar supplemented with egg yolk and SFP agar (Shahidi Ferguson perfringens TSC Agar, BD Difco). Plates were incubated anaerobically at 37 °C for 24 hours. Colonies exhibiting typical *C. perfringens* morphology were randomly selected and pooled by treatment group, then subcultured in BHI broth for DNA extraction. Cultures from each group were subjected to WGS-based identification. To this end, Illumina 2x250bp paired-end reads were mapped to the genomes of the inoculated strains using bowtie2.

All animal proceedings were in compliance with local legislation (Ley de Bienestar de los Animales N° 7451) and approved by the Comité Institucional de Cuido y Uso de Animales (CICUA) from the Universidad de Costa Rica (CICUA 73-2023). Procedures were conducted under Dr.Uzal protocol and supervision at School of Veterinary Medicine, University of California, San Bernardino.

2.3 Results

Amino acid substitutions in PLC suggest differential toxin activity in *C. perfringens*-like strains

The *plc* encoding genes from LIBA-8541 and LIBA-8841 strains share approximately 86% nucleotide identity, and show lower identity with the PLC gene from *C. perfringens* ATCC 13124 (82% and 79%, respectively). At the amino acid level, the Plc of the *C. perfringens*-like strains show difference to 98 previously described *C. perfringens* PLCs, mostly at the C-terminal domain (Table 4). Amino acid substitutions were also identified at critical residues for enzymatic activity (102, 106), including calcium-binding sites (D269Y, A337D) and exposed hydrophobic residues. Additional differences were observed in membrane-interacting regions, such as the Y331F substitution, previously associated with reduced

hemolytic activity and cytotoxic potency (107)(Table 4). These sequence-based differences were identified through *in silico* analyses and, while suggestive of functional divergence, require experimental validation using targeted functional approaches, such as site-directed mutagenesis.

Table 4. Amino acid substitutions in Cp-like phospholipase C compared to critical residues of *C. perfringens* PLC.

Critical residues for membrane–protein interactions [a]

Site	LIBA-8541	LIBA-8841
78–83	S79T, K80N, S83K	S83N
139–154	A146P	A146P
208–217	S209N, H212R	S209N, S211N, H212C, D243E
268–275	D269Y	K268D, D269Y, D273N
293–301	ns	N297D, T301S
329–337	R329S, Y331F, A333E, P335G, A337D	R329S, Y231F, A333E, P335A, A337D

Critical residues for the PLC activity [a]

Site	LIBA-8541	LIBA-8841
N-terminal	A87S, A146P	A87S, A146P
C - terminal	D269Y, Y331F, A337D	D269Y, Y331F, A337D

a. Residues listed correspond to critical sites previously identified in structural and functional analyses of *C. perfringens* PLC (106- 109). ns: no substitutions identified

To evaluate the phospholipase C activity of the Cp-like enzymes, recombinant proteins were expressed in *E. coli*, purified as His_6-tagged constructs, and analyzed by SDS-PAGE. The electrophoretic mobility of the purified proteins corresponded to the expected molecular mass (~43 kDa) (Supplementary Figure 6). Lecithinase activity of both recombinant toxins resulted in opaque halos of approximately 4.5 mm in diameter (Supplementary Figure 7). Phosphatidylcholine hydrolysis was confirmed by ELISA (Sigma-Aldrich) (Fig.15). Besides, both Cp-like enzymes induced a dose- and time-dependent increase in hemolysis of human erythrocytes (Supplementary Figure 8).

Although no statistically significant differences were detected between the two Cp-like strains, LIBA-8541 exhibited higher hemolytic activity than LIBA-8841, whereas LIBA-8841 displayed greater phosphatidylcholine hydrolysis, suggesting subtle differences in substrate affinity or catalytic efficiency under the tested conditions (Fig. 15). When compared with the CpPLC control, both enzymes exhibited markedly reduced activity, with hemolytic

activity and phosphatidylcholine hydrolysis levels approximately threefold lower (Kruskal–Wallis, p = 0.002 and p = 0.027, respectively).

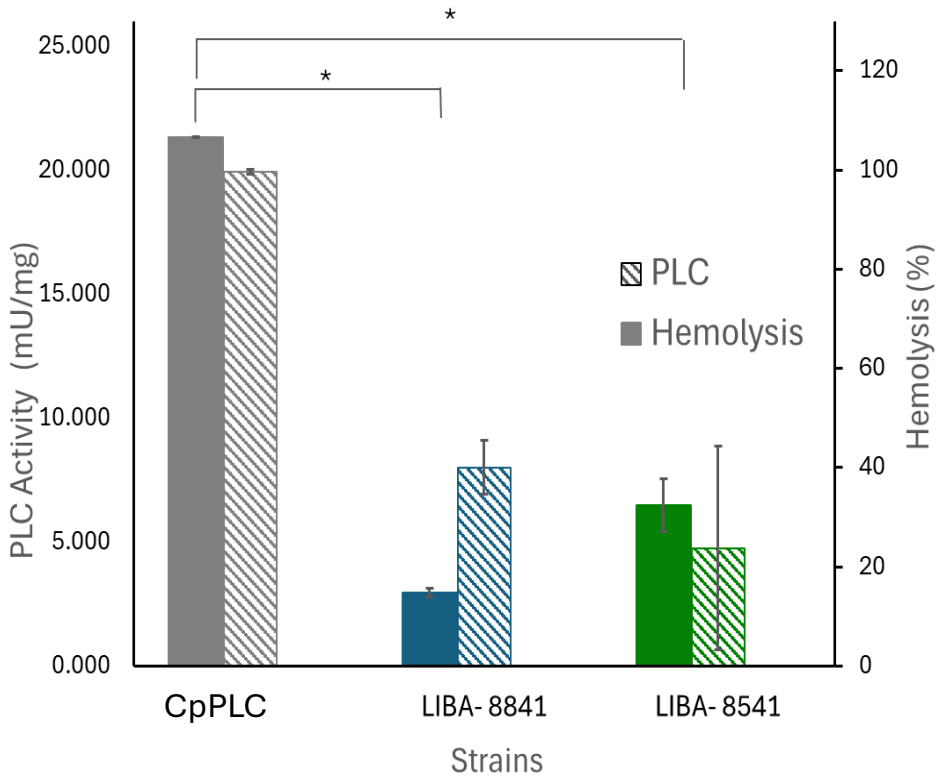

Figure 15. *In vitro* functional characterization of PLCs from LIBA-8841 and LIBA-8541. The enzymatic activity of purified PLC proteins was assessed using a colorimetric phospholipase C activity assay kit (Sigma-Aldrich). One unit of PLC is defined as the amount of enzyme required to produce 1 µmol of product per minute under the assay conditions at 37 °C (left axis). Hemolytic activity was assessed by measuring hemoglobin release in the supernatants at 550 nm after 5 h of incubation of human erythrocytes incubated with 2ug/ml of recombinant PLC from Cp-like LIBA-8841 and LIBA-8541 in 0.5 ml (right axis). PLC from *Clostridium perfringens* (*C. welchii*) Sigma-Aldrich (2U/ml) was included as positive control. Statistical analyses were performed using a Kruskal–Wallis test followed by Dunn's post hoc comparison; * $p < 0,05$.

The cytopathic and cytotoxic effects induced by Cp-like supernatants involve PLC-dependent mechanisms.

Based on the *in vitro* results with purified toxin, cell-free supernatants from overnight cultures were used to evaluate cytopathic and cytotoxic effects in ganglioside-deficient DonQ cells (130). An apparent cytopathic effect was observed in wells exposed to 1:2 dilutions of the supernatants, including partial monolayer disruption, emergence of clearance zones, and cell rounding (Fig. 16). Despite the relatively low phospholipase activity of LIBA-8541 and LIBA-8841 PLCs, both Cp-like supernatants induced a greater (81.14 % and 95,48%

respectively) reduction in cell viability compared to the reference strain *C. perfringens* ATCC 13124 (56.76%). This difference was significant for LIBA-8841 ($p = 0.005$), whereas LIBA-8541 did not differ significantly from the reference strain ($p = 0.259$) (Fig. 17).

The addition of anti-PLC antibodies partially protected the cell monolayer from both cytopathic and cytotoxic effect (Fig. 16 and 17). Neutralization significantly reduced cell killing by 21.44% for LIBA-8841 ($p = 0.029$) and 20.38% for LIBA-8541 ($p = 0.029$). This protective effect was consistent with the reduction observed for the *C. perfringens* reference strain (35.00%, $p = 0.021$) (Fig. 17).

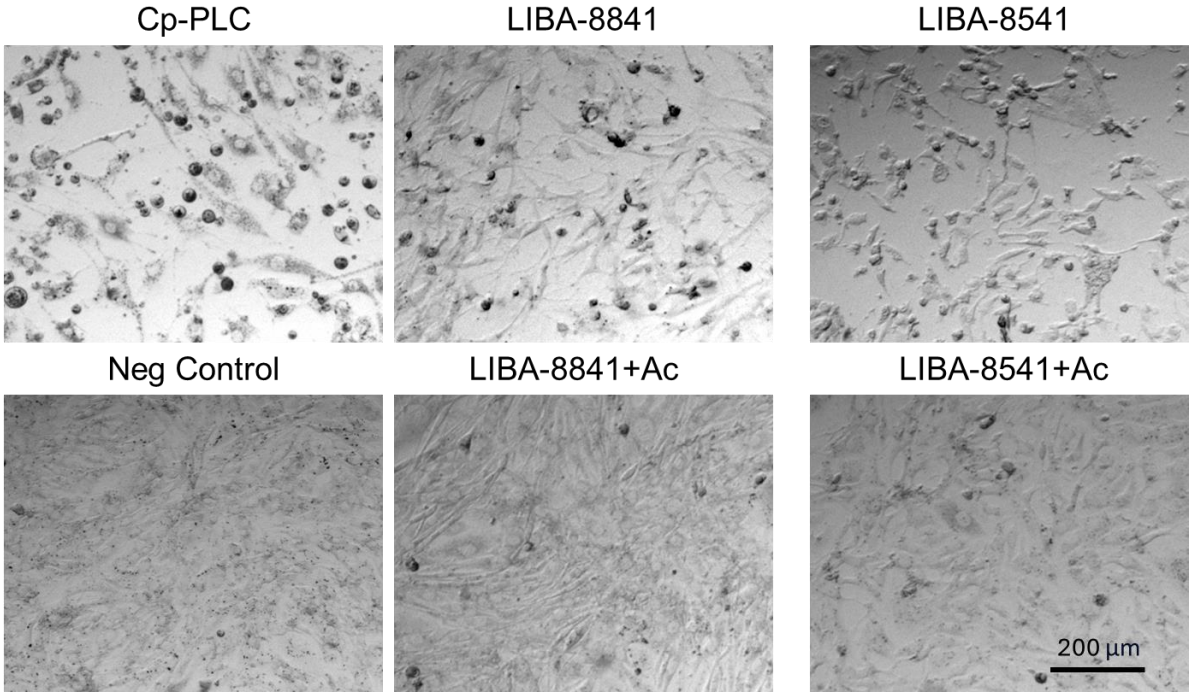

Figure 16. Cytopathic effects (CPE) induced by LIBA-8841 and LIBA-8541 strain supernatants in DonQ cell cultures. DonQ monolayers were exposed overnight to 1:20 dilutions of cell-free supernatants from LIBA-8841 and LIBA-8541, resulting in characteristic CPE including monolayer disruption, clearance zones, and cell rounding. Purified recombinant PLC from *C. perfringens* expressed in *E. coli* (provided by Dr. Laura Monturiol, Instituto Clodomiro Picado) (Cp-PLC) was included as a positive control of CPE induction. Neutralization assays performed by incubating supernatants with a polyclonal anti-CpPLC antibody (Ac) (0.024 mg/mL), produced in rabbits and purified by affinity chromatography. partially protected the cell monolayer, preserving morphology similar to the DMEM control (Neg Control).

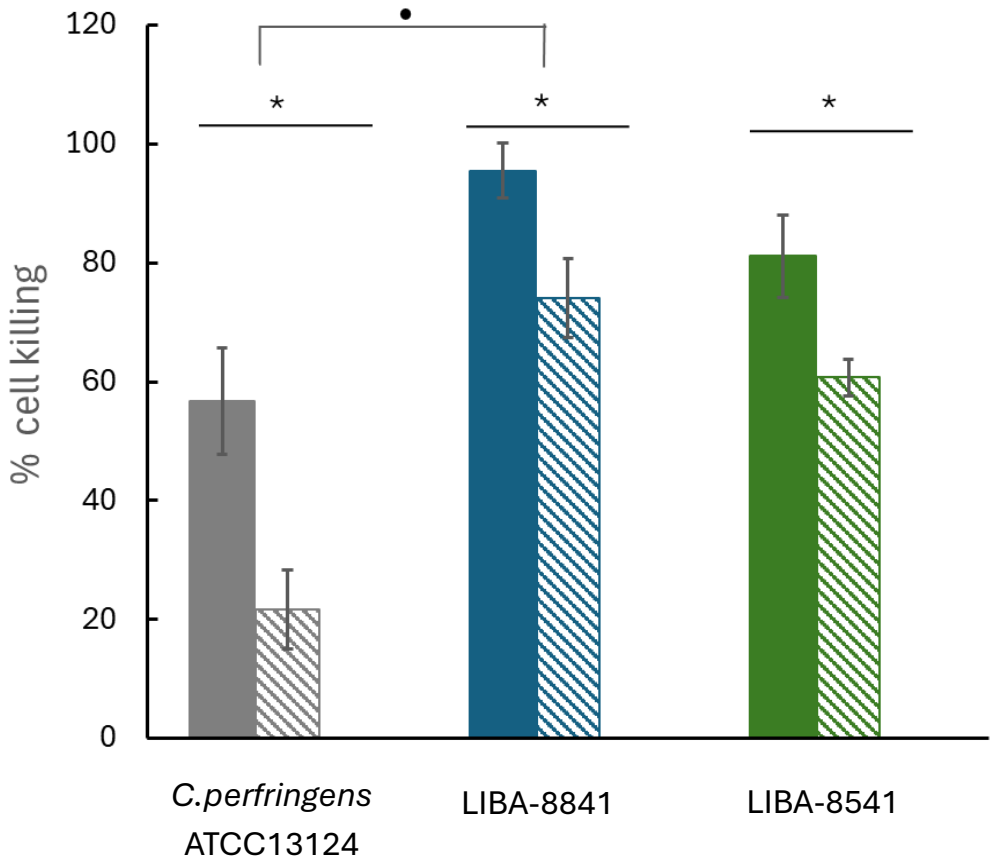

Figure 17. Cytotoxic effects induced by cell-free supernatants of LIBA-8841 and LIBA-8541 strain supernatants on Don-Q cells. Don-Q cells were incubated ON with cell-free supernatants from each strain, in the presence or absence of an anti-PLC antibody. Cell viability was assessed using the MTT assay. The percentage of cell killing was calculated by normalizing absorbance values to 100% viability defined as the signal from untreated cells (DMEM only), and 100% cell death defined as the signal from cells treated with purified Cp-PLC showing complete cytopathic effect. Black bars represent the mean ± SE. Statistical differences between each strain and its corresponding anti-PLC-treated condition (striped bars) were evaluated using a two-tailed Mann–Whitney test (* p value < 0.05). Differences among strains were analyzed using the Kruskal–Wallis test with and pos hoc Tuckey method (• p value < 0.05 **).**

The extracellular proteome of LIBA-8841 and LIBA-8541 contains virulence factors commonly associated with *C. perfringens*

Proteins in the supernatant of LIBA-8841 and LIBA-8541 cultures, and of *Clostridium perfringens* type A strains SM101 and JIR325 during the stationary phase of growth in RCM medium, were analyzed using mass spectrometry. A total of 264 and 321 proteins were identified in the exoproteomes of LIBA-8541 and LIBA-8841, respectively (Supplementary Table 1 &2). The most abundant exoproteins, which together accounted for approximately 75% of the total detected protein abundance, were predicted to be involved in carbohydrate

transport and metabolism, lipid transport and metabolism, and energy production and conversion. Among them, immunogenic proteins, such as acetyl-CoA acetyltransferase and translation elongation factors (132), were also identified (Table 5).

The identified proteins include virulence factors implicated in *C. perfringens* pathogenesis such as the cell wall-associated hydrolase SagA, which plays a role in host invasion (132) and was among the most abundant proteins detected representing 2.161% and 1.011% in LIBA-8541 and LIBA-8841 respectively. CpPLC was found in a similar relative abundance for both strains (LIBA-8541=0.038% vs. LIBA-8841=0.034%) with no significant difference compared to *C.perfringens* SM101 (0.034%) (Kruskall-Wallis $p = 0.837$) (Table 5). Furthermore, eight different predicted peptidases and an additional 5′-nucleotidase were identified in both strains. LIBA-8841 also presented three additional enzymes with roles in virulence (collagenase, exodeoxyribonuclease and ornithine carbamoyltransferase).

To assess intra-strain variability across biological replicates, the Bray–Curtis dissimilarity index was calculated based on the proteomic profiles of each strain. Among the strains analyzed, LIBA-8841 showed a higher degree of variability between replicates (Supplementary Fig. 9). However, this trend was not supported by statistically significant differences when variability was compared across strains using a Kruskal–Wallis test ($p > 0.05$).

Table 5. Proteins identified in cell free supernatants from LIBA-8841 and LIBA-8541 Cp-like strains

Most abundant proteins			LIBA-8541		LIBA-8841		Cp SM101	
Accesion	Description	COG	%	SD	%	SD	%	SD
AGCDLC_00605	type I glyceraldehyde-3-phosphate dehydrogenase	G	27.078	14.689	23.812	33.521	25.915	7.472
COAOJB_04550	Chaperone protein DnaK	O	10.862	3.034	15.174	2.560	14.580	6.486
AGCDLC_12795	3-hydroxyacyl-CoA dehydrogenase	I	6.600	1.988	2.754	0.552	1.238	0.261
COAOJB_00620	Glyceraldehyde-3-phosphate dehydrogenase	G	0.001	0.002	7.611	2.821	0.000	-
AGCDLC_05290	Acetyl-CoA acetyltransferase	G	5.302	2.874	1.716	1.471	1.577	0.823
AGCDLC_16030	Rubrerythrin	C	3.382	3.496	3.430	2.560	1.554	0.897
AGCDLC_00595	triose-phosphate isomerase	C	3.469	2.077	3.184	1.318	3.381	0.673
AGCDLC_12810	Acyl-CoA dehydrogenase related to the alkylation response protein AidB	I	4.286	2.616	2.090	2.640	1.237	0.849
AGCDLC_00005	GGGtGRT protein	S	2.908	1.135	2.643	1.894	1.208	0.670
AGCDLC_12640	glucose-6-phosphate isomerase	G	2.743	0.302	2.450	0.552	2.079	0.674
AGCDLC_00010	Fe-S cluster assembly scaffold protein IscU NifU family	P	1.895	0.497	3.085	1.249	0.856	0.543
AGCDLC_12815	Enoyl-CoA hydratase/carnithine racemase	I	2.527	1.079	0.780	0.856	0.176	0.026
AGCDLC_10715	SagA protein	M	2.161	2.108	1.011	1.221	0.023	0.033
AGCDLC_10290	6-phosphofructokinase	G	1.765	0.309	1.381	0.452	1.234	0.683
AGCDLC_13390	elongation factor G	J	0.051	0.032	2.958	-	0.387	0.383
Potential virulence factors								
AGCDLC_15620	Phospholipase C	M	0.038	0.021	0.034	0.021	0.057	0.049
WP_0115900921	collagenase ColA	R	0.000	-	0.048	-	0.000	-
AGCDLC_14110	Exodeoxyribonuclease VII small subunit	L	0.000	-	0.020	-	0.000	-
AGCDLC_14915	ornithine carbamoyltransferase	E	0.000	-	0.008	-	1.773	2.002

COG: Functional category; **%** Relative abundance; **SD:** standard deviation in 3 replicates; - protein identified just in one replicate.

The table shows the proteins with the highest relative abundance in the exoproteomes of LIBA-8841 and LIBA-8541 (representing ~75% of the total detected abundance). The corresponding relative abundances (%) detected in the exoproteome of the reference *C. perfringens* type A strain SM101 are also shown. Additionally, the table includes the relative abundance of putative virulence factors detected in the exoproteomes.

Divergent exoproteome profiles separate LIBA-8841 and LIBA-8541 from canonical *C. perfringens*

Subsequently, a NMDS analysis was performed using Hellinger-transformed data and Euclidean distances with bootstrap support to assess inter-strain relationships (Fig 18). The two *C. perfringens* type A reference strains, SM101 (8380) and JIR325 (8937), displayed the greatest similarity. In contrast, LIBA-8541 and LIBA-8841 showed the greatest separation from each other and from the reference strains, highlighting marked divergence in protein profiles. LIBA-8841 was the most divergent, while LIBA-8541 clustered more closely with the *C. perfringens* group, though with minimal overlap. The top ten proteins contributing most to the separation along each NMDS axis are involved in carbohydrate-, amino acid- and ion-transport and metabolism (Supplementary Table 3).

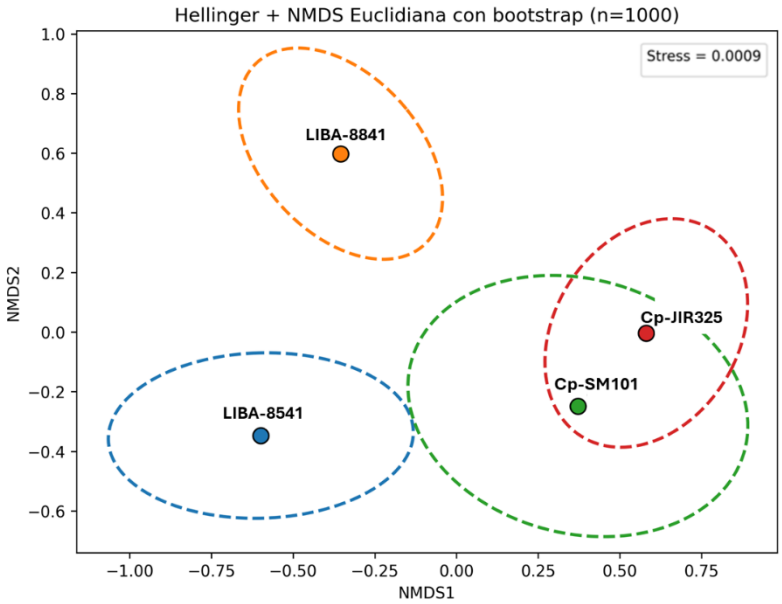

Figure 18. Non-metric multidimensional scaling (NMDS) plot representing the comparative exoproteome profiles of the *Clostridium perfringens*-like isolates and two reference *C. perfringens* type A strains (JIR325, 8937; and SM101, 8380). The analysis was performed on Hellinger-transformed protein abundance data using Euclidean distance, and 95% bootstrap confidence ellipses (n = 1000) were added to assess clustering robustness. Each point represents a strain, and ellipses denote the resampled confidence regions for each proteomic profile. The two reference strains clustered closely, reflecting their high exoproteomic similarity, whereas the *C. perfringens*-like isolates displayed distinct profiles relative to both reference strains. Stress value = 0.0009.

LIBA-8541 and LIBA-8841induce tissular damage in a mouse model of gas gangrene

Prompted by the observed differences in their exoproteomes compared to *C. perfringens*, we tested the LIBA strains in a gas gangrene mouse model to confirm their pathogenicity and characterize their virulence. The onset and progression of gas gangrene was rapid, with mice from each group showing signs of limping and swelling of the footpads and thighs as early as 4h post-infection. Grossly, LIBA-8841 and LIBA-8541 induced comparable edema, swollen, and congestion in affected legs. The reference strain *C.perfringens* ATCC 3624, instead, induced dark-red discoloration of the affected skeletal muscle (Fig. 19 and 20).

Among the histological changes observed in the skeletal muscle, *C. perfringens* ATCC 3624 caused several instances of muscle degeneration, characterized by myonecrosis with separation of muscle fibers, hypercontraction bands, vacuolation, loss of striations, and cytoplasm. LIBA-8841 induced hypercontraction of fibers and cytoplasm vacuolation, resulting in mild muscle degeneration. LIBA-8541 caused less severe muscle degeneration than *C. perfringens* ATCC 3624 (Kruskal–Wallis test followed by Dunn's post hoc test with

Bonferroni correction p = 0.027) (Fig. 19 and 20). Both LIBA-8841 and LIBA-8541 induced hemorrhage and inflammatory infiltration at levels comparable to those observed for *C. perfringens*, with no statistically significant differences among groups (Kruskal–Wallis test; hemorrhage, p = 0.061; inflammation, p = 0.733) (Fig 20).

Gram stains of tissue affected by ATCC 3624 showed abundant Gram-positive rods (Fig. 19C). In contrast, skeletal muscle exposed to strains LIBA-8541 and LIBA-8841 tended to display fewer visible Gram-positive rods, mainly in association with inflammatory infiltration; however, these differences were not statistically significant, consistent with the bacterial load analysis (Fig20). Also, abundant purple segments were identified as a sign of bacterial lysis. The negative control, injection of PBS, failed to induce any gross or microscopically changes in the skeletal muscle (Fig. 19).

Sequencing results confirmed the match between the isolates and the corresponding inoculated strains, as well as the genetic differentiation between LIBA-8541 and LIBA-8841. No *C. perfringens* or Cp-like isolates were recovered from tissues injected with sterile DPBS buffer (negative control).

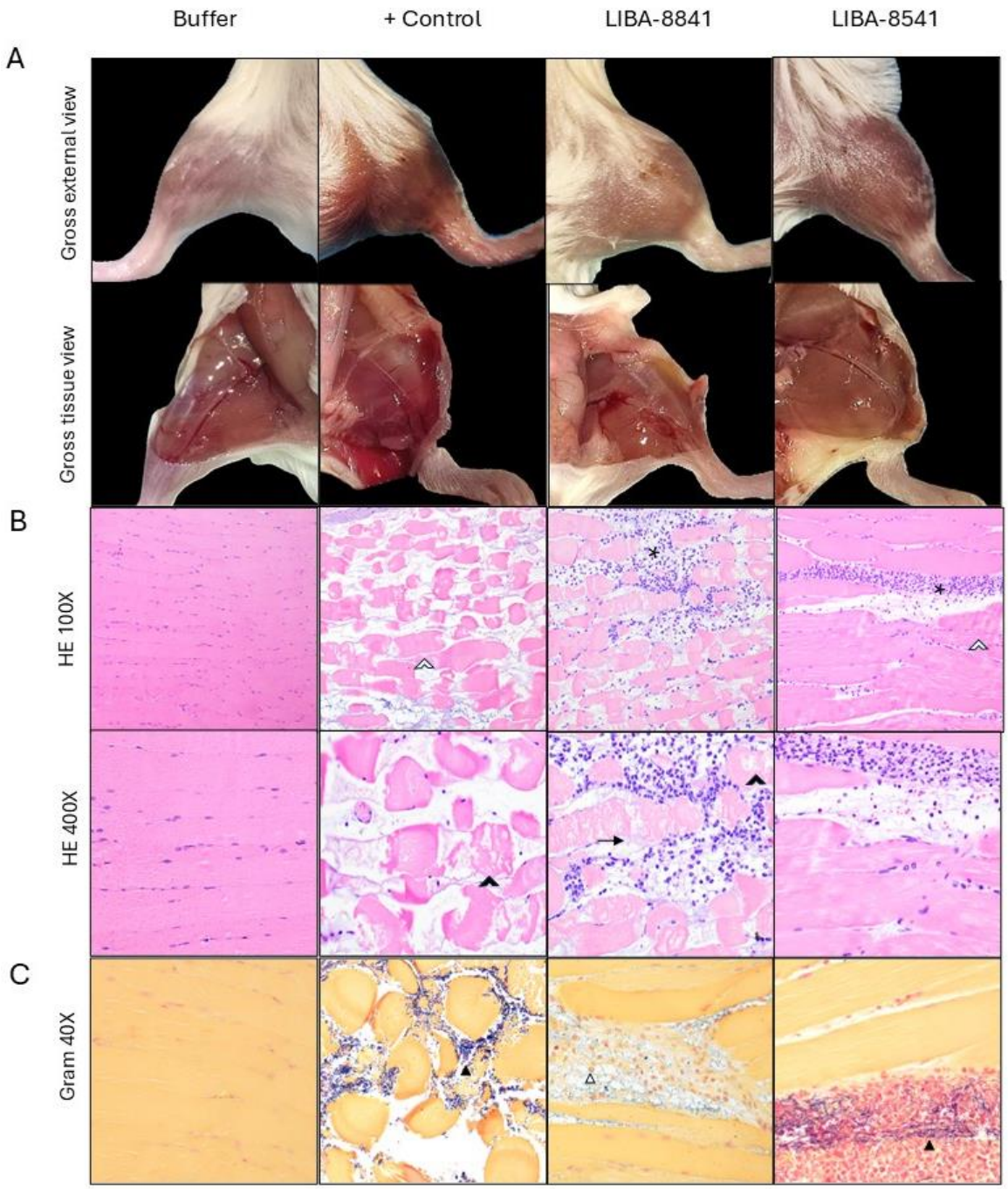

Figure 19. Tissular damage induced by Cp-like strains in a mice model of gas gangrene. Groups of 3 mice were intramuscularly injected with 1 x10^7 CFU of *C. perfringens* strains ATCC 3624 (+ control), strains LIBA-8841 and LIBA-8541, or PBS (- control) and muscle sections were collected 8h after infection. **(A)** Macroscopic pathology. **(B)** Hematoxylin and eosin (H&E)-stained sections show microscopically tissular damage. Myonecrosis is evident by hypercontraction bands (open arrowheads), vacuolation (black arrowheads), edema (arrows). Inflammatory infiltrate (asterisks) is evident in the affected muscle. **(C)** Gram stain sections show Gram- positive rods (black tringle) and purple segments related to bacterial lysis (open tringle). Representative pictures of 3 mice groups are shown.

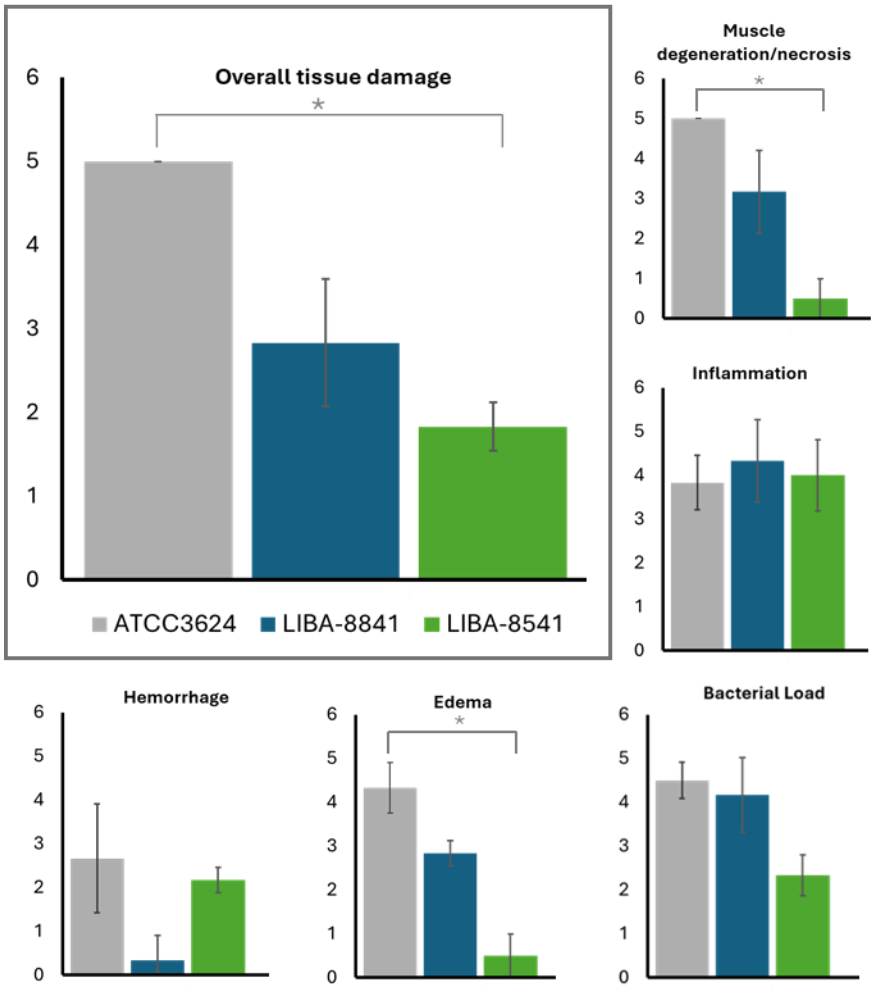

Figure 20. Evaluation of tissular damage induced by Cp-like strains in a mouse model of gas gangrene. Skeletal muscle was collected and evaluated for histopathological alterations, including muscle degeneration (loss of striations, cytoplasmic loss, vacuolation, and hypercontraction bands), inflammation (presence of inflammatory cells), hemorrhage, edema, and bacterial load. Damage was scored on a semi-quantitative scale from 0 to 5. *C.perfringens* ATCC3624 was used as virulence positive control. Bars represent the mean ± standard error of three animals per group (n = 3). Statistical comparisons were performed using the Kruskal–Wallis test followed by Dunn's multiple-comparison post hoc test with Bonferroni correction (* $p < 0.05$).

LIBA-8541 and LIBA-8841 exhibit highly similar PLC-associated phenotypic profiles and pathogenic potential

A comprehensive comparison of the quantitative and qualitative phenotypes evaluated for LIBA-8541 and LIBA-8841 is shown in Table 6. Overall, both Cp-like strains exhibited highly similar functional profiles, with no statistically significant differences between them across the assessed parameters. Their recombinant PLCs showed comparable enzymatic activity and hemolytic potential, and the exoproteomes displayed similar cytotoxicity levels, degrees of antibody neutralization, and relative PLC abundance. Consistent with the *in vitro*

findings, both strains induced comparable tissue damage scores in the murine gas gangrene model. Together, these results indicate that LIBA-8541 and LIBA-8841 share a closely related pathogenic phenotype driven by analogous PLC-associated activities.

Table 6. Comparative summary of *in vitro* and *in vivo* functional analyses of Cp-like strains LIBA-8541 and LIBA-8841.

***In vitro* evaluation of recombinant PLC**	**LIBA-8541**	**LIBA-8841**	***C.perfringens***
PLC activity (mU/mg)	4.756*	8.011	19.908*
Hemolysis potential (%)	32.43*	14.75*	106.65*
Exoproteome analyses			
Cytotoxic potential (% cell killing)	81.14	95.48*	56.75*
Neutralization by anti- Cp-PLC (% cell killing reduction)	20.38	21.44	35,00
Relative abundance of PLC (%)	0.038	0.034	0.057
***In vivo* evaluation in murine gas gangrene model**			
Overall tissue damage (severity scale)	2*	3	5

* indicate significant differences compared with Cp PLC or *C. perfringens* Type A.

2.4 Discussion

Two genetically distinct *Clostridium perfringens*-like isolates (LIBA-8541 and LIBA-8841) previously identified through molecular typing and characterized by the presence of variant phospholipase C (PLC) (25) and other virulence-associated traits were investigated in this study by an integration of phenotypic, proteomic, and *in vivo* analyses. The combined analyses indicate that these isolates are pathogenic and display virulence-associated phenotypes broadly comparable to *C. perfringens*, while some parameters suggest a tendency toward attenuated virulence.

Functional assays confirmed that both PLC variants in the Cp-like strains retain phosphatidylcholine hydrolysis, lecithinase and hemolytic activity despite their divergence at the sequence level. Nonetheless, when compared to a commercial CpPLC, their phospholipase and hemolytic activity profiles or kinetics hint to a slower hydrolysis rate of membrane-phospholipids or reduced substrate accessibility (113). Specifically, hemolytic activity was assessed using human erythrocytes, whose outer membrane is enriched in phosphatidylcholine (PC) and phosphatidylserine (PS). Variations in their relative abundance or membrane

asymmetry may therefore modulate substrate accessibility and influence PLC-mediated lysis (133).

These functional differences are consistent with sequence-based predictions indicating structural divergence in membrane-interaction sites and catalytic domains. In particular, substitutions identified in the PLCs of LIBA-8541 and LIBA-8841 are expected to modulate properties related to calcium dependency and membrane affinity and may be associated with increased Ca^{2+} requirements and a narrower pH range for optimal activity (106–108, 134). Additionally, predicted changes in the hydrophobicity and polarity of the lipid-binding interface may influence membrane interactions, possibly resulting in reduced affinity for phosphatidylcholine-rich bilayers and a relative preference for sphingomyelin (SM)-enriched membranes. This putative phenotype is analogous to that reported for *Paraclostridium bifermentans* PLC, which harbors substitutions in the C-terminal membrane-interaction region (including residues Y331 and adjacent positions) and exhibits selective SM hydrolysis with poor activity on PC-containing substrates such as egg yolk (104, 135, 136). Further studies assessing the activity of these PLC variants on erythrocytes from different species or against defined substrates such as sphingomyelin could help elucidate their true lytic potential. This is particularly relevant given that substrate-specific hydrolysis by bacterial phospholipases generates lipid-derived products such as diacylglycerol (DAG) and ceramide, which can act as secondary messengers in key cellular processes of host cells (137, 138), including stress response, cell cycle regulation, autophagy, and cytokine production (102). Thus, the substrate preference and enzymatic specificity of PLC variants may have broader implications.

Cytotoxicity assays demonstrated that cell-free supernatants induced cytopathic effects and cell death in Don-Q cells. Notably, neutralization assays using a polyclonal anti-PLC antibody derived from *C. perfringens* resulted in only partial protection. This incomplete neutralization suggests that sequence divergence in the variant PLCs compromises antibody neutralization efficiency. Alternatively, and not mutually exclusively, incomplete neutralization could result from suboptimal antibody concentration, limited epitope accessibility, antibody modification or degradation mediated by other exoproteome components (e.g., proteases), or the contribution of additional cytotoxic factors present in the bacterial supernatants. Such

antigenic divergence and functional complexity may have implications for antibody-based detection and therapeutic strategies, potentially limiting cross-reactivity and reducing efficacy.

These observations also underscore the need for a broader examination of the exoproteome to identify additional virulence factors contributing to the observed cytotoxic effects. Consistent with this hypothesis, the proteomic analysis performed revealed marked divergence between Cp-like and *C. perfringens* strains, highlighting metabolic and functional traits potentially linked to their pathogenic profiles. Increasing evidence suggests that such metabolic proteins contribute to pathogenesis or immune evasion by facilitating nutrient acquisition, promoting adhesion, and assisting protein folding under stress conditions (97, 139, 140). Beyond their metabolic roles, enzymes such as acetyl-CoA acetyltransferase, translation elongation factor, and ornithine carbamoyltransferase have been identified as immunogenic components of the *C. perfringens* exoproteome (132). Thus, divergence in these extracellular proteins may influence the repertoire of antigens presented to the host immune system during infection, potentially altering downstream immune activation in ways that directly shape the pathogenesis of gas gangrene.

Although the overall exoproteome profiles of Cp-like strains differ from *C. perfringens* reference strains, they still exhibit key virulence factors commonly associated with this species. Notably, both Cp-like strains secreted SagA and PLC, two major virulence proteins typically regulated by the VirR/VirS two-component system in *C. perfringens* (139). SagA, in addition to its proposed role in host invasion, is also essential for gliding motility (141), a mechanism potentially relevant for tissue dissemination.

However, the relatively low abundance of PLC and other toxins in the exoproteome of Cp-like strains LIBA-8541 and LIBA-8841 suggests that their expression may be distinctly regulated and influenced by undefined culture conditions or growth phases. In this context, differences in toxin abundance, together with possible intrinsic attenuation of enzymatic activity, could partially account for the reduced cytotoxicity observed *in vitro* and the tendency toward lower virulence suggested by the *in vivo* assays. Additional exoproteins detected, including peptidases, 5′-nucleotidases, and invasion-associated enzymes like collagenases and DNases, further support the pathogenic potential of LIBA-8541 and LIBA-8841. Of note, 5′-nucleotidases may contribute to immune evasion by degrading extracellular ATP, a damage-

associated molecular pattern (DAMP) that activates immune cells, thereby suppressing inflammation through a negative feedback mechanism. LIBA-8841 secreted a broader array of factors linked to gas gangrene, such as exodeoxyribonucleases, which may act synergistically with PLC to degrade neutrophil extracellular traps (NETs) (117).

In the murine model, both Cp-like isolates produced clinical signs and histopathological changes compatible with myonecrosis. However, under the experimental conditions used, tissue damage associated with LIBA-8541 and LIBA-8841 tended to be less severe than that observed for the reference *C. perfringens* strain (ATCC 3424) (13). These results indicate that the Cp-like strains are capable of inducing localized colonization and tissue injury *in vivo*, while other pathogenic processes, such as immune modulation remain to be evaluated. Future studies could address the expression of additional virulence-associated genes, such as proteases (e.g., clostripain and endoN-acetylgalactosamindase), hyaluronidase (μ toxin), collagenase, and endoglycosidases, which have been reported to be differentially expressed by *C. perfringens* during infection compared with *in vitro* conditions (99, 142).

Although the pathogenic potential of Cp-like strains was demonstrated through *in vitro* and *in vivo* assays, further structural and biochemical studies, including analyses of pH, temperature, ion concentration, and substrate specificity, are needed to fully elucidate the functional implications of the newly identified PLC variants (137, 138). Preliminary observations suggest cell-type-specific cytotoxicity; thus, future studies should explore host cell death mechanisms such as ROS production, MEK/ERK signaling, and ceramide-mediated responses, as previously described for other bacterial phospholipases C, which could provide deeper insights into host-pathogen interactions (102, 114). The use of isogenic mutants could also clarify the regulation of virulence gene expression during infection and reveal the role of other phenotypic traits, such as gliding motility and adhesion, in host colonization and disease progression (100, 143).

Collectively, this study provides functional and pathological evidence that the Cp-like isolates represent distinct *Clostridium* species capable of reproducing key features of myonecrosis. Their divergent PLC variants, together with the unique exoproteomic profiles observed, highlight adaptive strategies that may modulate virulence potential. These findings broaden current understanding of pathogenic diversity within the *C. perfringens* group and underscore

the importance of exploring emerging clostridial species at the interface of environmental persistence and clinical disease.

LIMITATIONS

Despite the breadth of our findings, several limitations merit acknowledgment. The experimental characterization of the novel *Clostridioides* species was based on culture supernatants rather than purified toxins; therefore, the observed cytopathic and tissue effects cannot be attributed exclusively to toxin activity. Additional virulence determinants, including the binary toxin may contribute to the observed pathology and should be examined individually in future studies using purified toxins or genetically modified strains targeting specific virulence factors or their regulatory elements. The ligated ileal loop model employed to study these bacteria assesses tissue damage rather than the complete infection process. Factors such as colonization efficiency, the presence of metabolically active cells in the intestine, bile acid interactions, and sporulation rates were not explored here but could provide critical insights into the infection dynamics of these new genomospecies, particularly through complementary *in vivo* models, such as the hamster infection model.

As for the *Clostridium*-related species, this study primarily focused on α-toxin, while other virulence factors potentially influencing pathogenesis were not evaluated independently.

Finally, the conclusions presented are derived from a limited number of isolates, five strains representing three of the eight novel *Clostridioides* genomospecies and two isolates from *Clostridium* related species. A broader analysis including a more diverse and representative collection of strains will be necessary to achieve a more comprehensive understanding of the phenotypic variability, pathogenic potential, and evolutionary relationships within these emerging taxa.

CONCLUSIONS

This study provides the first phenotypic and experimental evidence supporting the pathogenic potential of novel *Clostridioides* and *Clostridium* species from human and environmental origin. Through *in vitro* and *in vivo* analyses, these organisms were shown to produce active toxins capable of inducing cytopathic effects, epithelial injury, and tissue damage consistent with the clinical manifestations of *C. difficile* and *C. perfringens* infections.

Comparative analyses between clinical and environmental *Clostridioides* strains revealed important differences in toxin production, cytotoxicity, and histopathological impact, suggesting ecological and evolutionary adaptations that shape virulence. Notably, environmental strains often exhibited comparable or even greater pathogenic effects than their clinical counterparts, underscoring the role of non-clinical reservoirs in maintaining and potentially disseminating toxigenic lineages. These observations highlight the importance of a *One Health* perspective to understand the interconnected dynamics between environment, animals, and humans in the epidemiology of clostridial pathogens.

Additionally, the characterization of *Clostridium perfringens*-like isolates demonstrated that genetically divergent strains retain phenotypic features associated with pathogenicity, supporting their relevance in the context of human disease. These results highlight the importance of considering atypical or previously unclassified *Clostridium* lineages in studies of clostridial infections. Beyond toxin activity, proteomic and phenotypic analyses revealed divergent metabolic and regulatory features that likely modulate virulent expression. The observed variability among isolates indicates that pathogenesis in *Clostridioides* and *Clostridium* is a complex, multifactorial trait that cannot be solely attributed to the presence of canonical toxin genes. Instead, it reflects the interplay between gene regulation, metabolic adaptation, and host–pathogen interactions. These insights emphasize the need for continued genomic and functional studies to elucidate the accessory determinants contributing to virulence variability and host specificity.

Overall, this work contributes to a more comprehensive understanding of the diversity and pathogenic mechanisms of anaerobic spore-forming bacteria. By integrating genomic evidence with experimental infection models, it provides a foundation for refining diagnostic

tools, improving surveillance systems, and informing the development of targeted therapeutic and preventive strategies.

PERSPECTIVES

Future research should expand environmental and clinical sampling to capture the full spectrum of diversity within *Clostridioides* and *Clostridium* species across habitats with varying human and animal influence. As this study includes a limited number of strains from three novel genomospecies, incorporating additional isolates from diverse ecological and clinical sources will be essential to achieve a more comprehensive understanding of their pathogenic potential and epidemiological significance**.**

Particular attention should be given to host-associated factors, such as diet, age, and microbiome composition, that may modulate colonization dynamics and infection outcomes. Given the metabolic adaptations observed in environmental isolates, interactions with the native microbiota are expected to differ from those of classical pathogens, potentially influencing both colonization success and therapeutic response, especially under conditions of antibiotic-induced dysbiosis. Additionally, targeted analyses of individual virulence factors through mutant-based approaches could elucidate their specific contributions to pathogenicity and host adaptation. In parallel, assessing the resistance of spores to environmental stressors and disinfection methods will be essential to identify potential transmission routes and inform prevention strategies.

Collectively, these studies will strengthen a One Health understanding of how environmental and genetic factors drive the emergence and dissemination of pathogenic clostridial species.

TECHNICAL DECLARATIONS

USE OF ARTIFICIAL INTELLIGENCE TOOLS

The writing and editing of this thesis benefited from the assistance of an artificial intelligence language model (ChatGPT 5.1, OpenAI), which was employed exclusively as a tool to support text refinement, improve grammar, enhance clarity, and streamline the presentation of scientific concepts. All scientific content, data interpretation, analyses, and conclusions presented herein are entirely the work and responsibility of the author. The AI tool did not generate original scientific ideas, conduct analyses, or make decisions regarding study design, methodology, or interpretation of results.

FUNDING

This research is framed in the project *"Exploring the virulence of emerging community-acquired human pathogens resembling Clostridioides difficile and Clostridium perfringens",* registered at the Vicerrectoría de Investigación of Universidad de Costa Rica with the code 803-C3-524. It was funded through a International Scientific Research Grant awarded by the Icahn School of Medicine at Mount Sinai, New York (Forgaty International Center, grant D43TW011403).

FACILITIES

The experimental procedures were conducted at the facilities of the Centro de Investigación de Enfermedades Tropicales (CIET), Laboratorio de Investigación en Bacteriología Anaerobia (LIBA), and Instituto Clodomiro Picado (ICP), with technical support provided by personnel with extensive experience in the proposed techniques.
The *in vivo* assays were carried out at the Laboratorio de Ensayos Biológicos (LEBi) with the assistance of specialized technical staff. The murine gas gangrene model was performed in collaboration with Dr. Francisco Uzal at the University of California, Davis (USA). This latter visit was enabled by a grant from SEP.

ETHICS APPROVAL

All animal procedures complied with local legislation (Ley de Bienestar de los Animales N° 7451) and were approved by the Comité Institucional de Cuidado y Uso de Animales (CICUA) of the Universidad de Costa Rica (CICUA-73-2023).

SUPPLEMENTARY MATERIAL

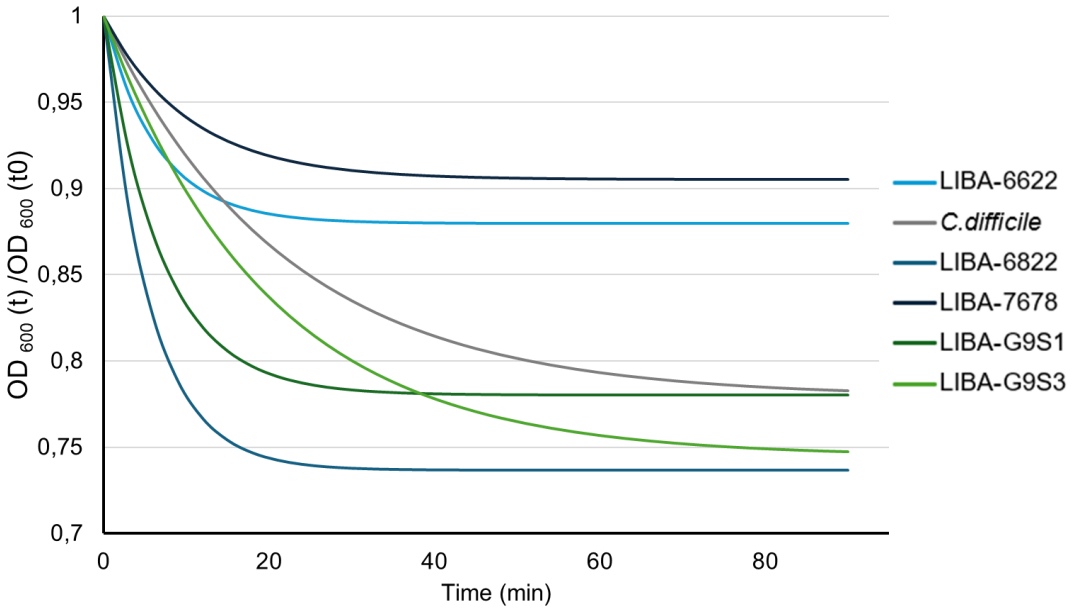

Supplementary Figure 1. Heterogenous germination kinetics of *Clostridioides* strains in the presence of 1% taurocholate. Purified spores were incubated in BHI containing 1% taurocholate, 1 mM glycine, and 50 µM $CaCl_2$ at 37 °C, and germination was monitored by measuring the decrease in OD_{600} over 90 min. *C.difficile* R20291 was used as positive control.

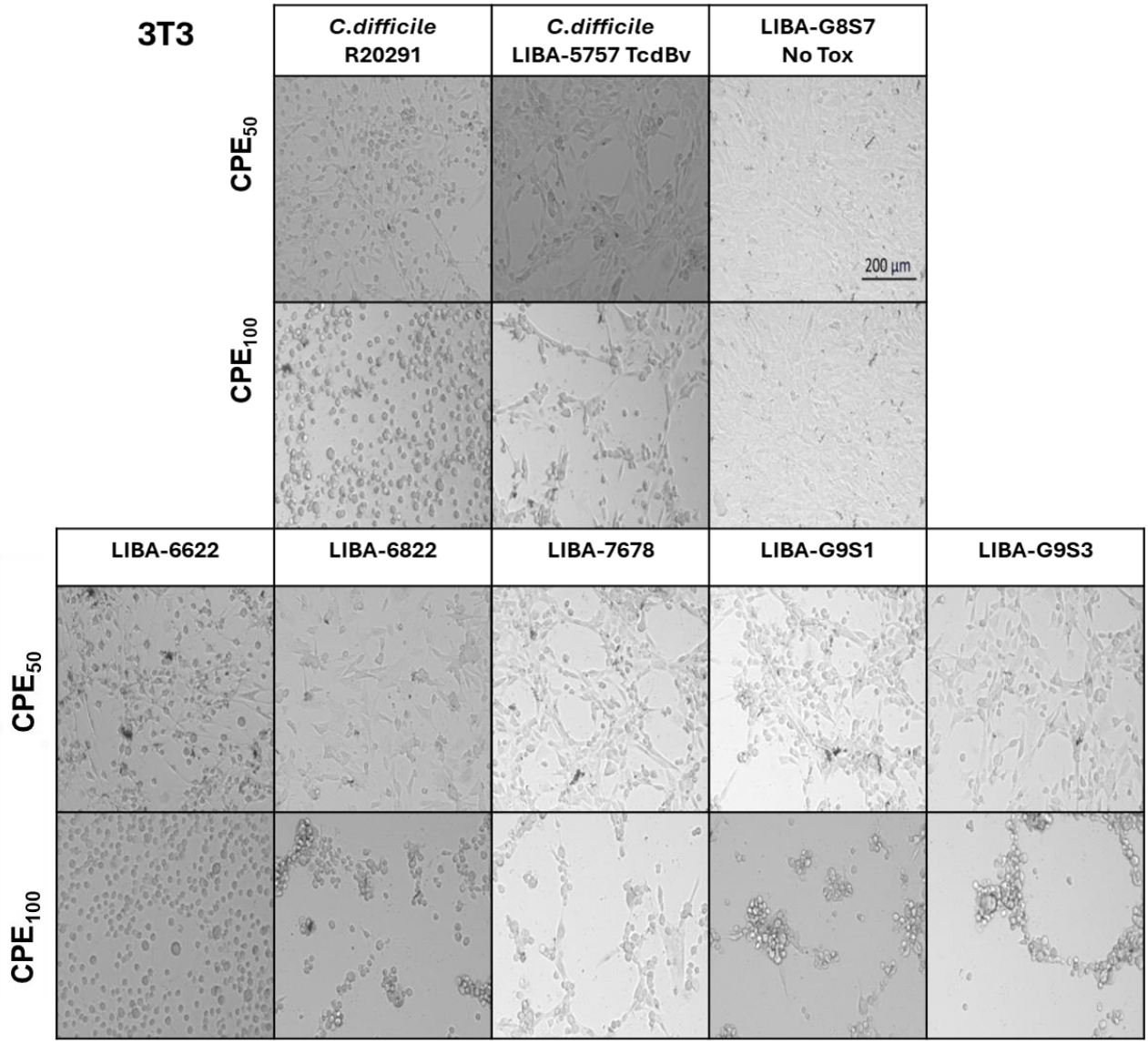

Supplementary Figure 2. Cytopathic phenotypes induced by Cd-like species supernatants in 3T3 cell cultures. Representative phase-contrast micrographs showing cytopathic effects at 50% cell rounding (CPE_{50}) and 100% cell rounding (CPE_{100}) induced by cell-free supernatants in 3T3 fibroblasts exposed to 1:10 diluted cell free supernatants. *C. difficile* R20291 was used as a positive control for classical arborizing CPE mediated by TcdB, whereas a TcdB-variant LIBA-5757 strain induced a distinct filopodia-like morphology. LIBA-G8S7, a non-toxigenic strain, served as a negative control. Scale bar = 200 µm.

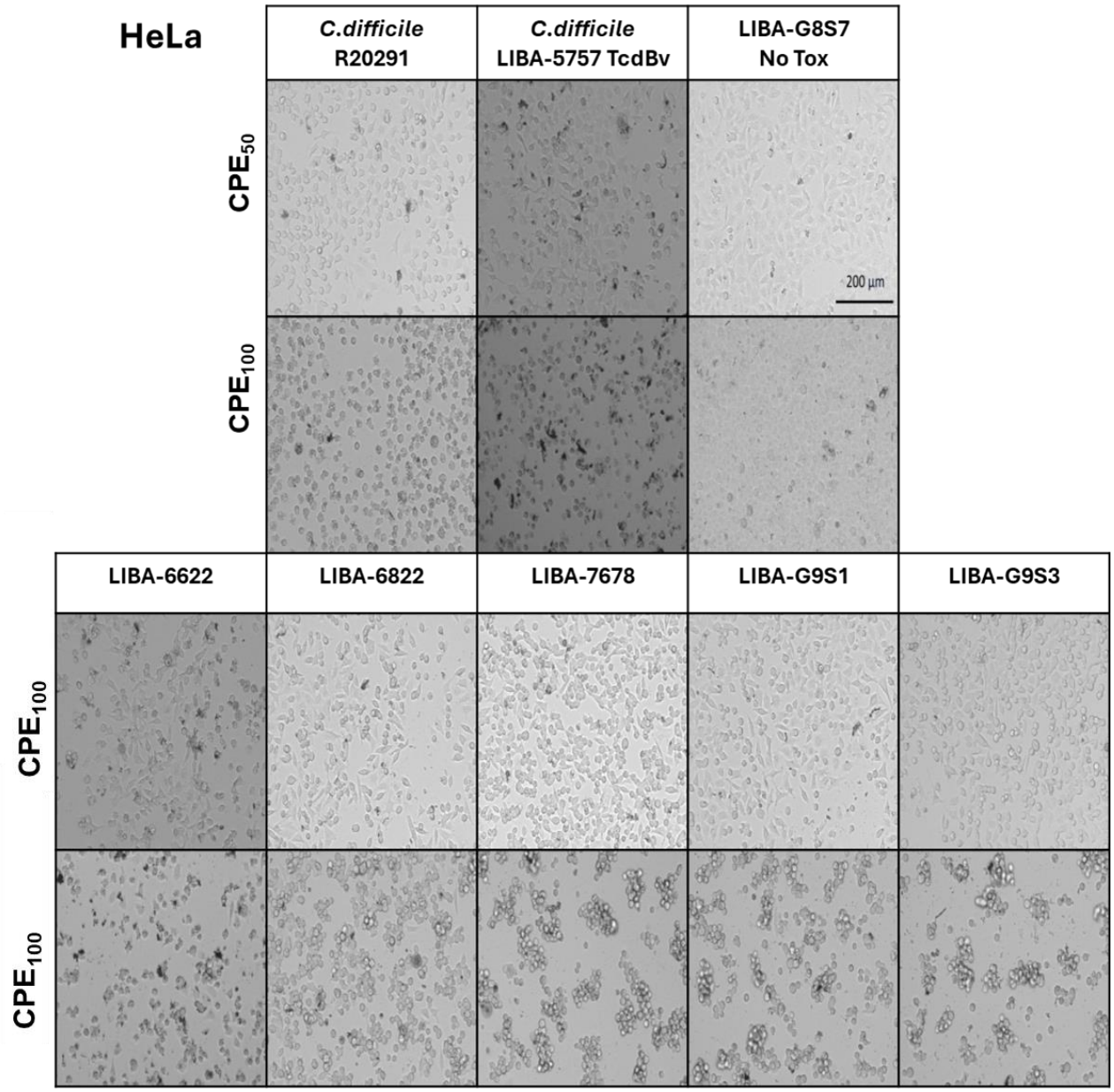

Supplementary Figure 3. Cytopathic phenotypes induced by Cd-like species supernatants in HeLa cell cultures. Representative phase-contrast micrographs showing cytopathic effects at 50% cell rounding (CPE_{50}) and 100% cell rounding (CPE_{100}) induced by cell-free supernatants in HeLa cell cultures exposed to 1:10 diluted cell free supernatants. *C. difficile* R20291 was used as a positive control for classical arborizing CPE mediated by TcdB, whereas a TcdB-variant LIBA-5757 strain induced a distinct filopodia-like morphology. LIBA-G8S7, a non-toxigenic strain, served as a negative control. Scale bar = 200 µm.

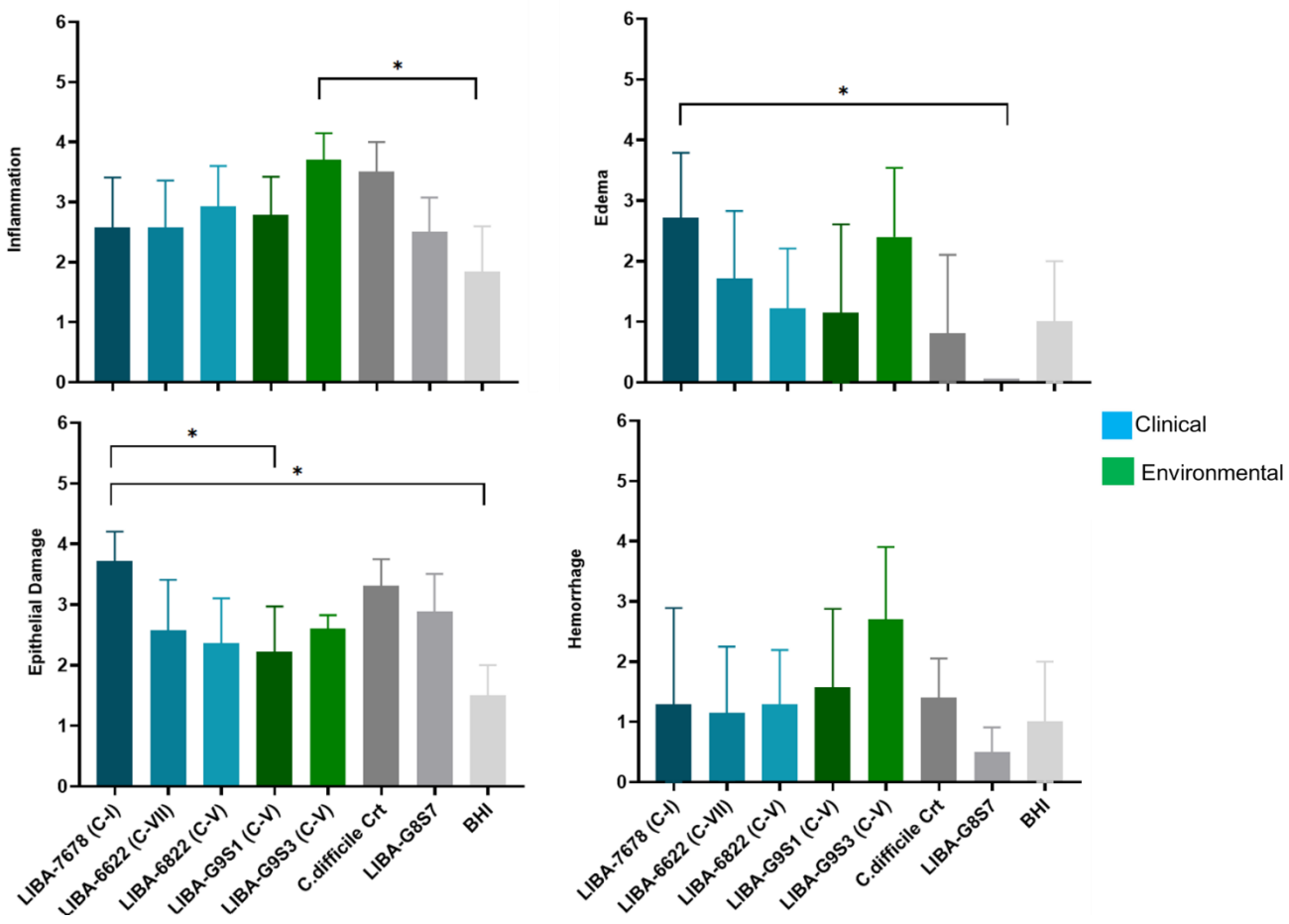

Supplementary Figure 4. Histopathological analysis of ileal tissue response induced by cell-free bacterial supernatants in the murine ligated ileal loop model. Groups of 4–6 mice were inoculated with bacterial supernatants for 4 h, after which tissues were collected, H&E stained, and blindly evaluated. Inflammation, edema, epithelial damage, and hemorrhage were scored on a scale of 0 (no alteration) to 4 (severe alteration). Controls are shown in grey, *C.difficile* R20291 served as positive control, as negative controls the non-toxigenic strain LIBA-G8S7 and BHI (culture medium bacterial free) were included. Data are shown as mean ± SEM. (*) Statistical significance was assessed using the Kruskal–Wallis test followed by Dunn's post hoc multiple-comparison test; $p < 0.05$ was considered statistically significant**.**

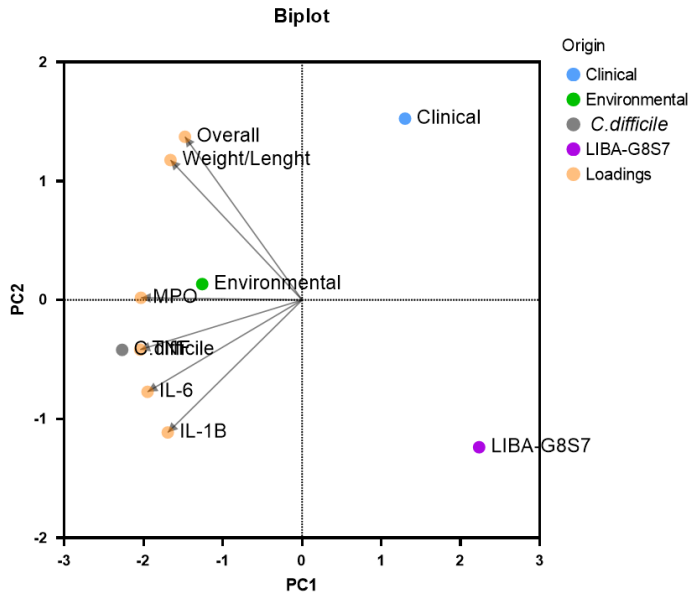

Supplementary Figure 5. Biplot representation of the principal component analysis (PCA) of quantitative and histological markers of intestinal injury induced by *Clostridioides* cell-free supernatants in the murine ileal loop model. PCA was performed using weight/length ratio, MPO activity, cytokine concentrations, and overall histopathological severity scores. Data points represent the mean response of each origin group (clinical, environmental, *C. difficile* R20291, and the non toxigenic Cd-like strain LIBA-G8S7. Vectors indicate the contribution (loadings) of each measured parameter to the variance structure, with PC1 and PC2 together explaining 98% of the total variance (75% and 23%, respectively).

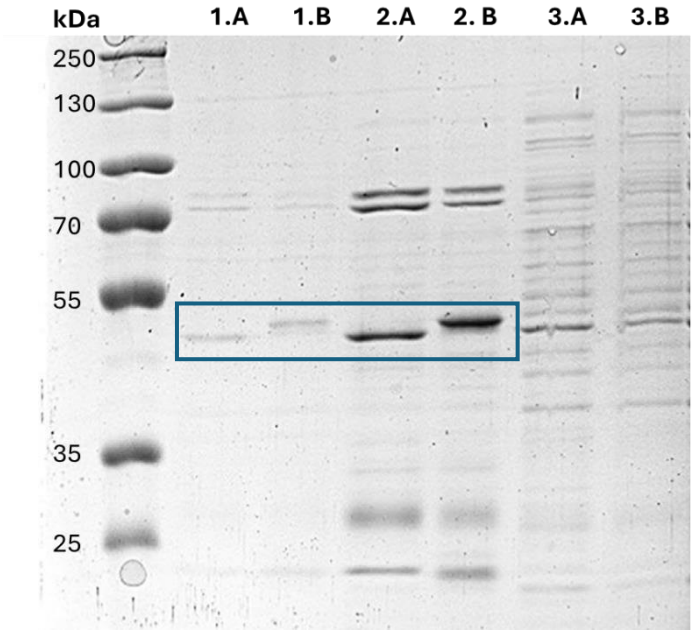

Supplementary Figure 6. SDS-PAGE analysis of recombinant expression and purification of Cp-like PLCs from LIBA-8541 and LIBA-8841 strains in *E. coli*. Samples labeled **A** correspond to the PLC from strain LIBA-8541, and **B** to the PLC from LIBA-8841. **Lane 1**: Second elution fraction; **Lane 2**: First elution fraction; **Lane 3**: Wash fractions. A prominent band near ~43 kDa is visible in the elution fractions (2.A and 2.B), indicating successful expression and purification of the recombinant proteins.

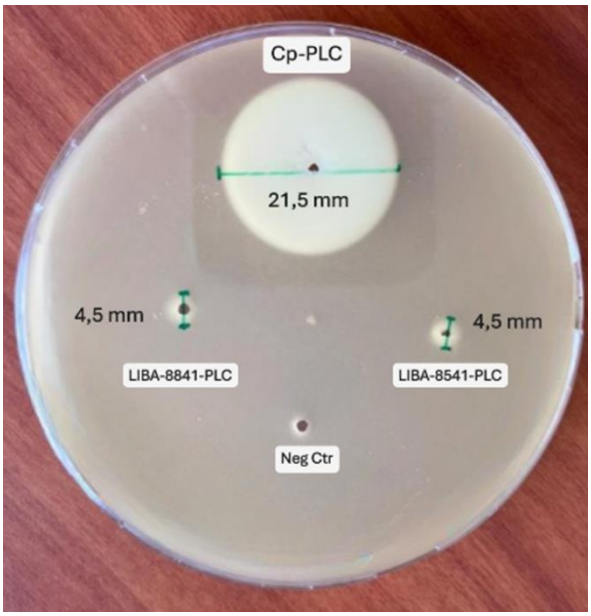

Supplementary Figure 7. Lecithinase activity of recombinant phospholipase C (PLC) enzymes purified from Cp-like strains. Egg yolk agar plates (LB supplemented with 5% egg yolk and ampicillin) were inoculated with purified recombinant PLC proteins. Both LIBA-8841-PLC and LIBA-8541-PLC produced opaque halos of approximately 4.5 mm in diameter, indicating lecithin hydrolysis. In contrast, the reference *C. perfringens* PLC (Cp-PLC) generated a markedly larger halo (21.5 mm). As a negative control, products of washing steps from the purification protocol were tested and showed no lecithinase activity (Neg Ctr).

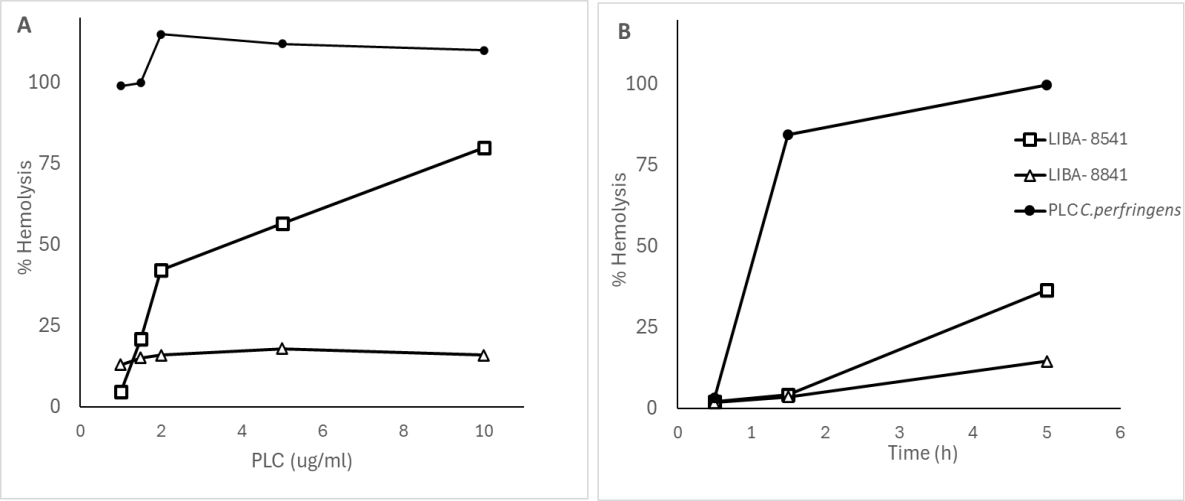

Supplementary Figure 8. Dose- and time-dependent hemolytic activity of recombinant PLCs from Cp-like strains LIBA-8541 and LIBA-8841, and *C. perfringens*. A. Human erythrocytes were incubated at 37 °C for 20 min with increasing concentrations (0–10 µg/ml) of recombinant PLC. Samples were then chilled at 4 °C for 10 min and maintained at room temperature for hemolysis measurements 5h later**. B.** A fixed concentration of 2 µg/ml PLC was used to evaluate hemolytic activity over time (1 h, 1.5 h, and 5 h) under the same conditions. PLC from *C. perfringens* served as a positive control. Results are expressed as percentage hemolysis. Values represent the mean of two independent experiments with reproducible trends; due to the limited number of replicates, no statistical test was applied.

Supplementary Table 1. Proteins identified in the cell-free supernatant of Cp-like strain LIBA-8841

Proteins with a relative abundance ≥ 0.174% (75th percentile) are listed

Accession	Anticipated function	Mean Coverage (%)	Avg.Mass (Da)	Relative Abundance (%)	Str.Desv(%)
AGCDLC_00605	type I glyceraldehyde-3-phosphate dehydrogenase	48	35362	23,8122	33,5206
COAOJB_04550	Chaperone protein DnaK	45	66883	15,1740	11,5471
COAOJB_00620	Glyceraldehyde-3-phosphate dehydrogenase	55	35675	7,6106	2,8212
AGCDLC_16030	Rubrerythrin	41	19979	3,4304	2,5596
AGCDLC_00595	triose-phosphate isomerase	56	27056	3,1845	1,3178
AGCDLC_00010	Fe-S cluster assembly scaffold protein IscU NifU family	48	24855	3,0846	1,2489
AGCDLC_13390	elongation factor G	28	76050	2,9576	-
AGCDLC_12795	3-hydroxyacyl-CoA dehydrogenase	31	30466	2,7545	1,9058
AGCDLC_00005	GGGtGRT protein	40	35479	2,6432	1,8943
AGCDLC_12640	glucose-6-phosphate isomerase	27	49782	2,4497	0,5523
AGCDLC_00555	phosphopyruvate hydratase	32	46976	2,2648	1,1258
AGCDLC_12810	Acyl-CoA dehydrogenase related to the alkylation response protein AidB	32	41010	2,0895	2,6401
COAOJB_04680	Glutamate decarboxylase beta	45	53117	2,0817	0,0770
COAOJB_04700	Pyruvate:ferredoxin oxidoreductase	20	128508	1,9067	2,5378
AGCDLC_00600	Phosphoglycerate kinase	33	42692	1,8968	1,2871
COAOJB_16270	Heme oxygenase	50	25208	1,7245	1,7268
AGCDLC_05290	Acetyl-CoA acetyltransferase	39	40782	1,7161	1,4709
AGCDLC_02510	HPr or related phosphotransfer protein	77	9094	1,5940	1,3619
AGCDLC_10290	6-phosphofructokinase	34	36415	1,3813	0,4515
AGCDLC_13290	30S ribosomal protein S5	42	17302	1,3069	1,2094
AGCDLC_00835	class II fructose-1 6-bisphosphate aldolase	25	30375	1,2292	0,7205
AGCDLC_10880	Succinyl-diaminopimelate desuccinylase	23	51415	1,1064	0,4156
AGCDLC_05805	Cytochrome C551	25	5987	1,0153	0,9388
AGCDLC_10715	SagA protein	24	47506	1,0115	1,2207
AGCDLC_13420	50S ribosomal protein L7/L12	51	12622	0,8635	0,7031
AGCDLC_02735	30S ribosomal protein S16	58	9098	0,8074	0,3398
COAOJB_11025	Glutaminase 1	45	34063	0,7968	0,8352
AGCDLC_12815	Enoyl-CoA hydratase/carnithine racemase	29	28177	0,7801	0,8560
AGCDLC_04495	30S ribosomal protein S20	21	9500	0,7755	-
AGCDLC_02670	translation elongation factor Ts	22	33230	0,7514	0,3274
AGCDLC_16165	Phosphotransferase system IIA component	33	16975	0,7163	0,6505
AGCDLC_11965	Enamine deaminase RidA house cleaning of reactive enamine intermediates YjgF/YER057c/UK114 family	26	13708	0,6986	0,5914
AGCDLC_12755	chaperonin GroEL	31	57535	0,6899	0,4336
WP_011590118.1	NlpC/P60 family protein	21	46946	0,6532	0,5092
AGCDLC_15940	50S ribosomal protein L9	41	16423	0,6346	0,2587
WP_003455061.1	glutamate decarboxylase	24	52940	0,5479	0,7748
AGCDLC_13125	thioredoxin	48	11526	0,5429	0,5040
AGCDLC_13270	adenylate kinase	24	24098	0,5425	0,5576
WP_011590766.1	C40 family peptidase	23	59140	0,5081	-
AGCDLC_13090	phosphate butyryltransferase	38	32334	0,5041	0,3943
COAOJB_11345	hypothetical protein	41	5440	0,5014	0,1318
COAOJB_15630	Rubrerythrin	28	22256	0,4918	0,3743
AGCDLC_04595	flavodoxin	18	15652	0,4335	0,2629
AGCDLC_13335	50S ribosomal protein L29	54	8134	0,4047	-
COAOJB_11895	YtxH domain-containing protein	46	15113	0,3992	-
AGCDLC_11525	Choloylglycine hydrolase	22	36857	0,3927	0,3373
AGCDLC_09735	L-threonine dehydrogenase	24	41367	0,3891	-
AGCDLC_13280	50S ribosomal protein L15	25	15549	0,3754	0,4039
AGCDLC_07805	HTH domain protein	49	6691	0,3741	0,3859
COAOJB_09200	hypothetical protein	53	15920	0,3606	-
AGCDLC_13225	50S ribosomal protein L17	35	12847	0,3529	0,0358
AGCDLC_13135	Phosphoenolpyruvate-protein kinase (PTS system EI component in bacteria)	13	59527	0,3500	0,0489
AGCDLC_04375	30S ribosomal protein S21	34	7016	0,3400	0,3696
AGCDLC_04455	Protein GrpE	24	24324	0,3350	0,1297
AGCDLC_13355	30S ribosomal protein S19	52	10640	0,3149	0,0374
AGCDLC_03880	Serine hydroxymethyltransferase	8	45260	0,3085	0,4354
AGCDLC_12680	glutamine-hydrolyzing GMP synthase	16	57058	0,2921	0,2470
AGCDLC_09125	Iron-only hydrogenase system regulator	28	9083	0,2806	0,1248
COAOJB_15400	Phage major capsid protein	39	10346	0,2790	0,1310
AGCDLC_13905	Xaa-Pro aminopeptidase	16	40453	0,2780	0,3932
AGCDLC_10780	Peptidyl-prolyl isomerase parvulin family	21	28003	0,2657	0,3611
AGCDLC_03090	Fe-S cluster assembly scaffold protein NifU	31	15833	0,2645	0,2639
AGCDLC_13550	thioredoxin-disulfide reductase	11	34412	0,2522	0,1144
AGCDLC_04900	50S ribosomal protein L27	29	10853	0,2486	0,0833
WP_011590151.1	pyruvate kinase	16	49485	0,2409	0,1664
AGCDLC_13715	transcription elongation factor GreA	35	17687	0,2377	0,2010
AGCDLC_14490	Preprotein translocase subunit SecA (ATPase RNA helicase)	16	19403	0,2375	0,1796
AGCDLC_15685	peptidase T	13	44898	0,2308	0,2157
AGCDLC_12030	glutamate--tRNA ligase	9	63689	0,2228	0,1924
AGCDLC_13435	50S ribosomal protein L11	33	14861	0,2183	0,1623
COAOJB_08130	hypothetical protein	25	16875	0,2155	0,2636
AGCDLC_03685	50S ribosomal protein L35	17	7455	0,2146	0,2329
AGCDLC_02660	ribosome recycling factor	26	20892	0,2117	0,1989
AGCDLC_10890	AlaDh-PNT-N domain-containing protein	26	12598	0,2080	0,0948
AGCDLC_13350	50S ribosomal protein L22	58	12385	0,2045	0,1841
AGCDLC_05335	50S ribosomal protein L31	34	7721	0,2025	0,0430
WP_003453100.1	alkyl hydroperoxide reductase subunit C	32	20910	0,1998	-
AGCDLC_13375	50S ribosomal protein L3	11	22673	0,1889	0,3054
WP_003458341.1	biliverdin-producing heme oxygenase	30	24874	0,1862	0,2620
AGCDLC_02795	phosphate acetyltransferase	17	35651	0,1801	0,1352
COAOJB_02615	Adenylosuccinate lyase	7	58316	0,1789	0,2371

Supplementary Table 2. Proteins identified in the cell-free supernatant of Cp-like strain LIBA-8541

Proteins with a relative abundance ≥ 0.163% (75th percentile) are listed

Accession	Anticipated function	Mean Coverage (%)	Avg.Mass (Da)	RelativeAbundance (%)	Str.Desv(%)
AGCDLC_00605	type I glyceraldehyde-3-phosphate dehydrogenase	62	35362	27,0776	14,6894
COAOJB_04550	Chaperone protein DnaK	37	66883	10,8620	3,0344
AGCDLC_12795	3-hydroxyacyl-CoA dehydrogenase	45	30466	6,5996	1,9876
AGCDLC_05290	Acetyl-CoA acetyltransferase	65	40782	5,3019	2,8736
AGCDLC_12810	Acyl-CoA dehydrogenase related to the alkylation response protein AidB	46	41010	4,2856	2,6161
AGCDLC_00595	triose-phosphate isomerase	71	27056	3,4693	2,0767
AGCDLC_16030	Rubrerythrin	37	19979	3,3822	3,4958
AGCDLC_00005	GGGtGRT protein	44	35479	2,9082	1,1349
AGCDLC_12640	glucose-6-phosphate isomerase	39	49782	2,7432	0,3022
AGCDLC_12815	Enoyl-CoA hydratase/carnithine racemase	54	28177	2,5275	1,0793
AGCDLC_10715	SagA protein	36	47506	2,1610	2,1082
AGCDLC_00010	Fe-S cluster assembly scaffold protein IscU NifU family	47	24855	1,8954	0,4968
AGCDLC_12755	chaperonin GroEL	47	57535	1,8573	0,8259
AGCDLC_10290	6-phosphofructokinase	42	36415	1,7652	0,3092
AGCDLC_00835	class II fructose-1 6-bisphosphate aldolase	21	30375	1,4874	1,4714
AGCDLC_13290	30S ribosomal protein S5	63	17302	1,2286	0,2333
AGCDLC_13135	Phosphoenolpyruvate-protein kinase (PTS system EI component in bacteria)	25	59527	1,1086	0,0912
AGCDLC_02510	HPr or related phosphotransfer protein	75	9094	0,9964	0,8943
AGCDLC_12680	glutamine-hydrolyzing GMP synthase	27	57058	0,9198	0,5899
AGCDLC_05805	Cytochrome C551	38	5987	0,8850	1,0028
AGCDLC_15685	peptidase T	35	44898	0,7659	0,2384
AGCDLC_15910	30S ribosomal protein S6	37	11030	0,5907	0,8584
AGCDLC_15940	50S ribosomal protein L9	51	16423	0,5105	0,3210
AGCDLC_04575	glutamate decarboxylase	21	53756	0,4832	0,4491
AGCDLC_06030	Phosphoribosylformylglycinamidine cyclo-ligase	24	36240	0,3806	-
AGCDLC_09250	Ferredoxin--nitrite reductase	25	57852	0,3761	0,2037
AGCDLC_13435	50S ribosomal protein L11	23	14861	0,3650	0,5115
AGCDLC_11985	aminopeptidase	25	51672	0,3645	0,2355
AGCDLC_09860	hypothetical protein	25	64784	0,3597	0,1756
AGCDLC_15815	50S ribosomal protein L34	18	5492	0,3573	-
AGCDLC_13420	50S ribosomal protein L7/L12	36	12622	0,3497	0,4472
AGCDLC_01080	purine-nucleoside phosphorylase	23	25635	0,3292	0,2604
AGCDLC_10880	Succinyl-diaminopimelate desuccinylase	27	51415	0,3188	0,2096
AGCDLC_11350	orotidine-5'-phosphate decarboxylase	26	31718	0,3175	0,2830
AGCDLC_13295	50S ribosomal protein L18	32	13299	0,3032	0,1111
AGCDLC_13125	thioredoxin	46	11526	0,3007	0,2248
AGCDLC_11525	Choloylglycine hydrolase	30	36857	0,2996	0,1849
AGCDLC_03880	Serine hydroxymethyltransferase	11	45260	0,2955	0,1188
AGCDLC_10780	Peptidyl-prolyl isomerase parvulin family	31	28003	0,2916	0,2434
AGCDLC_11965	Enamine deaminase RidA house cleaning of reactive enamine intermediates YjgF/YER057c/UK114 family	33	13708	0,2826	0,3927
COAOJB_04700	Pyruvate:ferredoxin oxidoreductase	12	128508	0,2784	0,3179
AGCDLC_03090	Fe-S cluster assembly scaffold protein NifU	38	15833	0,2761	0,2961
AGCDLC_04375	30S ribosomal protein S21	36	7016	0,2729	-
AGCDLC_06015	Phosphoribosylcarboxyaminoimidazole (NCAIR) mutase	20	17202	0,2671	-
AGCDLC_13270	adenylate kinase	27	24098	0,2615	0,2935
AGCDLC_03685	50S ribosomal protein L35	34	7455	0,2378	0,2423
AGCDLC_13355	30S ribosomal protein S19	39	10640	0,2240	0,2961
AGCDLC_04240	Leucyl aminopeptidase (aminopeptidase T)	19	46053	0,2227	0,1638
AGCDLC_13360	50S ribosomal protein L2	28	30365	0,2195	0,2976
AGCDLC_14090	Xaa-Pro aminopeptidase	26	47719	0,2170	0,1576
AGCDLC_04545	deoxyribose-phosphate aldolase	23	23884	0,2166	0,2903
AGCDLC_13550	thioredoxin-disulfide reductase	14	34412	0,2114	0,1266
AGCDLC_05305	ribose 5-phosphate isomerase B	17	15955	0,2089	0,2449
AGCDLC_13335	50S ribosomal protein L29	50	8134	0,2078	0,1854
AGCDLC_04910	50S ribosomal protein L21	43	11461	0,2038	-
AGCDLC_14805	Rubrerythrin	21	22170	0,1979	0,1714
AGCDLC_00600	Phosphoglycerate kinase	18	42692	0,1959	0,1714
AGCDLC_14490	Preprotein translocase subunit SecA (ATPase RNA helicase)	15	19403	0,1885	0,1726
COAOJB_00870	NlpC/P60 family protein	7	65676	0,1885	0,0453
AGCDLC_02735	30S ribosomal protein S16	19	9098	0,1878	0,2279
AGCDLC_13280	50S ribosomal protein L15	20	15549	0,1746	0,0770
AGCDLC_12685	IMP dehydrogenase	17	52095	0,1735	0,1389
AGCDLC_14265	Peptidyl-prolyl cis-trans isomerase (rotamase) - cyclophilin family	42	18902	0,1715	0,1891
AGCDLC_13090	phosphate butyryltransferase	30	32334	0,1713	0,1488
COAOJB_04095	2' 3'-cyclic-nucleotide 2'-phosphodiesterase	4	128835	0,1709	-
AGCDLC_09910	molecular chaperone HtpG	15	72421	0,1640	0,1062
AGCDLC_07490	Leucyl aminopeptidase (aminopeptidase T)	17	42201	0,1631	0,1612

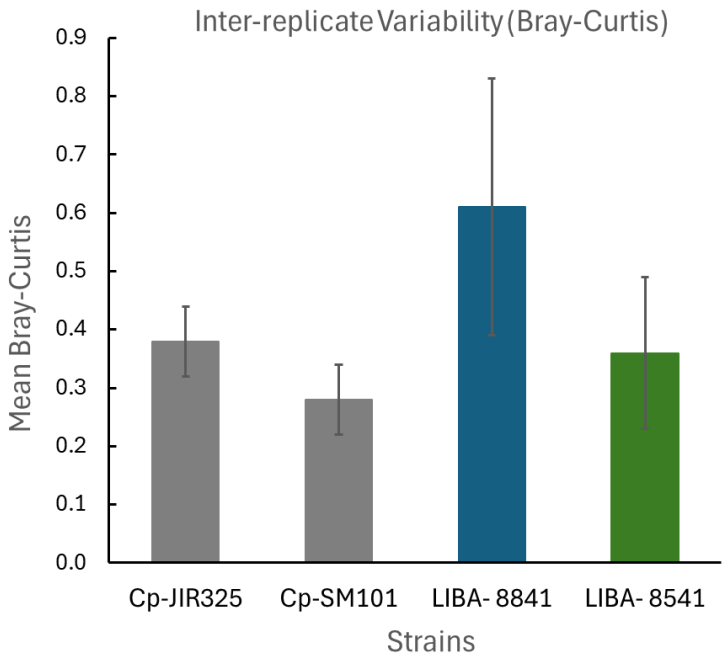

Supplementary Figure 9. Intra-strain variability of exoproteome profiles among biological replicates of the *C. perfringens*-like strains. Mean dissimilarity values (±SD) were calculated for each strain based on pairwise comparisons of replicate exoproteome abundance profiles using the Bray–Curtis dissimilarity index. Statistical analysis with the Kruskal–Wallis test indicated no significant differences in within-strain variability ($H = 3.82$, $p = 0.282$).

Supplementary Table 3. Proteins contributing to NMDS separation between *C.perfringens* reference strains (Cp SM101, Cp JIR325) and Cp-like LIBA-8541 and LIBA-8841

Accesion	Description	COG (functional category)	NMSD axis	Relative Abundance (%)			
				LIBA-8841	LIBA-8541	Cp SM101	Cp JIR325
WP_011590151.1	pyruvate kinase	C o G	1	-	0.15314441	-	-
AGCDLC_13065	Maltose-binding periplasmic protein MalE	G	1	0.0401909	0.01225821	0.08334469	0.11669067
AGCDLC_01785	Lipoprotein	S	1	-	-	0.03759991	0.05977085
AGCDLC_01275	Uroporphyrinogen-III synthase	O	1	-	-	0.01134919	0.01847519
WP_003457081.1	pectate lyase-like adhesive domain-containing protein	S	1	-	-	0.00938319	-
AGCDLC_14915	ornithine carbamoyltransferase	E	1	0.00837812	-	1.77321329	-
AGCDLC_01295	sulfite reductase subunit C	P	1	-	-	0.00239929	0.00324206
AGCDLC_16040	Acyl-ACP thioesterase	I	1	-	-	0.00607673	-
WP_003467108.1	Fe-Mn family superoxide dismutase	P	1	-	-	0.03800369	-
AGCDLC_11360	dihydroorotate dehydrogenase	F	1	-	-	0.01046145	0.02113671
AGCDLC_12970	Oligoendopeptidase F	E	2	-	0.08943437	0.06439197	0.04212901
AGCDLC_12000	UPF0291 protein CPF_1260	S	2	0.02543589	-	-	0.00105677
AGCDLC_00595	triose-phosphate isomerase	G	2	3.1844922	3.46929198	3.3805353	3.13175683
AGCDLC_12310	Glutathione peroxidase	V, I	2	0.09662333	-	-	0.01588471
AGCDLC_04455	Protein GrpE	O	2	0.33497598	0.03600773	0.03557652	0.06490921
AGCDLC_09250	Ferredoxin--nitrite reductase	P, Q	2	0.14861707	0.37611095	0.29297089	0.28118242
COAOJB_11270	Polyamine aminopropyltransferase	E	2	0.02075137	-	-	-
AGCDLC_12475	Propanediol dehydratase large subunit	Q	2	0.10957499	0.0247898	0.02234092	0.0330906
COAOJB_01285	Delta-aminolevulinic acid dehydratase	H	2	0.02606903	0.11426381	0.11610434	-
WP_172678790.1	glutamate-1-semialdehyde 2 1-aminomutase	H	2	-	0.11789195	-	-

APPENDIX

Appendix 1. Protein Quantification Assay

Protein concentration was determined using the Bio-Rad DC™ colorimetric assay according to the manufacturer's instructions. Briefly, 5 µL of each sample or its corresponding dilution was pipetted in duplicate into the wells of a 96-well microplate. Then, 25 µL of Reagent A (prepared by mixing 20 µL of Reagent S per mL of Reagent A) and 200 µL of Reagent B were added to each well. The plate was incubated for 15 minutes at room temperature to allow color development, and absorbance was measured at 690 nm using a Synergy HT microplate reader (BioTek). Protein concentrations were calculated from a calibration curve generated with bovine serum albumin (BSA) standards.

Appendix 2. SDS-PAGE Analysis

Precast 4–15% polyacrylamide Mini-PROTEAN® (Bio-Rad) gels were used for SDS-PAGE analysis. Samples were mixed with 10 µL of Laemmli sample buffer (60 mM Tris-Cl pH 6.8, 2% SDS, 10% glycerol, 5% β-mercaptoethanol, 0.01% bromophenol blue). PageRuler Plus Prestained Protein Ladder ™ (Thermo Scientific) was used as the molecular weight marker. Electrophoresis was carried out at 150 V for 1 hour.

Following electrophoresis, gels were stained with Coomassie Brilliant Blue R-250 solution prepared with 275 mL of deionized water, 500 mL of methanol, 100 mL of glacial acetic acid, and 125 mL of 0.125% Coomassie Brilliant Blue R-250 (in 50% methanol, 10% acetic acid). Protein bands were visualized using a ChemiDoc™ imaging system (Bio-Rad®).

Appendix 3. Western Blot Protocol

Membrane preparation. Proteins were separated on 10% SDS-PAGE gels and run for 1 h at 150 V using 1× running buffer (75 g glycine, 17.5 g Tris-base, and 7.5 g SDS) and a molecular weight marker. Following electrophoresis, proteins were transferred onto PVDF membranes. Prior to transfer, membranes were activated by immersion in methanol for 10 s, and both membranes and transfer materials (sponges and filter paper) were equilibrated in transfer buffer (17.4 g Tris-base, 8.7 g glycine, 600 mL methanol, adjusted to 3 L with distilled water and stored at 4 °C). Transfer was carried out in a cassette assembled in the following order: sponge, filter paper, membrane, gel, filter paper, and sponge. Proteins were

transferred for 1 h at 100 V under constant stirring with an ice block to maintain low temperature.

Immunodetection. Membranes were blocked for 30 min with 5% (w/v) skim milk in PBS-Tween. Primary antibodies were diluted 1:250 in PBS-Tween containing 5% skim milk and applied at a volume of 40 µL/cm² of membrane. Membranes were incubated for 1 h at room temperature with gentle agitation, followed by three washes of 15 min each in PBS-Tween. HRP-conjugated secondary antibodies were diluted 1:750 in PBS-Tween with 5% skim milk, incubated with the membranes for 1 h at room temperature with agitation, and washed three times for 15 min each with PBS-Tween. Signal development was performed by incubating the membranes with chemiluminescent reagent (Roche) for 5 min at a volume of 20 µL/cm², and protein bands were visualized using the ChemiDoc™ Imaging System (Bio-Rad®).

Appendix 4. Murine Ileal loop model

Four- to five-week-old male Hsd:ICR mice, weighing 18–25 g, were used. Animals were grouped in polycarbonate cages and maintained at room temperature. Mice were fasted overnight and then anesthetized with ketamine (60 mg/kg) and xylazine (5 mg/kg). Through a midline laparotomy, a 4-cm ileal loop was ligated and injected with 0.1 mL of bacterial cell-free supernatants or control solutions (saline or BHI broth). The intestinal segment was then returned to the abdominal cavity, the incision was sutured, and mice were allowed to recover from anesthesia. Four hours after inoculation, mice were euthanized, and the loops were collected for the corresponding measurements (40, 61).

Appendix 5. Myeloperoxidase (MPO) activity assay

Myeloperoxidase (MPO) activity was determined using tissue homogenates from ileal loop sections. Reagents were prepared as follows: potassium phosphate buffer (0.01% [w/v] K_2HPO_4 and 0.67% [w/v] KH_2PO_4), hexadecyltrimethylammonium bromide (HTAB) buffer (5 g of HTAB in 1 L of potassium phosphate buffer, adjusted to pH 6.0), O-dianisidine solution (10 mg of O-dianisidine dissolved in 6 mL of potassium phosphate buffer), and substrate solution (30 µL of 1% H_2O_2 diluted in 54 mL of distilled water and mixed with the complete O-dianisidine solution [6 mL]). The substrate solution was stored at 4 °C protected from light until use.

Ileal loop sections of known mass were stored in HTAB buffer at –80 °C, then homogenized in HTAB buffer at a ratio of 1 mL per 56 mg of tissue. Homogenates were centrifuged at 5000 rpm for 5 min, and 10 µL of the resulting supernatant were dispensed in duplicate into 96-well ELISA plates. Potassium phosphate buffer (10 µL) was used as blank. Subsequently, 200 µL of substrate solution was added to each well, and absorbance was measured at 450 nm at 0, 1, and 2 min. MPO activity was expressed as units (U) of MPO per mg of tissue (40).

Appendix 6. Parameters and scoring scale applied in histopathological analysis of murine ileal loops

Sample ID	Inflammation	Score
	Extent	
Severity Score Mild 1 Moderate 2 Marked 3 Severe/diffuse 4	mucosa and submucosa	
	mucosa and submucosa	
	mucosa and submucosa, sometimes transmural	
	transmural	
	Intestinal architecture	
	Epithelial changes and mucosal architecture	
	Hyperplasia: hyperplasia and goblet cell loss	
	Villi: broadening and blunting of the villi up to complete loss of villous. Disorganized, atrophied, or broken villi.	
	Crypts: Irregular crypts with variable diameters along the depth of single crypts or dilated crypts , crypts that did not run parallel, bifurcation at the base of the crypt that might extend to branched crypts, to a mucosa completely devoid of crypts	
	Ulcerations, erosion	
	Desquamation epithelium	
	Edema	
	Congestion/edema	
	Hemorrhage	
	OVERALL	

Appendix 7. Composition of Reinforced Clostridial Medium

Component	g /L
Yeast extract	3
Meat extract	10
Peptone	10
Glucose	5
Soluble starch	1
Sodium chloride	5
Sodium acetate	3
Cysteine hydrochloride	0.5

Appendix 8. **Murine Gas gangrene model**

Three BALB/c mice weighing 20–25 g were used per treatment group. Animals were housed in polycarbonate cages under controlled temperature and light conditions with ad libitum access to food and water.

For bacterial inoculum preparation, cultures of *Clostridium* perfringens and Cp-like strains (LIBA-8541 and LIBA-8841) were initiated by transferring 0.4 mL of overnight cultures grown in fluid thioglycolate medium (FTG; Difco Laboratories) into 20 mL of fresh FTG and incubated at 37 °C for 5 h. Cells were then harvested by centrifugation at 5000 rpm for 3 min, washed twice with Dulbecco's phosphate-buffered saline (DPBS), and resuspended in 500 µL of DPBS to obtain a final concentration of approximately 10^8 CFU/mL.

Each mouse received a subcutaneous injection of 50 µL of bacterial suspension into the left hind thigh and 50 µL of sterile saline into the right thigh as a control. Animals were euthanized 8 h post-inoculation for tissue collection and analysis.

Muscle tissue samples were obtained for histopathological examination and bacterial identification. Tissues were aseptically excised, weighed, and macerated in DPBS (200 µL per sample). Serial tenfold dilutions were plated on brain heart infusion (BHI) agar supplemented with 5% egg yolk and Shahidi Ferguson perfringens (SFP) selective agar (BD Difco) and incubated anaerobically at 37 °C for 24 h (101).

REFERENCES

1. Vouga M, Greub G. 2016. Emerging bacterial pathogens: the past and beyond. Clin Microbiol Infect 22:12–21. doi:10.1016/j.cmi.2015.10.010.
2. Weiss RA, Sankaran N. 2022. Emergence of epidemic diseases: zoonoses and other origins. Fac Rev 11 (2). doi: 10.12703/r/11-2.
3. Cersosimo LM, Worley JN, Bry L. 2024. Approaching toxigenic Clostridia from a One Health perspective. Anaerobe 87:102839. doi:10.1016/j.anaerobe.2024.102839.
4. Lucas T, Brown B. 2024. Expansion of a versatile pathogen: *Clostridioides difficile*. Hygiene and Environmental Health Advances 12:100–108. doi.org/10.1016/j.heha.2024.100108.
5. Abad-Fau A, Sevilla E, Martín-Burriel I, Moreno B, Bolea R. 2023. Update on Commonly Used Molecular Typing Methods for *Clostridioides difficile*. Microorganisms 11(7):1752. doi:10.3390/microorganisms11071752.
6. McGraw P, Lim SC, Collins DA, Riley T V. 2025. Toxigenic, atypical strains of *Clostridioides difficile* isolated from soils of Western Australian public parks. Anaerobe 94:102986. doi:10.1016/j.anaerobe.2025.102986.
7. Kiu R, Caim S, Alexander S, Pachori P, Hall LJ. 2017. Probing genomic aspects of the multi-host pathogen *Clostridium perfringens* reveals significant pangenome diversity, and a diverse array of virulence factors. Front Microbiol 8: 2485. doi: 10.3389/fmicb.2017.02485
8. Brüggemann H. 2005. Genomics of clostridial pathogens: Implication of extrachromosomal elements in pathogenicity. Curr Opin Microbiol 8(5):601–605. doi:10.1016/j.mib.2005.08.006.
9. Mengoli M, Barone M, Fabbrini M, D'Amico F, Brigidi P, Turroni S. 2022. Make It Less difficile: Understanding Genetic Evolution and Global Spread of *Clostridioides difficile*. Genes (Basel) 13(12):2200. doi:10.3390/genes13122200.
10. Hassan KA, Elbourne LDH, Tetu SG, Melville SB, Rood JI, Paulsen IT. 2015. Genomic analyses of *Clostridium perfringens* isolates from five toxinotypes. Res Microbiol 166(4):255–263. doi:10.1016/j.resmic.2014.10.003.
11. Cruz-Morales P, Orellana CA, Moutafis G, Moonen G, Rincon G, Nielsen LK, Marcellin E, Bapteste E. 2019. Revisiting the Evolution and Taxonomy of *Clostridia*, a Phylogenomic Update. Genome Biol Evol 11(7):2035–2044. doi:10.1093/gbe/evz096.

12. Zhu D, Sorg JA, Sun X. 2018. *Clostridioides difficile* biology: Sporulation, germination, and corresponding therapies for *C. difficile* infection. Front Cell Infect Microbiol 8:29. doi: 10.3389/fcimb.2018.00029.
13. Fu Y, Alenezi T, Sun X. 2022. *Clostridium perfringens*-Induced Necrotic Diseases: An Overview. Immuno 2(2):387–407. doi.org/10.3390/immuno2020024.
14. Grenda T, Jarosz A, Sapała M, Grenda A, Patyra E, Kwiatek K. 2023. *Clostridium perfringens*—Opportunistic Foodborne Pathogen, Its Diversity and Epidemiological Significance. Pathogens 12(6):768. doi.org/10.3390/pathogens12060768.
15. Chandrasekaran R, Lacy DB. 2017. The role of toxins in *Clostridium difficile infection*. FEMS Microbiol Rev 41(6):723-750. doi:10.1093/femsre/fux048.
16. Camargo A, Ramírez JD, Kiu R, Hall LJ, Muñoz M. 2024. Unveiling the pathogenic mechanisms of *Clostridium perfringens* toxins and virulence factors. Emerg Microbes Infect 13(1):2341968. doi:10.1080/22221751.2024.2341968.
17. Rood JI, Adams V, Lacey J, Lyras D, McClane BA, Melville SB, Moore RJ, Popoff MR, Sarker MR, Songer JG, Uzal FA, Van Immerseel F. 2018. Expansion of the *Clostridium perfringens* toxin-based typing scheme. Anaerobe 53:5–10. doi:10.1016/j.anaerobe.2018.04.011.
18. Mansfield MJ, Tremblay BJM, Zeng J, Wei X, Hodgins H, Worley J, Bry L, Dong M, Doxey AC. 2020. Phylogenomics of 8,839 *Clostridioides difficile* genomes reveals recombination-driven evolution and diversification of toxin A and B. PLoS Pathog 16(12):e1009181. doi:10.1371/journal.ppat.1009181.
19. Kordus SL, Thomas AK, Lacy DB. 2021. *Clostridioides difficile* toxins: mechanisms of action and antitoxin therapeutics. Nat Rev Microbiol 20(5):285-298. doi:10.1038/s41579-021-00660-2.
20. Ramírez-Vargas G, López-Ureña D, Badilla A, Orozco-Aguilar J, Murillo T, Rojas P, Riedel T, Overmann J, González G, Chaves-Olarte E, Quesada-Gómez C, Rodríguez C. 2018. Novel Clade C-I *Clostridium difficile* strains escape diagnostic tests, differ in pathogenicity potential and carry toxins on extrachromosomal elements. Scientific Reports 8:13951. doi.org/10.1038/s41598-018-32390-6.
21. Camargo A, Guerrero-Araya E, Castañeda S, Vega L, Cardenas-Alvarez MX, Rodríguez C, Paredes-Sabja D, Ramírez JD, Muñoz M. 2022. Intra-species diversity of *Clostridium*

perfringens: A diverse genetic repertoire reveals its pathogenic potential. Front Microbiol 13:952081. doi: 10.3389/fmicb.2022.952081.

22. Trsinar K, Mlakar S, Janzekovic F, Rupnik M, Janezic S. 2025. High prevalence and clonality of *Clostridioides difficile* isolates from cryptic clades in household composters and small mammals. Anaerobe 95:102990. doi:10.1016/j.anaerobe.2025.102990.
23. Williamson CHD, Stone NE, Nunnally AE, Roe CC, Vazquez AJ, Lucero SA, Hornstra H, Wagner DM, Keim P, Rupnik M, Janezic S, Sahl JW. 2022. Identification of novel, cryptic *Clostridioides* species isolates from environmental samples collected from diverse geographical locations. Microb Genom 8(2):000742. doi:10.1099/mgen.0.000742.
24. Knight DR, Imwattana K, Kullin B, Guerrero-Araya E, Paredes-Sabja D, Didelot X, Dingle KE, Eyre DW, Rodríguez C, Riley T V. 2021. Major genetic discontinuity and novel toxigenic species in *Clostridioides difficile* taxonomy. Elife 10:e64325. doi:10.7554/eLife.64325.
25. Rodríguez C, Kiu R, Quesada-Gómez C, Sandí C, Hall, J L. 2020. *Clostridium perfringenosum* sp. nov., a closely related species to *Clostridium perfringens* and its virulence factors, isolated from a human soft tissue infection. bioRxiv https://doi.org/10.1101/2020.12.01.406348.
26. Abdel-Glil MY, Thomas P, Linde J, Busch A, Wieler LH, Neubauer H, Seyboldt C. 2021. Comparative in silico genome analysis of *Clostridium perfringens* unravels stable phylogroups with different genome characteristics and pathogenic potential. Sci Rep 11(1):6756. doi:10.1038/s41598-021-86148-8.
27. Sinnathamby ES, Mason JW, Flanagan CJ, Pearl NZ, Burroughs CR, De Witt AJ, Wenger DM, Klapper VG, Ahmadzadeh S, Varrassi G, Shekoohi S, Kaye A. 2023. *Clostridioides difficile* Infection: A Clinical Review of Pathogenesis, Clinical Considerations, and Treatment Strategies. Cureus 15(12):e51167. doi:10.7759/cureus.51167.
28. Rohana H, Azrad M, Nitzan O, Adler A, Binyamin D, Koren O, Peretz A. 2020. Characterization of *Clostridioides difficile* Strains, the Disease Severity, and the Microbial Changes They Induce. J Clin Med 9(12):4099. doi:10.3390/jcm9124099.
29. Lim SC, Knight DR, Riley T V. 2020. *Clostridium difficile* and One Health. Clinical Microbiology and Infection 26(7):857-863. doi: 10.1016/j.cmi.2019.10.023.
30. Ofori E, Ramai D, Dhawan M, Mustafa F, Gasperino J, Reddy M. 2018. Community-acquired *Clostridium difficile*: epidemiology, ribotype, risk factors, hospital and intensive care unit

outcomes, and current and emerging therapies. Journal of Hospital Infection 99(4):436-442. doi: 10.1016/j.jhin.2018.01.015.

31. CDC. 2019. Antibiotic resistance threats in the United States, 2019. U.S. Department of Health and Human Services, CDC, Atlanta, GA.
32. Chilton CH, Viprey V, Normington C, Moura IB, Buckley AM, Freeman J, Davies K, Wilcox MH. 2025. *Clostridioides difficile* pathogenesis and control. Nat Rev Microbiol. doi.org/10.1038/s41579-025-01242-2.
33. Lawler AJ, Lambert PA, Worthington T. 2020. A Revised Understanding of *Clostridioides difficile* Spore Germination. Trends Microbiol 28(9):744-752. doi:10.1016/j.tim.2020.03.004.
34. Francis MB, Allen CA, Shrestha R, Sorg JA. 2013. Bile acid recognition by the *Clostridium difficile* germinant receptor, CspC, is important for establishing infection. PLoS Pathog 9(5):e1003356. doi:10.1371/journal.ppat.1003356.
35. Wheeldon LJ, Worthington T, Hilton AC, Elliott TSJ, Lambert PA. 2008. Physical and chemical factors influencing the germination of *Clostridium difficile* spores. J Appl Microbiol 105(6):2223-2230. doi: 10.1111/j.1365-2672.2008.03965.x.
36. Baloh M, Sorg JA. 2021. *Clostridioides difficile* spore germination: initiation to DPA release. Curr Opin Microbiol 65:101-107. doi:10.1016/j.mib.2021.11.001.
37. Smits WK, Lyras D, Lacy DB, Wilcox MH, Kuijper EJ. 2016. *Clostridium difficile* infection. Nat Rev Dis Primers 2:16020. doi:10.1038/nrdp.2016.20.
38. DiBenedetto N V., Oberkampf M, Crouzols A, Cersosimo L, Yeliseyev V, Bry L, Peltier J, Dupuy B. 2025. *Clostridioides difficile*'s virulence requires efficient holin-mediated toxin secretion. iScience 28(6):112586. doi:10.1016/j.isci.2025.112586.
39. López-Ureña, D., Quesada-Gómez, C., Rodríguez, C., Chaves-Olarte, E. 2016. Role of *Clostridium difficile* Toxins in Antibiotic-Associated Diarrhea and Pseudomembranous Colitis. In: Gopalakrishnakone, P., Stiles, B., Alape-Girón, A., Dubreuil, J., Mandal, M. (eds) Microbial Toxins. Toxinology. Springer, Dordrecht. doi.org/10.1007/978-94-007-6725-6_17-1.
40. Orozco-Aguilar J, Alfaro-Alarcón A, Acuña-Amador L, Chaves-Olarte E, Rodríguez C, Quesada-Gómez C. 2020. *In vivo* animal models confirm an increased virulence potential

and pathogenicity of the NAP1/RT027/ST01 genotype within the *Clostridium difficile* MLST Clade 2. Gut Pathog 12:45. doi:10.1186/s13099-020-00383-4.

41. Merrigan M, Venugopal A, Mallozzi M, Roxas B, Viswanathan VK, Johnson S, Gerding DN, Vedantam G. 2010. Human Hypervirulent *Clostridium difficile* Strains Exhibit Increased Sporulation as Well as Robust Toxin Production. J Bacteriol 192(19):4904-4911. doi:10.1128/JB.00445-10.
42. Pourliotopoulou E, Karampatakis T, Kachrimanidou M. 2024. Exploring the Toxin-Mediated Mechanisms in *Clostridioides difficile* Infection. Microorganisms 12(5):1004. doi:10.3390/microorganisms12051004.
43. López-Ureña D, Orozco-Aguilar J, Chaves-Madrigal Y, Ramírez-Mata A, Villalobos-Jimenez A, Ost S, Quesada-Gómez C, Rodríguez C, Papatheodorou P, Chaves-Olarte E. 2019. Toxin B variants from *Clostridium difficile* strains VPI 10463 and NAP1/027 share similar substrate profile and cellular intoxication kinetics but use different host cell entry factors. Toxins (Basel) 11(6):348. doi:10.3390/toxins11060348.
44. Bongaerts GPA, Lyerly DM. 1994. Role of toxins A and B in the pathogenesis of *Clostridium difficile* disease. Microb Pathog 17(1):1-12. doi:10.1006/mpat.1994.1047.
45. Chaves-Olarte E, Freer E, Parra A, Guzmán-Verri C, Moreno E, Thelestam M. 2003. R-Ras glucosylation and transient RhoA activation determine the cytopathic effect produced by toxin B variants from toxin A-negative strains of *Clostridium difficile*. J Biol Chem 278(10):7956-7963. doi:10.1074/jbc.M209244200.
46. Carter GP, Rood JI, Lyras D. 2010. The role of toxin A and toxin B in *Clostridium difficile*-associated disease: Past and present perspectives. Gut Microbes 1(1):58-64. doi:10.4161/gmic.1.1.10768.
47. Nibbering B, Gerding DN, Kuijper EJ, Zwittink RD, Smits WK. 2021. Host Immune Responses to *Clostridioides difficile*: Toxins and Beyond. Front Microbiol 2:804949. doi:10.3389/fmicb.2021.804949.
48. Brayan MT, Alejandro AA, Quesada-Gómez C, Chaves-Olarte E, Elías BC. 2025. Polymorphonuclear neutrophil depletion in ileal tissues reduces the immunopathology induced by *Clostridioides difficile* toxins. Anaerobe 92:102947. doi:10.1016/j.anaerobe.2025.102947.

49. Gerding DN, Johnson S, Rupnik M, Aktories K. 2014. *Clostridium difficile* binary toxin CDT: mechanism, epidemiology, and potential clinical importance. Gut Microbes 5(1):15-27. doi:10.4161/gmic.26854.
50. Martínez-Meléndez A, Cruz-López F, Morfin-Otero R, Maldonado-Garza HJ, Garza-González E. 2022. An Update on *Clostridioides difficile* Binary Toxin. Toxins (Basel) 14(5):305. doi:10.3390/toxins14050305.
51. Rao K, Malani PN. 2020. Diagnosis and Treatment of *Clostridioides* (*Clostridium*) *difficile* Infection in Adults in 2020. JAMA 323(14):1403-1404. doi:10.1001/jama.2019.3849.
52. Brosse A, Coullon H, Janoir C, Péchiné S. 2024. The state of play of rodent models for the study of *Clostridioides difficile* infection. J Med Microbiol 73(7):001857. doi:10.1099/jmm.0.001857.
53. Ducarmon QR, van der Bruggen T, Harmanus C, Sanders IMJG, Daenen LGM, Fluit AC, Vossen RHAM, Kloet SL, Kuijper EJ, Smits WK. 2023. *Clostridioides difficile* infection with isolates of cryptic clade C-II: a genomic analysis of polymerase chain reaction ribotype 151. Clin Microbiol Infect29(4):538.e1-538.e6. doi:10.1016/j.cmi.2022.12.003.
54. Schüler MA, Daniel R, Poehlein A. 2023. Complete genome sequence of a *Clostridioides difficile* cryptic C-III strain isolated from horse feces. Microbiol Resour Announc 12(12):e0078123. doi:10.1128/MRA.00781-23.
55. Meier-Kolthoff JP, Göker M. 2019. TYGS is an automated high-throughput platform for state-of-the-art genome-based taxonomy. Nat Commun 10:2182. doi.org/10.1038/s41467-019-10210-3.
56. Monteford J, Bilverstone TW, Ingle P, Philip S, Kuehne SA, Minton NP. 2021. What's a SNP between friends: The lineage of *Clostridioides difficile* R20291 can effect research outcomes. Anaerobe 71:102422. doi:10.1016/j.anaerobe.2021.102422.
57. Quesada-Gómez C, López-Ureña D, Chumbler N, Kroh HK, Castro-Peña C, Rodríguez C, Orozco-Aguilar J, González-Camacho S, Rucavado A, Guzmán-Verri C, Lawley TD, Lacy DB, Chaves-Olarte E. 2016. Analysis of TcdB proteins within the hypervirulent clade 2 reveals an impact of RhoA glucosylation on *Clostridium difficile* proinflammatory activities. Infect Immun 84(3):856-865. doi:10.1128/IAI.01291-15.
58. Kochan TJ, Shoshiev MS, Hastie JL, Somers MJ, Plotnick YM, Gutierrez-Munoz DF, Foss ED, Schubert AM, Smith AD, Zimmerman SK, Carlson PE, Hanna PC. 2018. Germinant

Synergy Facilitates *Clostridium difficile* Spore Germination under Physiological Conditions. mSphere 3(5):e00335-18. doi:10.1128/mSphere.00335-18.

59. Kochan TJ, Somers MJ, Kaiser AM, Shoshiev MS, Hagan AK, Hastie JL, Giordano NP, Smith AD, Schubert AM, Carlson PE, Hanna PC. 2017. Intestinal calcium and bile salts facilitate germination of *Clostridium difficile* spores. PLoS Pathog 13(7):e1006443. doi:10.1371/journal.ppat.1006443.
60. Held P, Brescia PJ, Clayton J. 2025. Automated label-free imaging assay for measuring T cell activation and cluster formation. Application note. Agilent Technologies, Inc., Santa Clara, CA.
61. Fachi JL, Vinolo MAR, Colonna M. 2024. Reviewing the *Clostridioides difficile* Mouse Model: Insights into Infection Mechanisms. Microorganisms 12(2):273. doi:10.3390/microorganisms12020273.
62. Carter GP, Chakravorty A, Nguyen TAP, Mileto S, Schreiber F, Li L, Howarth P, Clare S, Cunningham B, Sambol SP, Cheknis A, Figueroa I, Johnson S, Gerding D, Rood JI, Dougan G, Lawley TD, Lyras D. 2015. Defining the roles of TcdA and TcdB in localized gastrointestinal disease, systemic organ damage, and the host response during *Clostridium difficile* infections. mBio 6(3):e00551. doi:10.1128/mBio.00551-15.
63. LaFrance ME, Farrow MA, Chandrasekaran R, Sheng J, Rubin DH, Lacy DB. 2015. Identification of an epithelial cell receptor responsible for *Clostridium difficile* TcdB-induced cytotoxicity. Proc Natl Acad Sci U S A 112(22):7073-7078. doi:10.1073/pnas.1500791112.
64. Chen X, Katchar K, Goldsmith JD, Nanthakumar N, Cheknis A, Gerding DN, Kelly CP. 2008. A Mouse *Model of Clostridium difficile*-Associated Disease. Gastroenterol 135(6):1984-92. doi:10.1053/j.gastro.2008.09.002.
65. Caserta JA, Robertson SL, Saputo J, Shrestha A, McClane BA, Uzal FA. 2011. Development and Application of a Mouse Intestinal Loop Model To Study the *In Vivo* Action of *Clostridium perfringens* Enterotoxin. Infect Immun 79(8):3020-3027. doi:10.1128/IAI.01342-10.
66. Moore P, Kyne L, Martin A, Solomon K. 2013. Germination efficiency of clinical *Clostridium difficile* spores and correlation with ribotype, disease severity and therapy failure. J Med Microbiol 62(9):1405-1413. doi:10.1099/jmm.0.056614-0.

67. Oka K, Osaki T, Hanawa T, Kurata S, Okazaki M, Manzoku T, Takahashi M, Tanaka M, Taguchi H, Watanabe T, Inamatsu T, Kamiya S. 2012. Molecular and microbiological characterization of *Clostridium difficile* isolates from single, relapse, and reinfection cases. J Clin Microbiol 50(3):915-921. doi:10.1128/JCM.05588-11.
68. Paredes-Sabja D, Bond C, Carman RJ, Setlow P, Sarker MR. 2008. Germination of spores of *Clostridium difficile* strains, including isolates from a hospital outbreak of *Clostridium difficile*-associated disease (CDAD). Microbiology (Reading) 154(8):2241-2250. doi:10.1099/mic.0.2008/016592-0.
69. Sorg JA, Sonenshein AL. 2008. Bile salts and glycine as cogerminants for *Clostridium difficile* spores. J Bacteriol 190(7):2505-2512. doi:10.1128/JB.01765-07.
70. Smits WK. 2013. Hype or hypervirulence: a reflection on problematic *C. difficile strains.* Virulence 4(7):592-596. doi:10.4161/viru.26297.
71. Darkoh C, Dupont HL, Norris SJ, Kaplan HB. 2015. Toxin synthesis by *Clostridium difficile* is regulated through quorum signaling. mBio 6(2):e02569. doi:10.1128/mBio.02569-14.
72. Aminzadeh A, Jørgensen R. 2021. Systematic Evaluation of Parameters Important for Production of Native Toxin A and Toxin B from *Clostridioides difficile*. Toxins (Basel) 13(4):240. doi:10.3390/toxins13040240.
73. Lanis JM, Barua S, Ballard JD. 2010. Variations in TcdB activity and the hypervirulence of emerging strains of *Clostridium difficile*. PLoS Pathog 6(8):e1001061. doi:10.1371/journal.ppat.1001061.
74. Chandra H, Sorg JA, Hassett DJ, Sun X. 2023. Regulatory transcription factors of *Clostridioides difficile* pathogenesis with a focus on toxin regulation. Crit Rev Microbiol 49(3):334-349. doi:10.1080/1040841X.2022.2054307.
75. Hamo Z, Azrad M, Fichtman B, Peretz A. 2021. The Cytopathic Effect of Different Toxin Concentrations From Different *Clostridioides difficile* Sequence Types Strains in Vero Cells. Front Microbiol 12:763129. doi: 10.3389/fmicb.2021.763129.
76. Schöttelndreier D, Seeger K, Grassl GA, Winny MR, Lindner R, Genth H. 2018. Expression and (Lacking) Internalization of the Cell Surface Receptors of *Clostridioides difficile* Toxin B. Front Microbiol 9:1483. doi:10.3389/fmicb.2018.01483.

77. Guo S, Chen Y, Liu J, Zhang X, Liu Z, Zhou Z, Wei W. 2022. Low-density lipoprotein receptor-related protein 1 is a CROPs-associated receptor for Clostridioides infection toxin B. Sci China Life Sci 65(1):107-118. doi:10.1007/s11427-021-1943-9.

78. Henkel D, Tatge H, Schöttelndreier D, Tao L, Dong M, Gerhard R. 2020. Receptor Binding Domains of TcdB from *Clostridioides difficile* for Chondroitin Sulfate Proteoglycan-4 and Frizzled Proteins Are Functionally Independent and Additive. Toxins (Basel) 12(12):736. doi:10.3390/toxins12120736.

79. Chen P, Tao L, Wang T, Zhang J, He A, Lam K ho, Liu Z, He X, Perry K, Dong M, Jin R. 2018. Structural basis for recognition of frizzled proteins by *Clostridium difficile* toxin B. Science 360(6389):664-669. doi:10.1126/science.aar1999.

80. Luo J, Yang Q, Zhang X, Zhang Y, Wan L, Zhan X, Zhou Y, He L, Li D, Jin D, Zhen Y, Huang J, Li Y, Tao L. 2022. TFPI is a colonic crypt receptor for TcdB from hypervirulent clade 2 *C. difficile.* Cell 85(6):980-994.e15. doi:10.1016/j.cell.2022.02.010.

81. Tian S, Xiong X, Zeng J, Wang S, Tremblay BJM, Chen P, Chen B, Liu M, Chen P, Sheng K, Zeve D, Qi W, Breault DT, Rodríguez C, Gerhard R, Jin R, Doxey AC, Dong M. 2022. Identification of TFPI as a receptor reveals recombination-driven receptor switching in *Clostridioides difficile* toxin B variants. Nat Commun 13, 6786. doi.org/10.1038/s41467-022-33964-9.

82. Christopher Peritore-Galve F, Shupe JA, Cave RJ, Childress KO, Kay Washington M, Kuehne SA, Borden Lacy D. 2022. Glucosyltransferase-dependent and independent effects of *Clostridioides difficile* toxins during infection. PLoS Pathog 18:e1010323. doi:10.1371/journal.ppat.1010323.

83. Fettucciari K, Fruganti A, Stracci F, Spaterna A, Marconi P, Bassotti G. 2023. *Clostridioides difficile* Toxin B Induced Senescence: A New Pathologic Player for Colorectal Cancer? Int J Mol Sci 24(9):8155. doi:10.3390/ijms24098155.

84. Mileto SJ, Jardé T, Childress KO, Jensen JL, Rogers AP, Kerr G, Hutton ML, Sheedlo MJ, Bloch SC, Shupe JA, Horvay K, Flores T, Engel R, Wilkins S, McMurrick PJ, Lacy DB, Abud HE, Lyras D. 2020. *Clostridioides difficile* infection damages colonic stem cells via TcdB, impairing epithelial repair and recovery from disease. Proc Natl Acad Sci U S A 117(14):8064-8073. doi:10.1073/pnas.1915255117.

85. Diniz AN, Moura LNF, Cruz DSG, Junior CAO, Figueiredo HCP, Cunha JLR, Vilela EG, Kuijper EJ, Wilcox MH, Lobato FCF, Silva ROS. 2022. Characterization of the virulence of three novel clade 2 *Clostridioides* (*Clostridium*) *difficile* strains and a two-year screening in animals and humans in Brazil. PLoS One 17(8):e0273013. doi:10.1371/journal.pone.0273013.

86. Mitchell TJ, Ketley JM, Haslam SC, Stephen J, Burdon DW, Candy DC, Daniel R. 1986. Effect of toxin A and B of *Clostridium difficile* on rabbit ileum and colon. Gut 27(1):78-85. doi:10.1136/gut.27.1.78.

87. Jafari N V., Kuehne SA, Bryant CE, Elawad M, Wren BW, Minton NP, Allan E, Bajaj-Elliott M. 2013. *Clostridium difficile* modulates host innate immunity via toxin-independent and dependent mechanism(s). PLoS One 8(7):e69846. doi:10.1371/journal.pone.0069846.

88. Jose S, Madan R. 2016. Neutrophil-mediated inflammation in the pathogenesis of *Clostridium difficile* infections. Anaerobe 41:85-90. doi:10.1016/j.anaerobe.2016.04.001.

89. Hirota SA, Fines K, Ng J, Traboulsi D, Lee J, Ihara E, Li Y, Willmore WG, Chung D, Scully MM, Louie T, Medlicott S, Lejeune M, Chadee K, Armstrong G, Colgan SP, Muruve DA, MacDonald JA, Beck PL. 2010. Hypoxia-Inducible Factor Signaling Provides Protection in *Clostridium difficile*-Induced Intestinal Injury. Gastroenterol 139(1):259-69.e3. doi:10.1053/j.gastro.2010.03.045.

90. Castro-Cordova P, Lopez-Garcia OK, Orozco J, Montes-Bravo N, Gil F, Pizarro-Guajardo M, Paredes-Sabja D. 2025. *Clostridioides difficile* major toxins remodel the intestinal epithelia, affecting spore adherence/internalization into intestinal tissue and their association with gut vitronectin. bioRxiv https://doi.org/10.1101/2025.01.29.635439.

91. Sun X, Savidge T, Feng H. 2010. The enterotoxicity of *Clostridium difficile* toxins. Toxins (Basel) 2(7):1848-1880. doi:10.3390/toxins2071848.

92. Hunt JJ, Ballard JD. 2013. Variations in virulence and molecular biology among emerging strains of *Clostridium difficile*. Microbiol Mol Biol Rev 77(4):567-581. doi:10.1128/MMBR.00017-13.

93. Pawlowski SW, Calabrese G, Kolling GL, Platts-Mills J, Freire R, AlcantaraWarren C, Liu B, Sartor RB, Guerrant RL. 2010. Murine Model of *Clostridium difficile* Infection with Aged Gnotobiotic C57BL/6 Mice and a BI/NAP1 Strain. J Infect Dis 202(11):1708-1712. doi:10.1086/657086.

94. Bendary MM, Abd El-Hamid MI, El-Tarabili RM, Hefny AA, Algendy RM, Elzohairy NA, Ghoneim MM, Al-Sanea MM, Nahari MH, Moustafa WH. 2022. *Clostridium perfringens* Associated with Foodborne Infections of Animal Origins: Insights into Prevalence, Antimicrobial Resistance, Toxin Genes Profiles, and Toxinotypes. Biol (Basel) 11(4):551. doi.org/10.3390/biology11040551.

95. Feng Y, Fan X, Zhu L, Yang X, Liu Y, Gao S, Jin X, Liu D, Ding J, Guo Y, Hu Y. 2020. Phylogenetic and genomic analysis reveals high genomic openness and genetic diversity of *Clostridium perfringens*. Microb Genom 6(10):mgen000441. doi:10.1099/mgen.0.000441.

96. Kiu R, Hall LJ. 2018. An update on the human and animal enteric pathogen *Clostridium perfringens*. Emerg Microbes Infect 7(1):141. doi:10.1038/s41426-018-0144-8.

97. Geier RR, Rehberger TG, Smith AH. 2021. Comparative Genomics *of Clostridium perfringens* Reveals Patterns of Host-Associated Phylogenetic Clades and Virulence Factors. Front Microbiol 12:649953. doi:10.3389/fmicb.2021.649953.

98. Buttolph A, Marietta M, Sapra A. 2023. Gas gangrene. In Chronic diseases: an encyclopedia of causes, effects, and treatments, vol 1. StatPearls Publishing, Treasure Island, FL.

99. Mehdizadeh Gohari I, A. Navarro M, Li J, Shrestha A, Uzal F, A. McClane B. 2021. Pathogenicity and virulence of *Clostridium* perfringens. Virulence 12(1):723-753. doi:10.1080/21505594.2021.1886777.

100. Navarro MA, Li J, Beingesser J, McClane BA, Uzal FA. 2020. The Agr-Like Quorum-Sensing System Is Important for *Clostridium perfringens* Type A Strain ATCC 3624 To Cause Gas Gangrene in a Mouse Model. mSphere 5(3):e00500-20. doi:10.1128/mSphere.00500-20.

101. Uzal FA, McClane BA, Cheung JK, Theoret J, Garcia JP, Moore RJ, Rood JI. 2015. Animal models to study the pathogenesis of human and animal *Clostridium perfringens* infections. Vet Microbiol 179(1-2):23-33. doi:10.1016/j.vetmic.2015.02.013.

102. Monturiol-Gross L, Villalta-Romero F, Flores-Díaz M, Alape-Girón A. 2021. Bacterial phospholipases C with dual activity: phosphatidylcholinesterase and sphingomyelinase. FEBS Open Bio 11(12):3262-3275. doi:10.1002/2211-5463.13320.

103. Eaton JT, Naylor CE, Howells AM, Moss DS, Titball RW, Basak AK. 2002. Crystal structure of the *C. perfringens* alpha-toxin with the active site closed by a flexible loop region. J Mol Biol 319(2):275-281. doi:10.1016/S0022-2836(02)00290-5.

104. Urbina P, Flores-Díaz M, Alape-Girón A, Alonso A, Goni FM. 2009. Phospholipase C and sphingomyelinase activities of the *Clostridium perfringens* α-toxin. Chem Phys Lipids 159(1):51-57. doi:10.1016/j.chemphyslip.2009.02.007.

105. Nagahama M, Nakayama T, Michiue K, Sakurai J. 1997. Site-specific mutagenesis of *Clostridium perfringens* alpha-toxin: replacement of Asp-56, Asp-130, or Glu-152 causes loss of enzymatic and hemolytic activities. Infect Immun 65(8):3489-3492. doi:10.1128/iai.65.8.3489-3492.1997.

106. Sakurai J, Nagahama M, Oda M. 2004. *Clostridium perfringens* alpha-toxin: characterization and mode of action. J Biochem 136(5):569-574. doi:10.1093/jb/mvh161.

107. Alape-Girón A, Flores-Díaz M, Guillouard I, Naylor CE, Titball RW, Rucavado A, Lomonte B, Basak AK, Gutiérrez JM, Cole ST, Thelestam M. 2000. Identification of residues critical for toxicity in *Clostridium perfringens* phospholipase C, the key toxin in gas gangrene. Eur J Biochem 267(16):5191-5197. doi:10.1046/j.1432-1327.2000.01588.x.

108. Naylor CE, Eaton JT, Howells A, Justin N, Moss DS, Titball RW, Basak AK. 1998. Structure of the key toxin in gas gangrene. Nat Struct Biol 5(8):738-746. doi:10.1038/1447.

109. Oda M, Ikari S, Matsuno T, Morimune Y, Nagahama M, Sakurai J. 2006. Signal transduction mechanism involved in *Clostridium perfringens* alpha-toxin-induced superoxide anion generation in rabbit neutrophils. Infect Immun 74(5):2876-2886. doi:10.1128/IAI.74.5.2876-2886.2006.

110. Oda M, Kabura M, Takagishi T, Suzue A, Tominaga K, Urano S, Nagahama M, Kobayashi K, Furukawa K, Furukawa K, Sakurai J. 2012. *Clostridium perfringens* alpha-toxin recognizes the GM1a-TrKA complex. J Biol Chem 287(39):33070-33079. doi:10.1074/jbc.M112.393801.

111. Navarro MA, McClane BA, Uzal FA. 2018. Mechanisms of Action and Cell Death Associated with *Clostridium perfringens* Toxins. Toxins (Basel) 10(5):212. doi:10.3390/toxins10050212.

112. Flores-Díaz M, Alape-Girón A. 2003. Role of *Clostridium perfringens* phospholipase C in the pathogenesis of gas gangrene. Toxicon 42(8):979-986. doi:10.1016/j.toxicon.2003.11.013.

113. Urbina P, Collado MI, Alonso A, Goñi FM, Flores-Díaz M, Alape-Girón A, Ruysschaert JM, Lensink MF. 2011. Unexpected wide substrate specificity of C. *perfringens* α-toxin

phospholipase C. Biochim Biophys Acta 1808(10):2618-2627. doi:10.1016/j.bbamem.2011.06.008.

114. Takehara M, Bandou H, Kobayashi K, Nagahama M. 2020. *Clostridium perfringens* α-toxin specifically induces endothelial cell death by promoting ceramide-mediated apoptosis. Anaerobe 65:102262. doi:10.1016/j.anaerobe.2020.102262.
115. Takehara M, Seike S, Sonobe Y, Bandou H, Yokoyama S, Takagishi T, Miyamoto K, Kobayashi K, Nagahama M. 2019. *Clostridium perfringens* α-toxin impairs granulocyte colony-stimulating factor receptor-mediated granulocyte production while triggering septic shock. Commun Biol 2:45. doi:10.1038/s42003-019-0280-2.
116. Awad MM, Ellemor DM, Boyd RL, Emmins JJ, Rood JI. 2001. Synergistic Effects of Alpha-Toxin and Perfringolysin O in *Clostridium perfringens*-Mediated Gas Gangrene. Infect Immun 69(12):7904-7910. doi:10.1128/IAI.69.12.7904-7910.2001.
117. Badilla-Vargas L, Pereira R, Molina-Mora JA, Alape-Girón A, Flores-Díaz M. 2023. *Clostridium perfringens* phospholipase C, an archetypal bacterial virulence factor, induces the formation of extracellular traps by human neutrophils. Front Cell Infect Microbiol 13:1278718. doi:10.3389/fcimb.2023.1278718.
118. Takehara M, Kobayashi K, Nagahama M. 2021. Toll-Like Receptor 4 Protects Against *Clostridium perfringens* Infection in Mice. Front Cell Infect Microbiol 11:633440. doi:10.3389/fcimb.2021.633440.
119. Zúñiga-Pereira AM, Santamaría C, Gutierrez JM, Alape-Girón A, Flores-Díaz M. 2019. Deficient Skeletal Muscle Regeneration after Injury Induced by a *Clostridium perfringens* Strain Associated with Gas Gangrene. Infect Immun 87:e00200-19. doi:10.1128/IAI.00200-19.
120. Dione N, Lo CI, Raoult D, Fenollar F, Fournier PE. 2020. *Clostridium massiliamazoniense* sp. nov., New Bacterial Species Isolated from Stool Sample of a Volunteer Brazilian. Curr Microbiol 77(9):2008-2015. doi:10.1007/s00284-020-02099-9.
121. Hosny M, Abdallah RA, Bou Khalil J, Fontanini A, Baptiste E, Armstrong N, La Scola B. 2018. *Clostridium pacaense:* a new species within the genus *Clostridium.* New Microbes New Infect 28:6-10. doi:10.1016/j.nmni.2018.12.003.
122. QIAGEN. 2011. QIAexpress Ni-NTA fast start handbook, 2nd ed. QIAGEN, Hilden, Germany.

123. Varnavides G, Madern M, Anrather D, Hartl N, Reiter W, Hartl M. 2022. In Search of a Universal Method: A Comparative Survey of Bottom-Up Proteomics Sample Preparation Methods. J Proteome Res 21(10):2397-2411. doi:10.1021/acs.jproteome.2c00265.
124. Gubash SM. 1991. Improved egg-yolk agar plate medium for the detection of clostridial phospholipase C activity. Res Microbiol 142(1):87-93. doi:10.1016/0923-2508(91)90100-o.
125. Ochi S, Oda M, Nagahama M, Sakurai J. 2003. *Clostridium perfringens* alpha-toxin-induced hemolysis of horse erythrocytes is dependent on Ca^{2+} uptake. Biochim Biophys Acta Biomembr 1613(1-2):79-86. doi:10.1016/s0005-2736(03)00140-8.
126. Tatusov RL, Galperin MY, Natale DA, Koonin EV. 2000. The COG database: a tool for genome-scale analysis of protein functions and evolution. Nucleic Acids Res 28:33–36. doi.org/10.1093/nar/28.1.33.
127. Awad MM, Bryant AE, Stevens DL, Rood JI. 1995. Virulence studies on chromosomal alpha-toxin and theta-toxin mutants constructed by allelic exchange provide genetic evidence for the essential role of alpha-toxin in *Clostridium perfringens*-mediated gas gangrene. Mol Microbiol 15(2):191-202. doi:10.1111/j.1365-2958.1995.tb02234.x.
128. Xiao Y, Van Hijum SAFT, Abee T, Wells-Bennik MHJ. 2015. Genome-Wide Transcriptional Profiling of *Clostridium perfringens* SM101 during Sporulation Extends the Core of Putative Sporulation Genes and Genes Determining Spore Properties and Germination Characteristics. PLoS One 10(5):e0127036. doi:10.1371/journal.pone.0127036.
129. Liu H, McCord KD, Howarth J, Popham DL, Jensen R V., Melville SB. 2014. Hypermotility in *Clostridium perfringens* strain SM101 is due to spontaneous mutations in genes linked to cell division. J Bacteriol 196(13):2405-2412. doi:10.1128/JB.01614-14.
130. Flores-Díaz M, Alape-Girón A, Clark G, Catimel B, Hirabayashi Y, Nice E, Gutiérrez JM, Titball R, Thelestam M. 2005. A cellular deficiency of gangliosides causes hypersensitivity to *Clostridium perfringens* phospholipase C. Journal of Biological Chemistry 280(29):26680-26689. doi:10.1074/jbc.M500278200.
131. Riss TL, Moravec RA, Niles AL, et al. 2016. Cell viability assays. In Markossian S, Grossman A, Baskir H, et al (ed), Assay guidance manual. Eli Lilly & Company and the National Center for Advancing Translational Sciences, Bethesda, MD. https://www.ncbi.nlm.nih.gov/books/NBK144065.

132. Sengupta N, Alam SI, Kumar B, Kumar RB, Gautam V, Kumar S, Singh L. 2010. Comparative proteomic analysis of extracellular proteins of *Clostridium perfringens* type A and type C strains. Infect Immun 78(9):3957-3968. doi:10.1128/IAI.00374-10.

133. Vahedi A, Bigdelou P, Farnoud AM. 2020. Quantitative analysis of red blood cell membrane phospholipids and modulation of cell-macrophage interactions using cyclodextrins. Sci Rep 10(1):15111. doi:10.1038/s41598-020-72176-3.

134. Guillouard I, Alzari PM, Saliou B, Cole ST. 1997. The carboxy-terminal C2-like domain of the alpha-toxin from *Clostridium perfringens* mediates calcium-dependent membrane recognition. Mol Microbiol 26(5):867-876. doi:10.1046/j.1365-2958.1997.6161993.x.

135. Karasawa T, Wang X, Maegawa T, Michiwa Y, Kita H, Miwa K, Nakamura S. 2003. *Clostridium sordellii* phospholipase C: gene cloning and comparison of enzymatic and biological activities with those of *Clostridium perfringens* and *Clostridium bifermentans* phospholipase C. Infect Immun 71(2):641-646. doi:10.1128/IAI.71.2.641-646.2003.

136. Jepson M, Howells A, Bullifent HL, Bolgiano B, Crane D, Miller J, Holley J, Jayasekera P, Titball RW. 1999. Differences in the carboxy-terminal (Putative phospholipid binding) domains of *Clostridium perfringens* and *Clostridium bifermentans* phospholipases C influence the hemolytic and lethal properties of these enzymes. Infect Immun 67(7):3297-3301. doi:10.1128/IAI.67.7.3297-3301.1999.

137. Monturiol-Gross L, Flores-Díaz M, Pineda-Padilla MJ, Castro-Castro AC, Alape-Giron A. 2014. *Clostridium perfringens* phospholipase C induced ROS production and cytotoxicity require PKC, MEK1 and NFκB activation. PLoS One 9(1):e86475. doi:10.1371/journal.pone.0086475.

138. Bakala N'Goma JC, Schué M, Carrière F, Geerlof A, Canaan S. 2010. Evidence for the cytotoxic effects of *Mycobacterium tuberculosis* phospholipase C towards macrophages. Biochim Biophys Acta Mol Cell Biol Lipids 1801(12):1305-1313. doi:10.1016/j.bbalip.2010.08.007.

139. Shimizu T, Shima K, Yoshino KI, Yonezawa K, Shimizu T, Hayashi H. 2002. Proteome and transcriptome analysis of the virulence genes regulated by the VirR/VirS system in *Clostridium perfringens*. J Bacteriol 184(10):2587-2594. doi:10.1128/JB.184.10.2587-2594.2002.

140. Ebner P, Götz F. 2019. Bacterial Excretion of Cytoplasmic Proteins (ECP): Occurrence, Mechanism, and Function. Trends Microbiol 27(2):176-187. doi:10.1016/j.tim.2018.10.006.
141. Liu H, Bouillaut L, Sonenshein AL, Melville SB. 2013. Use of a mariner-based transposon mutagenesis system to isolate *Clostridium perfringens* mutants deficient in gliding motility. J Bacteriol 195(3):629-636. doi:10.1128/JB.01288-12.
142. Low LY, Harrison PF, Gould J, Powell DR, Choo JM, Forster SC, Chapman R, Gearing LJ, Cheung JK, Hertzog P, Rood JI. 2018. Concurrent Host-Pathogen Transcriptional Responses in a *Clostridium perfringens* Murine Myonecrosis Infection. mBio 9(2):e00473-18. Published 2018 Mar 27. doi:10.1128/mBio.00473-18.
143. Skotnicka D, Petters T, Heering J, Hoppert M, Kaever V, Søgaard-Andersen L. 2015. Cyclic Di-GMP Regulates Type IV Pilus-Dependent Motility in *Myxococcus xanthus*. J Bacteriol 198(1):77-90. doi:10.1128/JB.00281-15.